Graduate School ETD Form 9
(Revised 12/07)

PURDUE UNIVERSITY
GRADUATE SCHOOL
Thesis/Dissertation Acceptance

This is to certify that the thesis/dissertation prepared

By Joseph David Heidenreich

Entitled MOLECULAR DYNAMICS SIMULATIONS OF THE MECHANICAL DEFORMATION BEHAVIOR OF FACE-CENTERED CUBIC METALLIC NANOWIRES

For the degree of Master of Science in Mechanical Engineering

Is approved by the final examining committee:

Guofeng Wang
Chair

Alan Jones

Jie Chen

To the best of my knowledge and as understood by the student in the *Research Integrity and Copyright Disclaimer (Graduate School Form 20)*, this thesis/dissertation adheres to the provisions of Purdue University's "Policy on Integrity in Research" and the use of copyrighted material.

Approved by Major Professor(s): Guofeng Wang

Approved by: Jie Chen 4/21/2010
Head of the Graduate Program Date

Graduate School Form 20
(Revised 1/10)

PURDUE UNIVERSITY
GRADUATE SCHOOL

Research Integrity and Copyright Disclaimer

Title of Thesis/Dissertation:
MOLECULAR DYNAMICS SIMULATIONS OF THE MECHANICAL DEFORMATION BEHAVIOR OF FACE-CENTERED CUBIC METALLIC NANOWIRES

For the degree of Master of Science in Mechanical Engineering

I certify that in the preparation of this thesis, I have observed the provisions of *Purdue University Teaching, Research, and Outreach Policy on Research Misconduct (VIII.3.1)*, October 1, 2008.*

Further, I certify that this work is free of plagiarism and all materials appearing in this thesis/dissertation have been properly quoted and attributed.

I certify that all copyrighted material incorporated into this thesis/dissertation is in compliance with the United States' copyright law and that I have received written permission from the copyright owners for my use of their work, which is beyond the scope of the law. I agree to indemnify and save harmless Purdue University from any and all claims that may be asserted or that may arise from any copyright violation.

Joseph David Heidenreich
Printed Name and Signature of Candidate

04/22/2010
Date (month/day/year)

*Located at http://www.purdue.edu/policies/pages/teach_res_outreach/viii_3_1.html

MOLECULAR DYNAMICS SIMULATIONS OF THE MECHANICAL DEFORMATION BEHAVIOR OF FACE-CENTERED CUBIC METALLIC NANOWIRES

A Thesis
Submitted to the Faculty
of
Purdue University
by
Joseph David Heidenreich

In Partial Fulfillment of the
Requirements for the Degree
of
Master of Science in Mechanical Engineering

May 2010
Purdue University
Indianapolis, Indiana

ACKNOWLEDGEMENTS

I would like to thank my research advisor, Dr. Guofeng Wang for giving me the opportunity to work with him on this project. Without his guidance and knowledge base this project would not be possible. I would also like to thank the IUPUI Mechanical Engineering Department for funding through a block grant. Thanks to Dr. Jie Chen and Dr. Alan Jones for being on my committee and proving many useful suggestions and critiques which were incorporated into the final draft. Lastly, I would like to thank my research group comprised of Zhiyao Duan, Chan Xiao, Yuhua Zhang, and Jun Zhong for help throughout the project.

TABLE OF CONTENTS

Page

LIST OF TABLES

LIST OF FIGURES

Figure Page

Figure Page

Figure Page

Figure Page

ABSTRACT

Heidenreich, Joseph David. M.S.M.E., Purdue University, May 2010. Molecular Dynamics Simulations of the Mechanical Deformation Behavior of Face-Centered Cubic Metallic Nanowires. Major Professor: Guofeng Wang.

Nanoscale materials have become an active area of research due to the enhanced mechanical properties of the nanomaterials in comparison to their respective bulk materials. The effect that the size and shape of a nanomaterial has on its mechanical properties is important to understand if these materials are to be used in engineering applications. This thesis presents the results of molecular dynamics (MD) simulations on copper, gold, nickel, palladium, platinum, and silver nanowires of three cross-sectional shapes and four diameters. The cross-sectional shapes investigated were square, circular, and octagonal while the diameters varied from one to eight nanometers.

Due to a high surface area to volume ratio, nanowires do not have the same atomic spacing as bulk materials. To account for this difference, prior to tensile loading, a minimization procedure was applied to find the equilibrium strain for each structure size and shape. Through visualization of the atomic energy before and after minimization, it was found that there are more than two energetically distinct areas within the nanowires. In addition, a correlation between the anisotropy of a material and its equilibrium strain was found.

The wires were then subjected to a uniaxial tensile load in the [100] direction at a strain rate of 10^8 s^{-1} with a simulation temperature of 300 K. The embedded-atom method (EAM) was employed using the Foiles [1] potential to simulate the stretching of

the wires. The wires were stretched to failure, and the corresponding stress-strain curves were produced. From these curves, mechanical properties including the elastic modulus, yield stress and strain, and ultimate strain were calculated. In addition to the MD approach, an energy method was applied to calculate the elastic modulus of each nanowire through exponential fitting of an energy function. Both methods used to calculate Young's modulus qualitatively gave similar results indicating that as diameter decreases, Young's modulus decreases.

The MD simulations were also visualized to investigate the deformation and yield behavior of each nanowire. Through the visualization, most nanowires were found to yield and fail through partial dislocation nucleation and propagation leading to {111} slip. However, the 5 nm diameter octagonal platinum nanowire was found to yield through reconstruction of the {011} surfaces into the more energetically favorable {021} surfaces.

1. INTRODUCTION

1.1 Objectives

The two goals of this research are (1) to investigate the effect of nanomaterials' cross-sectional size and shape on the elastic and plastic mechanical properties of the materials, and (2) to view the atomic movement to gain insight into the deformation characteristics. The cross-sectional size and shape have previously been investigated, but not across such a broad range of materials. Widening the scope of materials used allows us to search for trends that may occur. If these trends are identified, we can achieve a better understanding of what materials to select for systems on the nano-scale. Viewing the atomic movement gives molecular dynamics an advantage versus physical experiments. While physical experiments can yield numerical results, molecular dynamics allows us to view the system in ways which are impossible to do experimentally. Molecular dynamics can be used to identify the cause of the numerical results through viewing the movement of individual atoms from many angles and observing a large number of physical quantities.

The broad scope of this molecular dynamics study included six different materials to investigate how these effects vary based on the material. In each case, an EAM potential developed by Adams, Foiles, and Wolfer [1] was used so results could be compared across materials. Specifically, the following five properties were investigated: (1) yield stress, (2) yield strain, (3) ultimate stress, (4) ultimate strain, and (5) Young's modulus.

To collect additional qualitative data, the nanowires were visualized throughout the deformation. A code was developed to allow the visualization of the strain energy of

each individual atom. Through visualization of the atoms and their energy, phenomena such as twinning, defect nucleation and propagation, surface reconstruction, and slip planes were observed. The visualization allowed for a comparison of yield behavior across all cross sections and materials.

To attain the objectives listed above, both preprocessors and postprocessors were created to input and analyze data from the experiment. All processing was accomplished by creating programs written in C and Tcl programming languages.

1.2 Description of Mechanical Properties

Many of the results presented in this thesis are numerical values which describe some of the mechanical properties of nanowires. Here, each property will be described and a sample stress-strain diagram provided to illustrate how some of the values were calculated.

Figure 1.1 shows an example of a stress-strain diagram which was created during this research. The blue area of the graph indicates the elastic region. The elastic region represents the area where changes to the structure due to stretching are reversible. That is, if the load was removed prior the yield point, the structure should move back to its equilibrium structure. The deformation in this region is reversible as the elongation prior to yielding is due to stretching of the bonds between atoms.

The point where the elastic region ends and the plastic region begins is the yield point. The plastic region is indicated by the red background in Figure 1.1. Structure changes in the plastic region are irreversible since bonds are broken and reformed beyond the yield point. The y axis intercept of the yield point is referred to as the yield stress while the x axis intercept is referred to as the yield strain. The slope of the stress-strain curve prior to yielding is Young's modulus. Young's modulus is a measure of the stiffness of the material with respect to tensile loading.

The stress-strain response of nanomaterials looks different than the stress-strain response of bulk materials. Nanomaterials exhibit localized yielding events. These localized yields correspond to the nucleation of a defect which dissipates internal energy causing a near instantaneous drop in the stress.

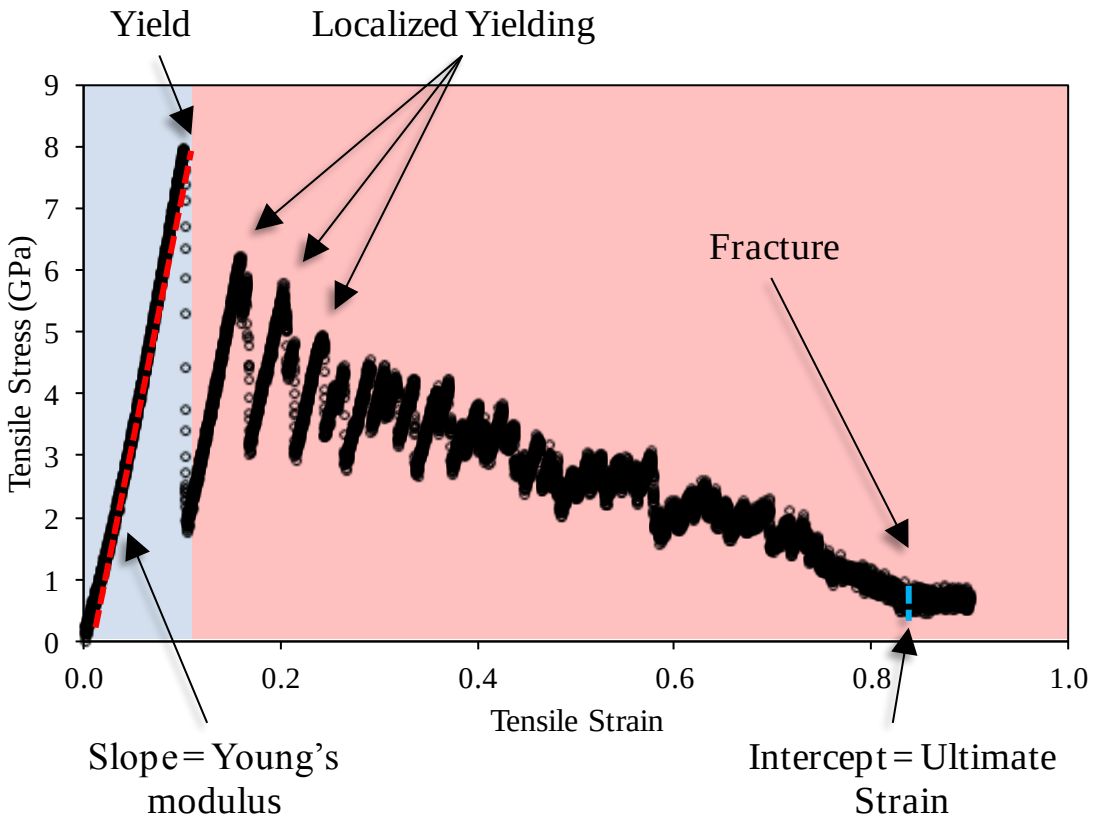

Figure 1.1 Stress-strain diagram of a 5 nm circular copper nanowire with the mechanical properties labeled

Lastly, fracture occurs when the nanowire breaks into two pieces. The exact point of fracture in Figure 1.1 is difficult to distinguish as there is thermal noise which causes the stress level to vary above 0 GPa. The actual fracture point was determined through visualization of the system. The strain value at which fracture occurred is referred to as the ultimate strain.

1.3 Organization

This thesis is organized into six chapters prepared to promote a logical flow of information. The first chapter is an introduction to the thesis providing an overview of the accomplishments and objectives of this research.

Chapter 2 provides background information describing molecular dynamics and the components required to begin simulations. An explanation of the steps completed to calculate the trajectory of atoms is provided. Methods of decreasing computation time are discussed. The methods used in this thesis, such as the embedded atom method and Velocity-Verlet numerical integration, are also discussed and explained in greater detail. In addition, the limits of using molecular dynamics are explored.

Chapter 3 provides a literature review describing the current state of MD simulations on nanomaterials. It discusses three types of current literature: (1) the current state of molecular simulations on nanomaterials, (2) the current state of physical experiments on nanomaterials, and (3) current theoretical work describing the behavior of nano-sized materials. In particular, the literature review focuses on experiments which investigate the mechanical properties of metallic nanowires.

Chapter 4 provides the motivation behind the research and describes the experimental setup for the simulations. Included in the description is the software package used, the choice of potential, structure minimization, experimental parameters, and visualization setup. Also, the continuum mechanics formulation and matrix method for determining Young's modulus are presented. These two methods are presented as ways to validate the molecular dynamics approach and results.

Chapter 5 both presents and discusses all the results of the research. Tables containing all numerical values obtained are presented. In addition, some values are graphed to show size correlation. In-depth figures showing yield mechanisms are

presented and described. Lastly, Chapter 6 offers conclusions and suggestions for further study.

2. A REVIEW OF MOLECULAR DYNAMICS

2.1 Introduction

Molecular dynamics (MD) is a branch of science that models atomic interaction. Usually studied through computer simulations, known physical approximations provide a view of the motion of individual atoms. The large number of molecules prevents an analytic solution of the system, so numerical methods are applied to approximate solutions. The principle of molecular dynamics was first conceived by Alder and Wainwright [2] in 1959 in which they envisioned modeling "the behavior of several hundred interacting classical particles."

More recently, MD has gained popularity with the decreasing cost of powerful personal computer processors capable of performing local simulations without the necessity of a supercomputer. Larger calculations can still utilize a parallel supercomputer by decomposing the MD simulation into smaller units and distributing those smaller simulations to individual nodes. Plimpton [3] discusses three types of decomposition for parallel computing: atom decomposition, force decomposition, and spatial decomposition. Each method has pros and cons, but they all allow the CPU time to be distributed across multiple processors. By spreading out the calculations, MD simulations which may take multiple CPU-months or years to be completed can be achieved in a matter of hours or days.

To compute the trajectory of an MD system, two main components are required. First to find the force equations for each atom, a potential energy function is required. This process is discussed in more detail in Section 2.2. Secondly, the forces obtained for each atom must be integrated to compute the motion of each atom. Because of the

complexity of the system, analytic integration is difficult, so numerical methods are used to calculate the motion of the atoms. Different numerical integration methods are presented in Section 2.3.

2.2 Potentials

Potential energy functions play a significant role in MD simulations. In MD simulations, the atoms move due to forces acting on them as described by Newton's second law of motion:

$$\vec{F} = m\vec{a} = m\frac{d\vec{v}}{dt} = m\frac{d^2\vec{r}}{dt^2} \qquad \text{Eq. 2.1}$$

The force on each atom can be found by taking the space derivative of the potential energy which is a function of each atom's position:

$$\vec{F} = -\nabla U(r) \qquad \text{Eq. 2.2}$$

The selection of a potential used in an MD simulation is a fundamental portion of the simulation process. A potential needs to be selected so that it provides useful results while not being too computationally expensive. Potentials based on the quantum mechanical properties are the most powerful but are also the most computationally expensive.

The potential selected for this project is an example of a many-body potential energy function. In a many-body potential, the potential energy of each atom is found by summing the contribution of the potential energy between the atom and every other atom in the simulation. Mathematically:

$$E_i = \sum_{j=1, j\neq i}^{N} U_{ij} \qquad \text{Eq. 2.3}$$

where E_i is the potential energy of the atom, N is the total number of atoms and U_{ij} is the potential energy between atoms i and j. The total potential energy of the system is determined by summing all of these potentials together:

$$E_{total} = \sum_{i=1}^{N} \sum_{j=1, j\neq i}^{N} U_{ij} \qquad \text{Eq. 2.4}$$

Since Eq. 2.4 involves a double summation over all particles, without optimization, the computational time grows on the order of N^2. Therefore, if the system size doubles, the computational time will increase by a magnitude of four. The computational time needed when using a many-body potential can be reduced by including a cutoff radius. The cutoff radius causes the individual atom's potential energy to be calculated by taking into account only the interaction between that particular atom and others within the predetermined cutoff radius. Proper choice of a cutoff radius can decrease the time dependence of the simulation toward the order of N without sacrificing accuracy. The cutoff radii for the materials studied in this thesis can be found in Table 4.2 on page 22.

Examples of many-body potentials include the Tersoff potential, Tight-Binding Second Moment Approximation (TBSMA), and the embedded-atom method (EAM). The EAM is used in this thesis since it yields accurate results when calculating the properties of metallic systems [4]. The EAM is described in more detail in Section 2.2.1.

2.2.1 Embedded Atom Method

The embedded atom method measures the potential energy of an atom by summing the atom's embedding energy. The embedding energy is defined as the energy needed to move that particular atom's positive nucleus from infinity into the electron cloud created by all other atoms in the simulation. For the EAM, each individual atom's energy is given by:

$$E_i = F_i\left(\sum_{j\neq i} \rho_\alpha\left(r_{ij}\right)\right) + \frac{1}{2}\sum_{j\neq i} \varphi_{\alpha\beta}\left(r_{ij}\right) \qquad \text{Eq. 2.5}$$

where F_i is the embedding function which measures the amount of energy required to embed atom i in the electron density indicated by ρ_α. α and β indicate the element of

atoms i and j respectively. $\varphi_{\alpha\beta}$ is the pair interaction function between atoms α and β separated by a distance of r_{ij}.

2.3 Integration

For atoms to move in a molecular dynamics simulation, the forces must be integrated. Molecular dynamic simulations can include millions of atoms; systems with millions of atoms are difficult to solve analytically. Therefore, a numerical integration method is applied to the system. Common numerical integration techniques include Verlet algorithm, leap-frog algorithm, Velocity-Verlet, and Beeman's algorithm. The molecular dynamics software used in this thesis, LAMMPS, uses Velocity-Verlet integration. Velocity-Verlet is described in greater detail in Section 2.3.1.

2.3.1 Velocity-Verlet Integration

The Velocity-Verlet algorithm is a method of numeric integration to determine the positions of the atoms after each timestep. Velocity-Verlet is an extension of basic Verlet integration. Basic Verlet is derived by first writing the Taylor expansions for the position functions, one forward in time and one backward in time. These are as follows:

$$r(t+\Delta t) = r(t) + v(t)\Delta t + \frac{1}{2}a(t)\Delta t^2 + \frac{1}{6}b(t)\Delta t^3 + O(\Delta t^4)$$
$$r(t-\Delta t) = r(t) - v(t)\Delta t + \frac{1}{2}a(t)\Delta t^2 - \frac{1}{6}b(t)\Delta t^3 + O(\Delta t^4) \qquad \text{Eq. 2.6}$$

If these two are added together:

$$r(t+\Delta t) = 2r(t) - r(t-\Delta t) + a(t)\Delta t^2 + O(\Delta t^4) \qquad \text{Eq. 2.7}$$

Eq. 2.7 gives the position after time t as a function of the current position, the previous timestep position, and the acceleration with a truncation error of order Δt^4.

An issue with basic Verlet integration is that the prior position, $r(t-\Delta t)$, is not defined for the first timestep. Velocity-Verlet solves this problem by explicitly incorporating the velocities of the atoms:

$$r(t+\Delta t) = r(t) + v(t)\Delta t + \frac{1}{2}a(t)\left(\Delta t\right)^2$$

$$v\left(t+\Delta t\right) = v(t) + \frac{a(t)+a\left(t+\Delta t\right)}{2}\Delta t \qquad \text{Eq. 2.8}$$

Figure 2.1 shows the basic steps implementing the Velocity-Verlet algorithm.

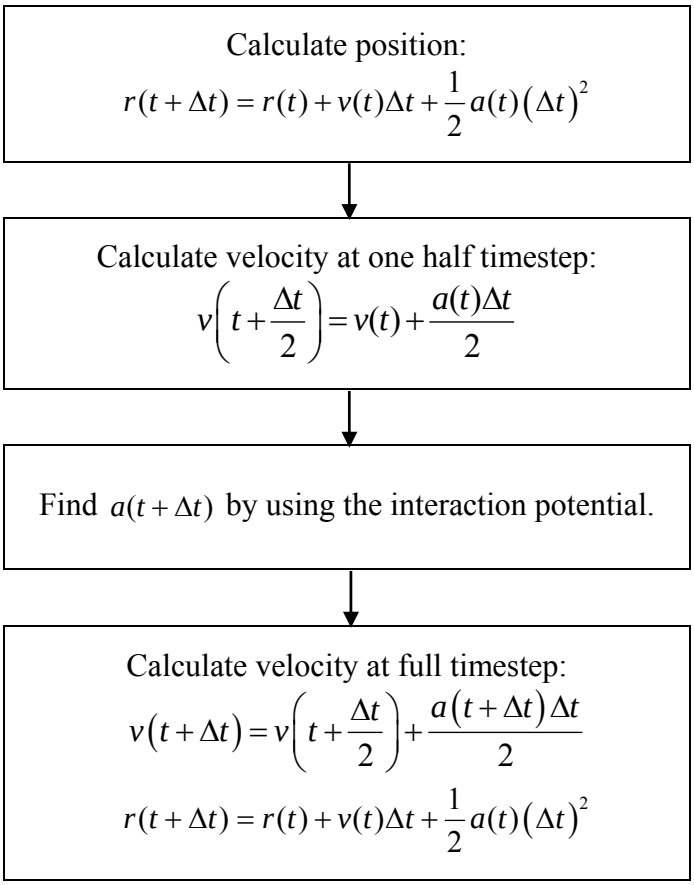

Figure 2.1 Steps to implement the Velocity-Verlet algorithm

2.4 Constraints

The main constraint of MD simulations involves the expense of CPU time to complete a simulation. Without employing some techniques to reduce the simulation time, the order of simulation time is proportional to the square of the number of atoms. This causes an exponential increase in time expense as the simulation system grows.

Another contributing factor to the time duration of the simulation is the small timestep needed to produce accurate results. Timesteps are generally on the order of femtoseconds to avoid discretization errors. In the application of this thesis, the timestep was chosen to be one femtosecond. Since the timesteps are so small, time-dependent variables sometimes need to assume larger than normal values to achieve the desired results in a reasonable time. Due to this constraint, in this research the strain rate is set at 10^8 s^{-1}. This strain rate is much larger than the strain rates applied to physical specimens when completing experimental work.

2.5 Summary

With the advent of powerful personal computers, molecular dynamic simulations have gained popularity as some calculations can be completed locally. For larger simulations, calculations can be parallized by decomposing the simulation in different ways. All molecular dynamics simulations need to include both a potential function to find the forces on each atom and a numerical integration technique to evaluate the motion of the atoms. In this thesis, the embedded atom method was chosen because of its ability to simulate metallic systems well [4]. The Velocity-Verlet algorithm was used to evaluate the motion of the atoms. A flow chart summarizing the molecular dynamics approach can be seen in Figure 2.2.

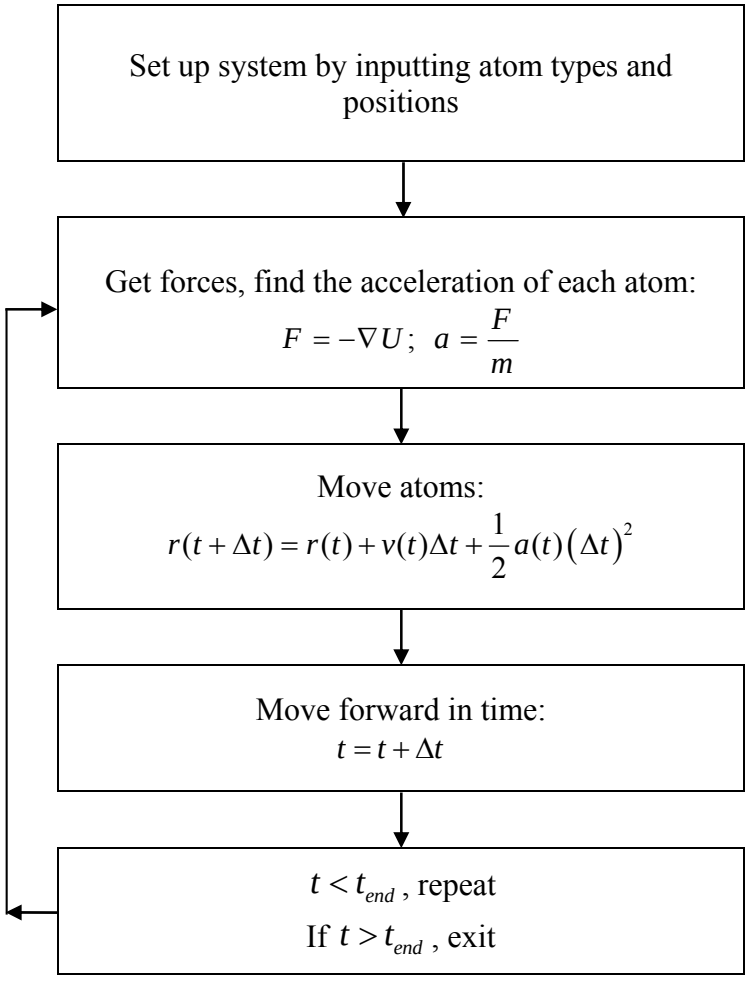

Figure 2.2 Summary of the MD approach – partly reproduced from [5]

3. LITERATURE REVIEW

3.1 Computer Simulations and Theoretical Work

Recently, the number of experiments which investigate the elastic and plastic properties of nanomaterials through molecular dynamics has increased. Understanding the mechanical properties of nanomaterials is necessary if they are to be used in industry applications.

Park and Zimmerman [6] focused on simulations of gold nanowires with a square cross section under tensile stress using two different EAM potentials, Voter-Chen and Foiles. They subjected the nanowires to five different strain rates. Their study found that the Foiles potential provided more accurate measurements of the stacking fault and surface energy. The Voter-Chen potential was found to produce results that overestimate the ductility of the nanowire. This overestimate caused the nanowires not to develop atom-thick chains in the necking region which have been experimentally observed [7].

In addition, Park and Zimmerman looked at the fracture properties of the nanowires. They found that the yield strain increased with decreasing cross-sectional area, and that the fracture strain increased with both increasing cross-sectional area and loading rate. Additionally, at strain rates lower than 10^9 s^{-1}, yield stress increased with decreasing cross-sectional area.

In a similar study, Koh et al. [8] studied the effects of strain rates and temperature on the mechanical properties of cylindrical platinum nanowires being subjected to uniaxial tensile strain. The diameter of the nanowires was approximately 1.4 nm. The study was conducted on infinitely long nanowires indicating the use of periodic boundary

conditions in the direction of strain. Strain rates of 0.04%, 0.4%, and 4.0% ps^{-1} were applied to wires at simulation temperatures of 50 K and 300 K. The temperature increase from 50 K to 300 K was found to be characterized by an increase in ductility while the 50 K wires exhibited brittle slips and rupture. The researchers attributed this to the larger vibrational amplitude of the atoms at 300 K.

In addition, Koh et al. investigated the elastic modulus of the nanowires through graphical methods. They found that the elastic modulus of the nanowires was 50% - 75% that of the bulk materials. The wires which were simulated at 300 K exhibited a lower modulus, while the wires simulated at 50 K were found to have a higher elastic modulus.

Another molecular dynamics study was conducted by Koh and Lee [9] on the mechanical response of face-centered cubic (fcc) metallic nanowires using the Sutton-Chen potential. Specifically, gold and platinum nanowires were investigated with diameters of 2, 4, and 6 nm. The nanowires were subjected to strain rates of 4.0×10^{8}, 4.0×10^{9}, and 4.0×10^{10} s^{-1}.

The study found that the percentage contraction of the nanowires was directly proportional to the percentage of atoms on the surface. That is, the smaller the diameter of the wires, the more the wire contracted upon relaxation. The authors noted that although the initial tensile stresses were acknowledged in other works, no explanation of the reasons behind the initial stresses had been discussed.

In another simulation, Leach, McDowell, and Gall [10] investigated the deformation of silver nanowires ranging in diameter from 1 to 25 nm and varying cross-sectional shapes. The three cross-sectional shapes that they investigated were: rhombic, truncated rhombic, and pentagonal. These shapes correspond to the two different approaches of creating nanowires: top-down and bottom-up fabrication. Top-down fabrication is when a nanowire is created from bulk material, while bottom-up fabrication is when a nanowire is grown thorough chemical or molecular assembly. Top-down

fabrication corresponds to rhombic and truncated-rhombic geometry while bottom-up fabrication corresponds to a pentagonal nanowire. The nanowires were stretched to failure using the Voter-Chen potential.

When investigating how the diameter affects the yield strength, Leach, McDowell, and Gall found that as the diameter decreased, the yield strength increased. This result is in agreement with the previous work cited from Park and Zimmerman [6].

Leach, McDowell and Gall also looked at the deformation mechanism and how it affected the fracture of the nanowire and its mechanical properties. Specifically, they investigated the difference between the truncated-rhombic nanowires, which contain both {100} and {111} side surfaces, and the rhombic nanowires which exclusively contain {111} side surfaces. The {100} surfaces have more surface energy than {111} surfaces causing the surface energy in the truncated-rhombic nanowires to be greater than the rhombic nanowires. The increased surface energy caused a larger compressive surface stress in the truncated-rhombic nanowires in comparison to the rhombic nanowires. The researchers found that after an initial stacking fault deformation, the nanowires followed different paths to failure. The rhombic nanowires main deformation mechanism was twinning and the wires elongated more than 40% before failure. The truncated-rhombic nanowires, which contain both types of surfaces, deformed through partial dislocation motion. The truncated-rhombic nanowires deformed considerably less (a little over 20%) than the rhombic nanowires.

In theoretical work, Wang and Li [11] investigated the elastic modulus of nanowires based on the bulk and surface volumes. Two effects were included: equilibrium strain and surface stress. The researchers remarked that the deformation process used to calculate Young's modulus could cause a change in the apparent value since the different processes cause different changes in length and surface area.

Wang and Li's work included two effects that nanowires' modified lattice parameter can have on Young's modulus. First, a compressive equilibrium strain in the core decreases Young's modulus. Second, a positive surface stress in the surface increases Young's modulus. They concluded that since these two effects are in opposition, the ratio of bulk material to surface material plays a key role in Young's modulus. The theoretical work was validated by comparing their results to experimental results for gold and silver nanowires.

In another simulation, Diao, Gall, and Dunn [12] investigated the free surface effects and elastic properties of square gold nanowires ranging in diameter from 1.5 to 6.0 nm. They used the modified embedded atom method potential developed by Daw and Baskes [4].

Diao, Gall, and Dunn used two different methods to calculate Young's modulus. One used the virial stress and one used an energy method based on continuum mechanics. In each case, the nanowires were relaxed to an initial structure before Young's modulus was calculated. The nanowires were found to contract due to their large surface area to volume ratio. The researchers referred to this contraction as the equilibrium strain of the nanowire. Below 20 nm equilibrium strain sharply decreased from above -5% to below -30%. At the lower equilibrium strains, the nanowire shifted in structure from an fcc structure with a lattice constant of 4.070 Å to a bct structure. For a square nanowire with initial cross-sectional dimensions of 1.83 nm x 1.83 nm, the lattice constant in the x_1 direction became 2.824 Å and the lattice constant in the x_2 and x_3 directions became 4.758 Å. This rearrangement was found to dramatically increase the Young's modulus of the nanowires.

3.2 Physical Experiments

Wu, Heidelberg, and Boland [13] conducted physical experiments investigating the mechanical properties of gold nanowires. This paper presents a method which the

authors report unambiguously measures mechanical properties including Young's modulus and yield strength.

The nanowires Wu, Heidelberg, and Boland created ranged from 40 nm to 250 nm in diameter. They found that the diameter of the wire had little to no effect on the elastic modulus at these sizes. The average elastic modulus was determined to be 70 ± 11 GPa which is slightly lower than the bulk value reported for gold of 78 GPa [14].

Unlike the elastic modulus results, they found that the yield strength increased with decreasing diameter. This finding is consistent with sources [6] and [10]. The average yield strengths were found to be 3.5 ± 1.1 GPa and 5.6 ± 1.4 GPa for diameters of 200 nm and 40 nm, respectively. The researchers indicated that they believe the increase in strength is due to the reduced number of defects in the nanowires in comparison to bulk materials.

Jing, Duan, Sun, et al. [15] performed a physical test on silver nanowires of diameters ranging from 20 to 140 nm. They found that the elastic modulus of nanowires with diameters below 100 nm increased sharply. At diameter sizes larger than 100 nm, they found that the elastic modulus approached a constant value. Jing, Duan, Sun, et al. introduced theoretical analysis that included the surface effects of an oxidation layer which had developed on the nanowire. The authors warned against an attempt to compare the modulus they obtained experimentally with simulation results as the composition, especially at the surface, was more complex than pure silver.

3.3 Summary

Both physical and computer experiments have been performed on metallic nanowires. These experiments looked at the effect of the diameter on many mechanical properties including the equilibrium strain, yield stress, and elastic modulus. The effect of diameter on the yield strength is well documented. References [6], [10], and [13] all found that as the diameter decreased, the yield strength increased.

The effect of diameter on the contraction of a nanowire is unambiguous as both references [8] and [12] report that as the diameter decreases, the contraction increases. This has been attributed to the outer surface of the nanowires. As a nanowire's surface area to volume ratio increases, the effect that the surface atoms have increases.

The effect of the diameter on Young's modulus is less well understood. Reference [9] found that for platinum nanowires, the elastic modulus was 50% that of bulk materials at 300 K. For gold nanowires, reference [13] found that the diameter had no effect on Young's modulus and that the Young's modulus was only slightly lower for nanowires in comparison to bulk materials. Theoretical work cited in reference [11] predicts that Young's modulus of gold nanowires should increase significantly when the diameter is less than 60 nm. Reference [15] found that in physical experiments on silver nanowires, the modulus increased with decreased diameter, but the authors attributed the increase to an oxidation layer on the outside of the nanowire. Finally, reference [12] found that the modulus of <100> gold nanowires dramatically increased when the diameter is below 2 nm. However, the modulus increase may be due to a transition from an fcc structure to a bct structure during minimization.

4. MOTIVATION AND EXPERIMENTAL SETUP

4.1 Motivation

Mechanical properties such as Young's modulus, yield stress, and yield strain are generally considered intrinsic properties for metallic systems. Intrinsic properties are properties that are not size or shape dependent. However, on the nano-scale, the mechanical properties of metallic systems exhibit size and shape dependence. These size and shape dependencies give rise to interesting engineering opportunities. If the science behind the mechanisms which cause the variations is fully developed, materials may be engineered to have the desired physical properties based on application.

The most common way to find the mechanical properties of materials is to run physical experiments. These experiments can yield both quantitative data and qualitative data such as pictures of the deformation process and microscopy images. However, there is a limit to how much information can be gained from imaging during and after the deformation process. Microscopy can only zoom in so far, and it is difficult to gain data about the interior of the structure. As an alternative to physical experiments, computer experiments can be completed which allow scientists to view the movement of individual atoms throughout the structure. The computer programs can also calculate a large number of physical quantities at very small timesteps. Through the post-processing of results from a computer simulation, insight into the deformation process can be gained which is impossible to obtain through experimentation.

Significant work has been done to investigate the values of the various mechanical properties for metallic nanowires. However, there are some key differences that set this work apart. First, only one work cited thus far, reference [10], investigated

the effect that different cross-sectional shapes have on the deformation mechanism. Secondly, most previous work has focused primarily on the mechanical properties of nanowires composed of a single metal. This work not only investigates the deformation mechanism, it also encompasses a breadth of materials, shapes, and sizes. Lastly, this work also includes two materials, nickel and palladium, which are rarely studied. To this researcher's knowledge a study of this size across a range of materials, shapes, and diameters has not been completed.

4.2 MD Software

Computations for this thesis were carried out in the software package LAMMPS [3]. LAMMPS, which stands for Large-scale Atomic/Molecular Massively Parallel Simulator, is an open-source project distributed by Sandia National Laboratories. LAMMPS can be run on a single processor or run in parallel utilizing message-passing parallelism (MPI). LAMMPS spatially decomposes the system when running in parallel. It is written in C++ which allows it to be highly portable. It can be compiled and run on a multitude of operating systems and machines. This portability allowed for small calculations to be run on a local computer. Calculations requiring more than a day of computing time were sent to Indiana University's supercomputer, Big Red, to be run in parallel. For the tasks sent to Big Red, 4 to 64 nodes were employed for the calculations. The number of nodes utilized was dependent on the size of the computing task.

4.3 Potential Choice and Description

The molecular dynamics simulations and potential energy calculations performed in this thesis utilized the EAM as described in Section 2.2.1 on page 8. The Foiles potential [1] was used because it produces more accurate results than other potentials when measuring the surface energy of metals [6]. The Foiles potential was developed by fitting the potential to the parameters found in Table 4.1. The parameters are: equilibrium lattice constant (a_o), sublimation energy (E_{sub}), bulk modulus (B), elastic constants (C_{11}, C_{12}, C_{44}), and vacancy-formation energy (E_v^f). Where two values are

listed in the table, the top number is the value calculated from the Foiles potential, and the bottom number is the experimental value. This table was reproduced from [1].

Table 4.1 Fitting parameters for the Foiles potential

	Gold	Silver	Copper	Nickel	Palladium	Platinum
a_o (Å)	4.08	4.09	3.615	3.52	3.89	3.92
E_{sub} (eV)	3.93	2.85	3.54	4.45	3.91	5.77
B (10^{12} erg/cm^3)	1.67	1.04	1.38	1.804	1.95	2.83
C_{11}(10^{12} erg/cm^3)	1.83	1.29	1.68	2.35	2.21	3.04
	1.86	1.24	1.70	2.465	2.341	3.47
C_{12}(10^{12} erg/cm^3)	1.59	0.91	1.24	1.53	1.83	2.72
	1.57	0.954	1.225	1.473	1.76	2.51
C_{44}(10^{12} erg/cm^3)	0.45	0.57	0.79	1.33	0.73	0.72
	0.42	0.461	0.758	1.247	0.712	0.765
E_v^f (10^{12} erg/cm^3)	1.04	0.97	1.33	1.71	1.58	1.77
	0.9	1.1	1.3	1.7	1.54	1.6

A cutoff radius is used in conjunction with each potential to ensure that the simulation time does not grow on the order of N^2. Steps are taken to ensure that the benefit of decreased computation time does not come at the cost of a significant loss in accuracy. For the EAM, the cutoff radii are generally chosen to be a distance in between the third and fourth nearest neighbor in the crystal lattice. The cutoff radii, as read directly from the potential files, are listed in Table 4.2.

An additional reason to use the potentials developed in [1] is the fact that the authors developed potentials for six different face-centered cubic metals. This allows for a comparison of behavior across different materials.

Table 4.2 Cutoff radii for all six metals

Material	Cutoff Radius (nm)
Gold	0.550
Silver	0.555
Copper	0.495
Nickel	0.480
Palladium	0.530
Platinum	0.530

4.4 Structure Minimization Motivation and Setup

In bulk materials the lowest energy state is at zero strain with consistent lattice parameters. However, the lowest energy state for the surfaces of these materials does not correspond to the bulk lattice parameters. The differing lattice parameters are due to the surface atoms' energies not being similar to their neighbors. The surface atoms have a lower coordination number meaning there is an availability of open bonds on the surfaces. This causes the surface atoms to be in a higher energy state. The high energy state causes the atoms to have the propensity to contract. A snapshot and cross section of a nanowire with the atoms colored by potential energy can be seen in Figure 4.1 and Figure 4.2. The blue core atoms are at a lower energy state than the surface atoms, as exemplified by their color.

In bulk materials, this contraction effect is so small that it cannot be seen because the number of atoms in the core of the material is orders of magnitude larger than the number of atoms on its surface. To illustrate this, consider a gold nanowire (lattice spacing of 0.408 nm) with a square cross section of width W and a length of 6W. This is similar in proportions to the nanowire depicted in Figure 4.1. If the surface is identified as the volume to a depth of one half of a lattice spacing from the surface while the rest of the volume is considered core material, the ratio of surface atoms to bulk atoms can be estimated. Table 4.3 shows the percentage of what is considered core material for

varying widths. In addition, Table 4.3 shows the surface area to volume ratio for different widths.

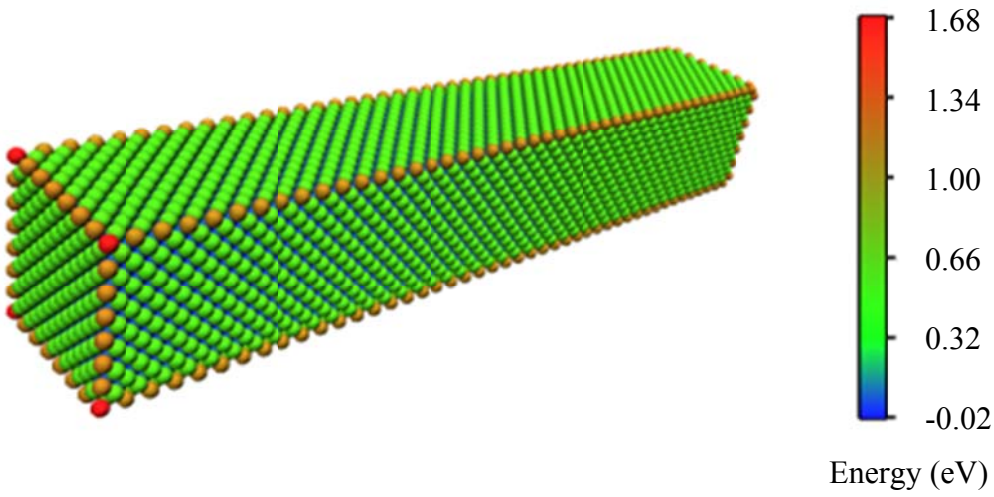

Figure 4.1 2.5 x 2.5 x 16 nm nickel nanowire with atoms colored by potential energy - figure created with the aid of VMD visualization software [16]

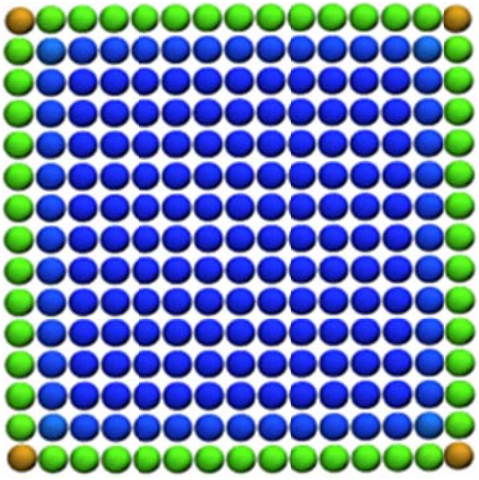

Figure 4.2 Cross-sectional view of the nickel nanowire from Figure 4.1

Table 4.3 Percentage of core material and surface area to volume ratio based on width of a gold sample with a length of 6W

W (nm)	Percentage of core material	Surface area to volume ratio (nm^{-1})
100000	100.00%	0.0000433
10000	99.99%	0.000433
1000	99.90%	0.00433
100	99.05%	0.0433
10	90.81%	0.433
1	34.70%	4.33

As can be seen in Table 4.3, as materials decrease below a critical cross-sectional size, the percentage of surface atoms increases significantly. Even at the micrometer scale, the percentage of bulk material is still above 99%. In gold, extreme differences are exhibited when side lengths are between 1 nm and 10 nm. The other fcc metals discussed in this thesis are similar as their lattice constants are all between 0.352 nm (nickel) and 0.409 nm (silver).

To account for this contraction before conducting the molecular dynamics simulations on the nanowires, many test structures were created with a decreasing lattice constant along the length of the wires. This lattice size variation can be considered as applying a compressive strain along the length of the wires. Each structure's total bond energy was then minimized by iterative perturbation of the atoms using the conjugate gradient method. As discussed earlier, the strain at which the total bond energy is minimized is referred to as the equilibrium strain.

To accomplish this objective, three preprocessors were developed which created files containing the x, y, and z position of each atom formatted in a LAMMPS-compatible syntax. One preprocessor was created for each cross-sectional shape of nanowire: square, octagonal, and circular. These files were created to produce a structure consistent with the effects of strain levels from -0.300 to 0 in increments of 0.002. The strain was applied by varying the lattice constant in the x direction while scaling the

lattice constant in the y and z directions to keep the volume consistent with the volume of the structure at 0 strain. The constant volume assumption was used rather than Poisson's ratio as it yielded structures closer to the final minimized structure.

Each structure was then minimized in LAMMPS using the conjugate gradient method with the Foiles potential [1]. Periodic boundaries were applied in the x direction while free shrink-wrapped boundaries were applied in the y and z directions to prevent loss of atoms during minimization. The energy cutoff for the minimization technique was 1.0×10^{-8}. That is, the solution was considered converged when the difference between the second to last iteration and the last iteration was less than one part in 100 million. The maximum number of iterations allowed was 1,000. Graphs exhibiting this minimization technique can be found in Section 5.1: Structure Minimization on page 37. This structure after minimization is the structure that should be exhibited by the material if created in a laboratory. As such, this minimization procedure was carried out prior to all simulations.

4.5 Energy Method Young's Modulus Setup

The first method used to calculate Young's modulus of each nanowire is derived from basic mechanics concerning the change in potential energy in the nanowire. It is a well-accepted method to determine Young's modulus. As such, it was mainly used to validate the molecular dynamics results. The method that is described in this section will be referred to as the energy method throughout the rest of this thesis.

Once the structure minimization as described in Section 4.4 is completed, the nanowire is in its equilibrium state. Therefore, when stretched, the work done on the nanowire is equal to the change in potential energy:

$$W = \Delta U = \int_0^{\Delta l} F dx \qquad \text{Eq. 4.1}$$

where Δl is the change in length applied to the nanowire. If linear elastic behavior is assumed, before yielding the engineering stress is defined as:

$$\sigma = \frac{F}{A_o} = E\varepsilon \qquad \text{Eq. 4.2}$$

where F is the force applied to the wire, E is Young's modulus, A_o is the initial cross-sectional area, and ε is the strain. Solving for the force in Eq. 4.2 and substituting it into Eq. 4.1 gives:

$$\Delta U = \int_0^{\Delta l} EA_o \varepsilon dx \qquad \text{Eq. 4.3}$$

By switching the limits of integration from length to strain, the following equation is derived:

$$\Delta U = EA_o L_o \int_0^{\varepsilon} \varepsilon d\varepsilon = \frac{1}{2} EV_o \varepsilon^2 \qquad \text{Eq. 4.4}$$

where L_o is the length at equilibrium and V_o is the volume at equilibrium. Rearranging gives:

$$\frac{\Delta U}{V_o} = \frac{1}{2} E\varepsilon^2 \qquad \text{Eq. 4.5}$$

Thus, if the change in potential energy divided by the initial volume is graphed versus the strain, the elastic modulus can be found by fitting a second order polynomial to the data.

4.6 Finding Young's Modulus from Elastic Constants

A second method to validate the molecular dynamics approach involves inverting the stiffness matrix. The stiffness matrix can be constructed by placing the elastic constants found in Table 4.1 into a stiffness tensor:

$$[c] = \begin{bmatrix} C_{11} & C_{12} & C_{12} & 0 & 0 & 0 \\ C_{12} & C_{11} & C_{12} & 0 & 0 & 0 \\ C_{12} & C_{12} & C_{11} & 0 & 0 & 0 \\ 0 & 0 & 0 & C_{44} & 0 & 0 \\ 0 & 0 & 0 & 0 & C_{44} & 0 \\ 0 & 0 & 0 & 0 & 0 & C_{44} \end{bmatrix} \qquad \text{Eq. 4.6}$$

If the stiffness matrix is inverted, the elastic modulus can be found through Eq. 4.7.

$$[C]^{-1} = \frac{1}{E}\begin{bmatrix} 1 & -\nu & -\nu & 0 & 0 & 0 \\ -\nu & 1 & -\nu & 0 & 0 & 0 \\ -\nu & -\nu & 1 & 0 & 0 & 0 \\ 0 & 0 & 0 & 1-2\nu & 0 & 0 \\ 0 & 0 & 0 & 0 & 1-2\nu & 0 \\ 0 & 0 & 0 & 0 & 0 & 1-2\nu \end{bmatrix} \quad \text{Eq. 4.7}$$

In Eq 4.7, E refers to Young's modulus and ν is Poisson's ratio.

4.7 Molecular Dynamics Setup

After finding the equilibrium strain, a pre-processor was used to confirm that no atom crossed the periodic boundary along the x axis during the minimization process. This processor also found the length of the wires and automatically created the control file to set up and run the simulation in LAMMPS.

Before running any molecular dynamics, the periodic boundary conditions were removed along the x direction. For the remainder of the MD process, shrink-wrapped boundary conditions were applied in all directions for the wire.

First, the ends of the nanowire in the x direction were held at zero force. The remainder of the atoms was set to a velocity corresponding to a temperature of 300 K. The velocities were assigned randomly to create an ensemble which is consistent with a temperature of 300 K. To ensure equilibrium, the total momentum and angular velocity of the system were kept at zero.

Next, the system was thermally equilibrated using a Nose/Hoover thermostat applied for 20 ps with a timestep of 0.001 ps while keeping the length of the nanowire constant. After thermal equilibration, the Nose/Hoover thermostat was removed and NVE integration applied to track the movement and velocity of the atoms. To apply the tension in the [100] direction, a ramped velocity profile was applied to the nanowires. The velocity profile ramped from 0 at one fixed end to the maximum velocity at the other

end. As discussed in Section 2.4 on page 11, sometimes time dependent variables have to be larger than they would be experimentally to decrease computation time. In this application the strain rate had to be increased beyond what one would expect to use experimentally. As such, the maximum velocity was chosen to be consistent with a strain rate of 10^8 s^{-1} for each wire. The ramped velocity profile is required to avoid shock wave emissions from the loaded end of the nanowire [6].

The total stress was calculated using the stress/atom command in LAMMPS. This command computes the stress tensor for each atom in a group. The group was defined to include all atoms except those within 1 nm of the fixed ends. These atoms were not considered to eliminate effects from the ends being held fixed. The virial keyword was used to remove the kinetic energy contribution to the stress tensor. The stress tensor has six components, one in each material direction. Only the S_{xx} component was considered as σ_{xx} is the relevant component when considering tensile stress. The sum of every atom's S_{xx} tensor component was stored every 1000 timesteps. The simulation was then allowed to run until fracture of the nanowire.

The stress tensor outputted by LAMMPS is actually in units of pressure*volume. As such, this quantity needed to be divided by the group's volume to obtain the stress. This volume was calculated by assuming the volume of a bulk system (using bulk lattice parameters) containing the number of atoms in the stress group. Since this value was outputted every 1000 timesteps and each timestep was 0.001 ps, the graphs created have a data point for every 1 ps of simulation time.

4.8 Visualization Setup

The visualization for this thesis utilized the open source software Visual Molecular Dynamics (VMD) [16] created at the University of Illinois at Urbana-Champaign. Most pictures utilized the built-in postprocessor for LAMMPS dump files which is provided in the software download. Other, more specific, visualization required post-processing of LAMMPS output beyond the built-in tool.

The postprocessor used to visualize the energy of each atom consists of two separate pieces. First, a C program was developed to extract the structure of the nanowire from a dump file created by LAMMPS. The dump files contain thousands of frames which made manual extraction time prohibitive. These structure files were then run though LAMMPS again to calculate the energy of each atom for every frame. Next, a Tcl script was created to aid in visualization within VMD. The Tcl script utilized the user field in VMD and allowed the atoms to be colored according to scalar values. The values which were used in this case were the energies of the individual atoms.

5. RESULTS AND DISCUSSION

Through using the techniques described in Chapter 4, many mechanical property quantities were calculated for each nanowire configuration. All of the details and discussion of the calculations are expanded upon within this chapter. For data brevity and organization, all major numerical results are summarized at the beginning of this chapter in the subsequent six tables. Each table is dedicated to a single material. Relevant graphs and discussion are provided in the text following Table 5.1 - Table 5.6.

Table 5.1 Mechanical properties of gold nanowires

Material Property	Cross-Sectional Shape		
	Square	Circle	Octagon
1 nm Diameter			
Minimized Strain	-0.2900	-0.3035	-0.3035
Young's Modulus, Energy Method (GPa)	136.260	95.547	90.584
2.5 nm Diameter			
Minimized Strain	-0.050	-0.0230	-0.0235
Yield Stress (GPa)	3.374	4.588	3.451
Yield Strain	0.0822	0.0798	0.0839
Ultimate Strain	0.303	0.310	0.326
Young's Modulus, Graphical Method (GPa)	11.480	19.387	23.130
Young's Modulus, Energy Method (GPa)	12.932	20.596	22.215
5 nm Diameter			
Minimized Strain	-0.0205	-0.0100	-0.0105
Yield Stress (GPa)	2.964	3.483	3.280
Yield Strain	0.0672	0.0790	0.0715
Ultimate Strain	0.778	0.290	0.896
Young's Modulus, Graphical Method (GPa)	28.257	28.201	30.940
Young's Modulus, Energy Method (GPa)	25.714	31.096	32.772
8 nm Diameter			
Minimized Strain	-0.0120	-0.0080	-0.0070
Yield Stress (GPa)	2.965	3.937	3.347
Yield Strain	0.0625	0.0777	0.0692
Ultimate Strain	1.082	1.240	1.172
Young's Modulus, Graphical Method (GPa)	32.079	32.472	35.621
Young's Modulus, Energy Method (GPa)	31.468	31.202	32.350

Table 5.2 Mechanical properties of silver nanowires

Material Property	Cross-Sectional Shape		
	Square	Circle	Octagon
1 nm Diameter			
Minimized Strain	-0.2820	-0.2920	-0.2920
Young's Modulus, Energy Method (GPa)	147.176	111.686	105.885
2.5 nm Diameter			
Minimized Strain	-0.0140	-0.0125	-0.0110
Yield Stress (GPa)	5.605	4.613	5.448
Yield Strain	0.0890	0.0875	0.0935
Ultimate Strain	0.486	0.353	0.280
Young's Modulus, Graphical Method (GPa)	41.402	44.607	25.273
Young's Modulus, Energy Method (GPa)	42.050	41.348	41.738
5 nm Diameter			
Minimized Strain	-0.0070	-0.0055	-0.0050
Yield Stress (GPa)	5.165	5.354	5.472
Yield Strain	0.0813	0.0963	0.0944
Ultimate Strain	0.661	0.291	0.532
Young's Modulus, Graphical Method (GPa)	46.601	43.540	45.446
Young's Modulus, Energy Method (GPa)	48.954	49.385	51.597
8 nm Diameter			
Minimized Strain	-0.0040	-0.0035	-0.0030
Yield Stress (GPa)	5.136	6.434	5.818
Yield Strain	0.0801	0.0974	0.0946
Ultimate Strain	0.992	1.610	0.832
Young's Modulus, Graphical Method (GPa)	48.612	49.280	50.555
Young's Modulus, Energy Method (GPa)	55.712	52.151	54.366

Table 5.3 Mechanical properties of copper nanowires

Material Property	Cross-Sectional Shape		
	Square	Circle	Octagon
1 nm Diameter			
Minimized Strain	-0.2720	-0.2835	-0.2760
Young's Modulus, Energy Method (GPa)	173.572	134.489	152.380
2.5 nm Diameter			
Minimized Strain	-0.0225	-0.0305	-0.0250
Yield Stress (GPa)	7.939	8.410	7.776
Yield Strain	0.1052	0.1133	0.1112
Ultimate Strain	0.437	0.337	0.353
Young's Modulus, Graphical Method (GPa)	34.220	26.823	31.907
Young's Modulus, Energy Method (GPa)	41.753	34.579	38.224
5 nm Diameter			
Minimized Strain	-0.0100	-0.0115	-0.0105
Yield Stress (GPa)	7.651	7.965	7.440
Yield Strain	0.0976	0.1000	0.0969
Ultimate Strain	1.082	0.830	0.961
Young's Modulus, Graphical Method (GPa)	49.848	48.137	50.470
Young's Modulus, Energy Method (GPa)	56.500	49.733	51.653
8 nm Diameter			
Minimized Strain	-0.0065	-0.0065	-0.0060
Yield Stress (GPa)	7.527	7.200	7.395
Yield Strain	0.0941	0.0957	0.0932
Ultimate Strain	1.776	1.168	0.904
Young's Modulus, Graphical Method (GPa)	58.987	52.781	55.133
Young's Modulus, Energy Method (GPa)	54.474	57.092	60.372

Table 5.4 Mechanical properties of nickel nanowires

Material Property	Cross-Sectional Shape		
	Square	Circle	Octagon
1 nm Diameter			
Minimized Strain	-0.2710	-0.2805	-0.2730
Young's Modulus, Energy Method (GPa)	265.720	169.504	208.661
2.5 nm Diameter			
Minimized Strain	-0.0105	-0.0150	-0.0135
Yield Stress (GPa)	14.093	11.356	12.454
Yield Strain	0.1013	0.1075	0.1097
Ultimate Strain	0.375	0.267	0.316
Young's Modulus, Graphical Method (GPa)	88.497	71.042	79.351
Young's Modulus, Energy Method (GPa)	97.319	80.826	88.234
5 nm Diameter			
Minimized Strain	-0.0050	-0.0060	-0.0060
Yield Stress (GPa)	13.807	12.935	13.290
Yield Strain	0.1001	0.1031	0.1032
Ultimate Strain	0.786	0.709	0.704
Young's Modulus, Graphical Method (GPa)	103.289	99.754	96.643
Young's Modulus, Energy Method (GPa)	110.847	104.682	98.365
8 nm Diameter			
Minimized Strain	-0.0035	-0.0035	-0.0035
Yield Stress (GPa)	13.119	14.343	13.308
Yield Strain	0.0946	0.1010	0.1001
Ultimate Strain	0.974	0.840	1.274
Young's Modulus, Graphical Method (GPa)	110.405	106.797	109.165
Young's Modulus, Energy Method (GPa)	103.627	111.292	108.587

Table 5.5 Mechanical properties of palladium nanowires

Material Property	Cross-Sectional Shape		
	Square	Circle	Octagon
1 nm Diameter			
Minimized Strain	-0.2790	-0.2910	-0.2810
Young's Modulus, Energy Method (GPa)	182.026	123.974	146.074
2.5 nm Diameter			
Minimized Strain	-0.0410	-0.0400	-0.0325
Yield Stress (GPa)	7.456	6.106	6.669
Yield Strain	0.1179	0.1173	0.1105
Ultimate Strain	0.328	0.612	0.472
Young's Modulus, Graphical Method (GPa)	20.746	17.890	24.899
Young's Modulus, Energy Method (GPa)	24.947	20.644	28.527
5 nm Diameter			
Minimized Strain	-0.0165	-0.0150	-0.0130
Yield Stress (GPa)	6.756	7.056	6.072
Yield Strain	0.0931	0.0932	0.0890
Ultimate Strain	0.678	0.679	0.863
Young's Modulus, Graphical Method (GPa)	43.967	41.477	44.387
Young's Modulus, Energy Method (GPa)	45.986	43.989	47.606
8 nm Diameter			
Minimized Strain	-0.0095	-0.0080	-0.0080
Yield Stress (GPa)	6.480	5.946	5.914
Yield Strain	0.0863	0.0846	0.0822
Ultimate Strain	0.928	1.084	0.792
Young's Modulus, Graphical Method (GPa)	53.201	49.933	52.749
Young's Modulus, Energy Method (GPa)	54.156	57.625	47.460

Table 5.6 Mechanical properties of platinum nanowires

Material Property	Cross-Sectional Shape		
	Square	Circle	Octagon
	1 nm Diameter		
Minimized Strain	-0.2805	-0.2945	-0.2820
Young's Modulus, Energy Method (GPa)	191.805	127.703	143.253
	4 nm Diameter		
Minimized Strain	-0.0435	-0.0225	-0.0235
Yield Stress (GPa)	5.219	4.716	4.536
Yield Strain	0.1015	0.0878	0.0806
Ultimate Strain	0.587	0.557	0.754
Young's Modulus, Graphical Method (GPa)	15.573	25.529	29.130
Young's Modulus, Energy Method (GPa)	15.020	27.049	27.287
	5 nm Diameter		
Minimized Strain	-0.0305	-0.0210	-0.0175
Yield Stress (GPa)	4.966	5.046	4.318
Yield Strain	0.0877	0.0802	0.0752
Ultimate Strain	1.175	0.725	1.194
Young's Modulus, Graphical Method (GPa)	29.095	32.729	31.555
Young's Modulus, Energy Method (GPa)	24.023	30.915	29.714
	8 nm Diameter		
Minimized Strain	-0.0170	-0.0100	-0.0105
Yield Stress (GPa)	4.898	4.662	4.455
Yield Strain	0.0757	0.0751	0.0690
Ultimate Strain	1.063	0.691	1.010
Young's Modulus, Graphical Method (GPa)	38.895	43.081	44.597
Young's Modulus, Energy Method (GPa)	34.334	37.055	38.138

5.1 Structure Minimization

Each structure was minimized in accordance with the procedure described in the section entitled Structure Minimization Motivation and Setup on page 22. Multiple structures were created by decreasing the lattice constant along the length of the nanowires. Varying the lattice constant along the [100] direction can be understood as applying compressive strain on the nanowire. These structures were minimized in LAMMPS by iterative perturbation using the conjugate gradient method. Figure 5.1 shows a curve resulting from one of these minimization procedures. In this example, the equilibrium strain is said to be -0.0115 as this is the strain value which corresponds to the minimum total energy.

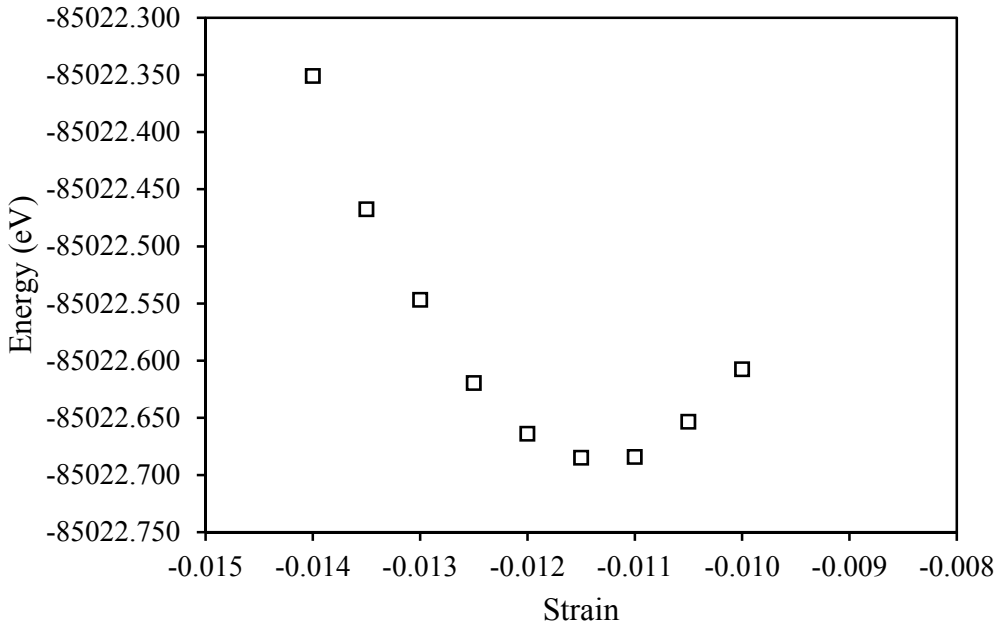

Figure 5.1 Close up of minimum energy region during the determination of the equilibrium strain of the 5 nm diameter circular copper nanowire

As previously discussed, this contraction is due to a large surface area to volume ratio. The surface atoms have a tendency to contract since they are at a higher energy state. Thus, there are two competing factors in the contraction: the atoms on the surface drop in energy due to contraction, while the internal atoms increase in energy due to

contraction. Figure 5.2 shows the cross section of a 2.5 nm nickel nanowire before contraction (left) and after contraction (right).

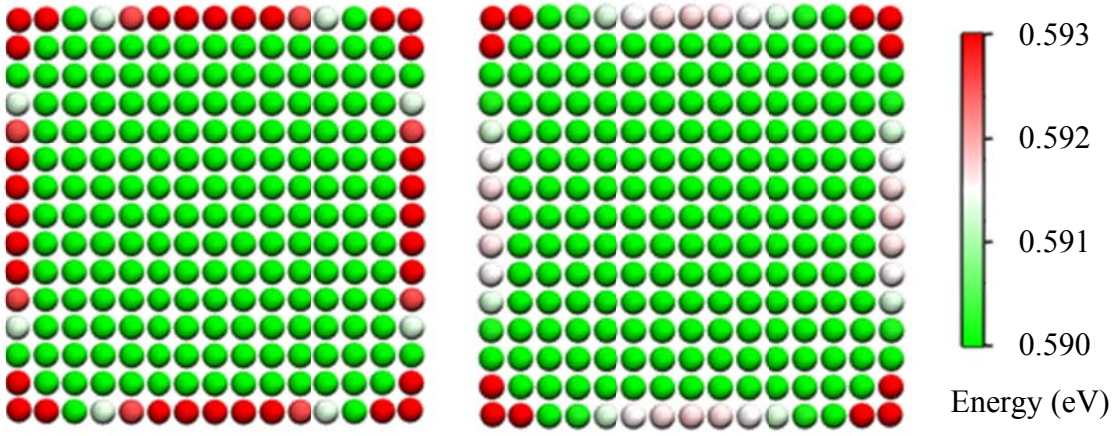

Figure 5.2 2.5 nm nickel nanowire cross sections before minimization at $\varepsilon = 0$ (left) and after minimization at $\varepsilon = -0.0105$ (right)

Both cross sections are colored using the same scale. Note that the scale was chosen to highlight the differences in energy of the surface atoms. As such, atoms colored in green may have an energy below 0.590 eV. The nanowire on the left shows the higher energy of some surface atoms which are colored in red. At the equilibrium strain, the same atoms exhibit a decrease in energy as exemplified by the color change to white.

Next, the color scale bar was adjusted to show the change in energy for the central atoms. In Figure 5.3, the same nanowire cross section is shown before any contraction (left) at $\varepsilon = 0$ and after minimization (right) at the equilibrium strain of $\varepsilon = -0.0105$. The X pattern in the core of the nanowire is due to the corner atoms constricting toward the core to lower the energy of the system. The constricting corner atoms cause the strain energy along this axis to increase. Figure 5.3 shows that the structure before minimization (left) actually contains more atoms at lower energy states than the structure at equilibrium strain (right). This shows that the internal atoms actually have a net increase in energy when the nanowire is contracted to the equilibrium strain. However,

the overall energy of the nanowire at ε = -0.0105 is smaller than the energy at ε = 0, indicating that decrease in energy of the surface dominates the increase in energy of the core.

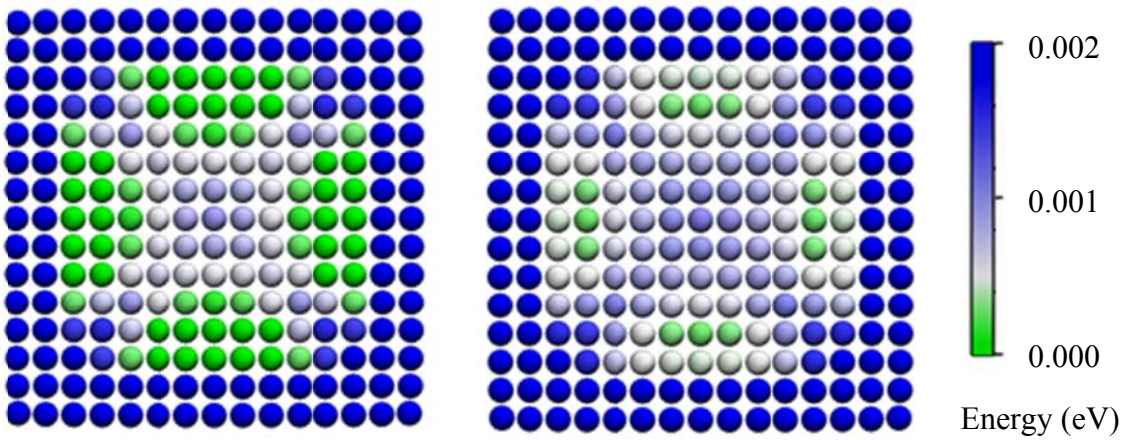

Figure 5.3 2.5 nm nickel nanowire cross sections before minimization at ε = 0 (left) and after minimization at ε = -0.0105 (right)

Figure 5.3 reveals many energetically distinct areas within the cross section of the nickel nanowire. Previous studies [9-11] have considered only two areas, the surface and the center. It was previously assumed that the surface would have residual compressive stresses while the center would have residual tensile stresses. However, the real situation is more complex. In the case of the square cross section, there are three distinct areas with two axes of symmetry.

Figure 5.2 and Figure 5.3 also demonstrate the competing factors which result in an overall contraction in nanowires. Since the surface atoms are the driving force of the contraction, the nanowires with a smaller diameter are expected to contract more. That is, they will have a lower equilibrium strain. Figure 5.4, Figure 5.5, and Figure 5.6 confirm this expectation.

The diameter dependence was expected prior to completion of minimization as many sources have found similar trends. However, not much work has been done investigating the dependence of equilibrium strain on the cross-sectional shape. For this case, the discussion will be restricted to the square and octagonal cross sections since they possess well-defined crystallographic surfaces. For the <100> nanowires created in this thesis, the nanowires with a square cross section contain {010} and {001} surfaces. These two surfaces are energetically the same. The octagonal nanowires contain {011} surfaces in addition to the {010} and {001} surfaces.

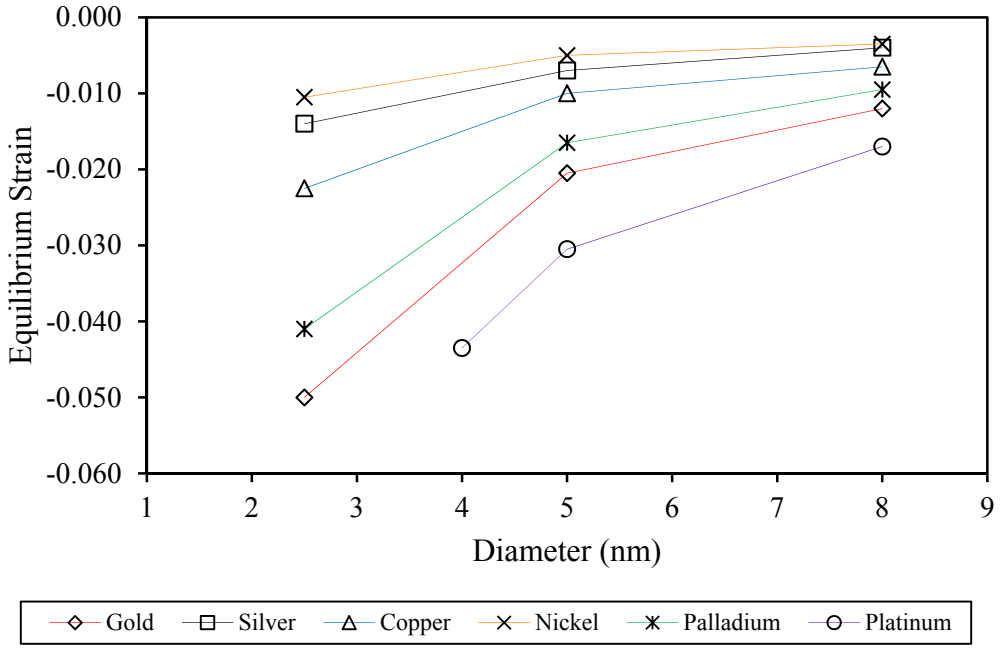

Figure 5.4 Equilibrium strain for square cross section nanowires

Figure 5.7 shows an octagonal nickel nanowire with a diameter of 2.5 nm. This nanowire is the same diameter as the nanowire depicted in Figure 5.2 and Figure 5.3.

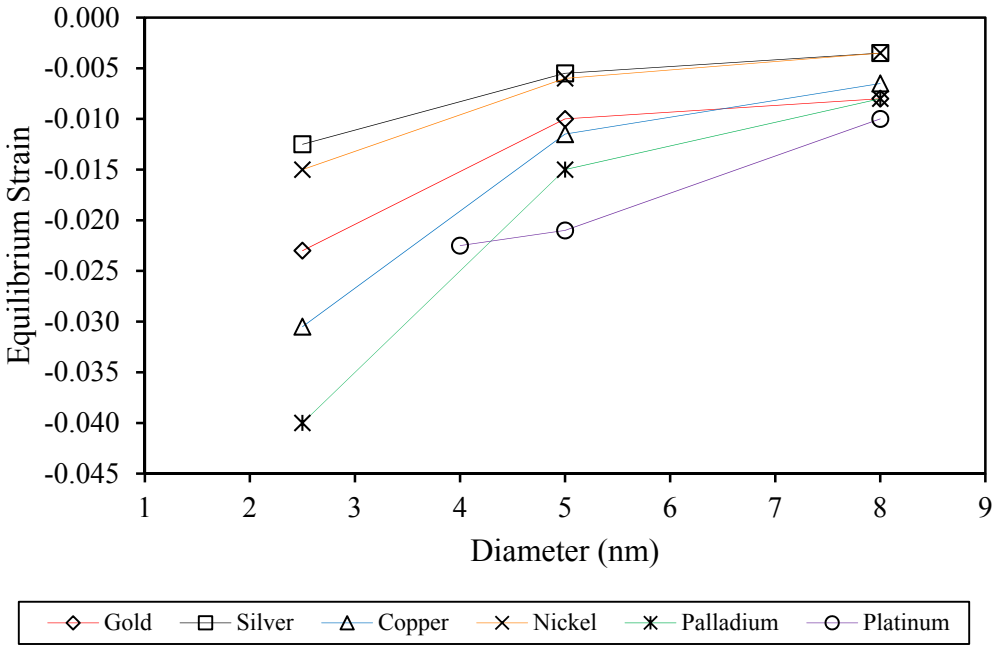

Figure 5.5 Equilibrium strain for circular cross section nanowires

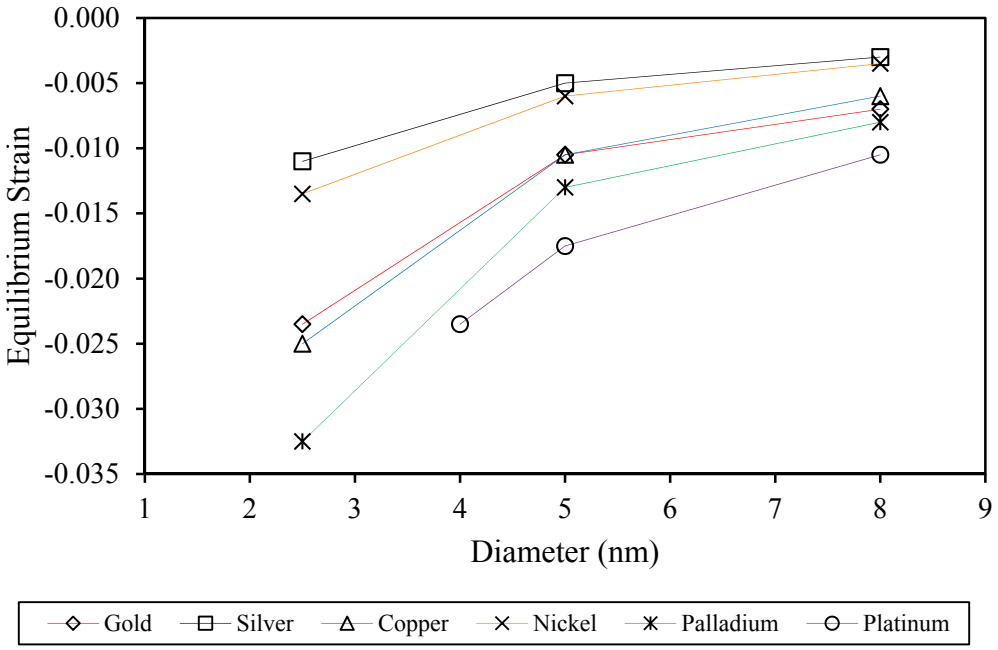

Figure 5.6 Equilibrium strain for octagonal cross section nanowires

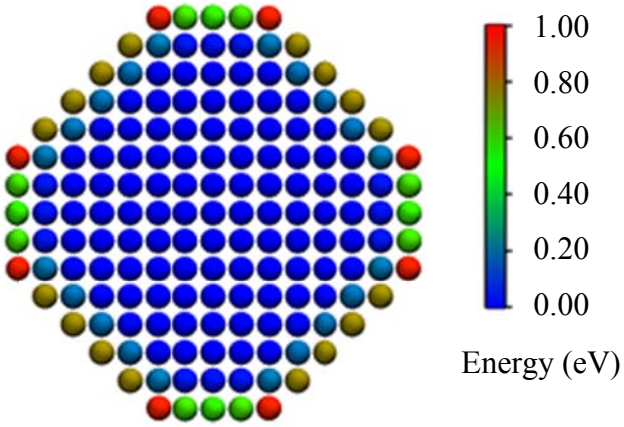

Figure 5.7 2.5 nm diameter octagonal nickel nanowire showing the higher energy {011} surfaces

As can be seen in Figure 5.7, the {011} surfaces are at a higher energy than the {100} surfaces. Since nanowires contract due to higher energy surfaces, one would expect that all octagonal cross section nanowires would constrict more than those with a square cross section. However, this is not necessarily the case. Figure 5.8 shows that, in the six materials studied, the majority of octagonal nanowires constrict less than the same-sized square nanowires.

This is not a size-dependent phenomenon as the other sizes studied show similar trends. The graphs for the 5 nm and 8 nm diameters can be found in the Appendix on page 91. To further investigate this phenomenon, the two extreme cases will be considered: gold and nickel. Gold constricts considerably more when the cross section is square in shape while nickel constricts less. Figure 5.9 shows both gold and nickel nanowires square cross sections at zero strain.

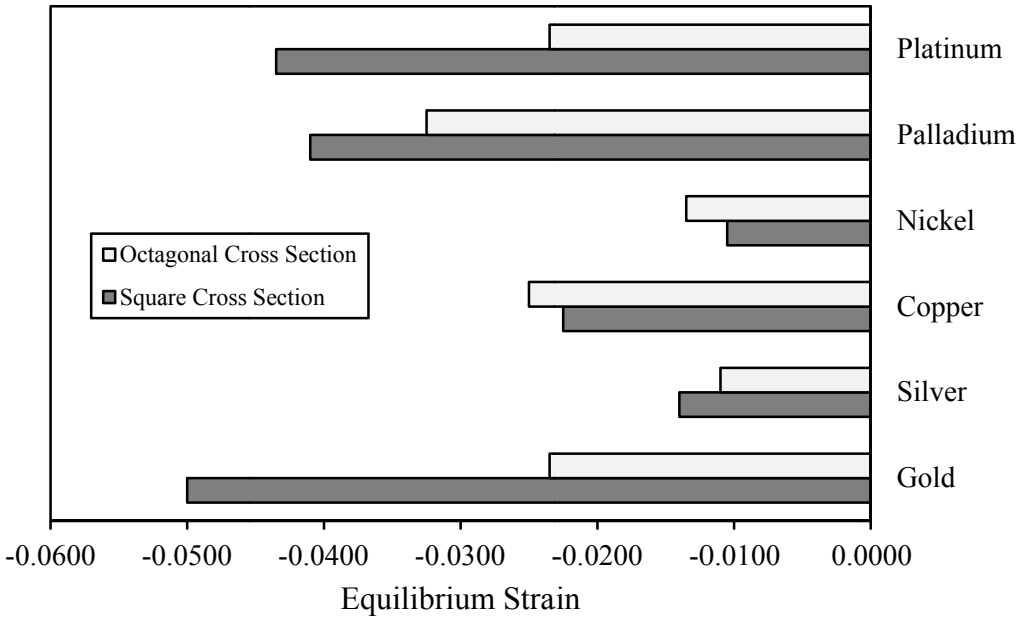

Figure 5.8 Comparison of the equilibrium strain of 2.5 nm square and octagonal cross section nanowires

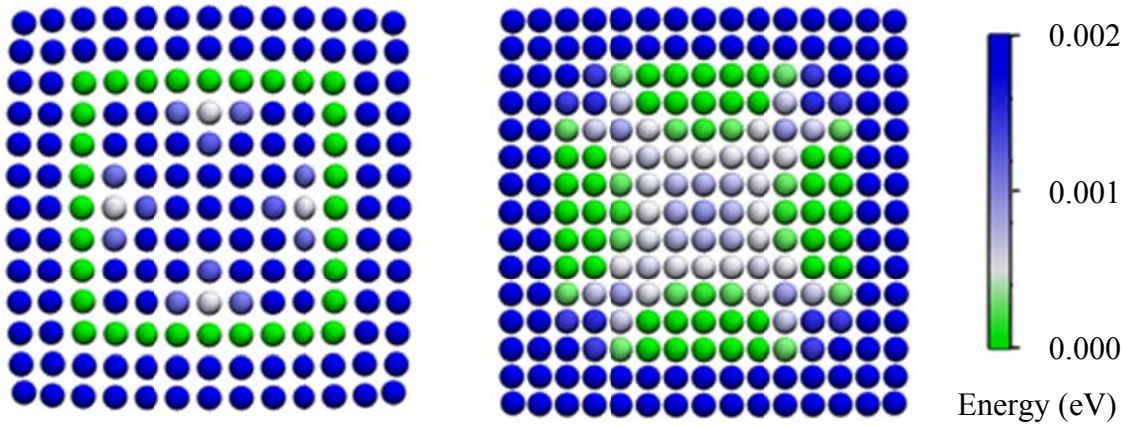

Figure 5.9 Comparison of gold (left) and nickel (right) 2.5 nm diameter square nanowires' energy at 0 strain

Both materials' corner atoms move toward the center to minimize energy. However, Figure 5.9 shows the gold corner atoms constricting much more than the nickel atoms. In addition, gold's surfaces become more rounded. The difference is due to the

anisotropicity of nickel between crystallographic directions. The anisotropy factor can be calculated from the elastic constants:

$$A = \frac{C_{11} - C_{12}}{2C_{44}} \qquad \text{Eq. 5.1}$$

The closer the anisotropy factor is to unity, the more anisotropic a single crystal of material is. Table 5.7 lists the anisotropy factor for all six metals. Calculated by the Foiles potential, the elastic constants used to calculate the anisotropy factor are found in Table 4.1. Note that gold has a lower anisotropy factor than nickel. This difference causes the gold nanowires to have higher internal strain energy over a larger area of the nanowire than nickel. This causes much higher internal strain energy in the core of the gold nanowires which contains few atoms at 0 energy. The gold nanowire has a much more defined core and surface in comparison to the nickel nanowire which is more heterogeneous. This discrepancy causes a difference in the interplay between the core atoms resisting contraction and the surface atoms driving contraction.

Table 5.7 Anisotropy factor for all materials

Material	Anisotropy Factor
Gold	0.267
Silver	0.333
Copper	0.278
Nickel	0.308
Palladium	0.260
Platinum	0.222

Figure 5.10 shows the per atom energy change from the initial structure to the equilibrium structure of 2.5 nm diameter nickel nanowires. Atoms colored in red increased in energy, atoms colored in white did not change energy, while green atoms decreased in energy.

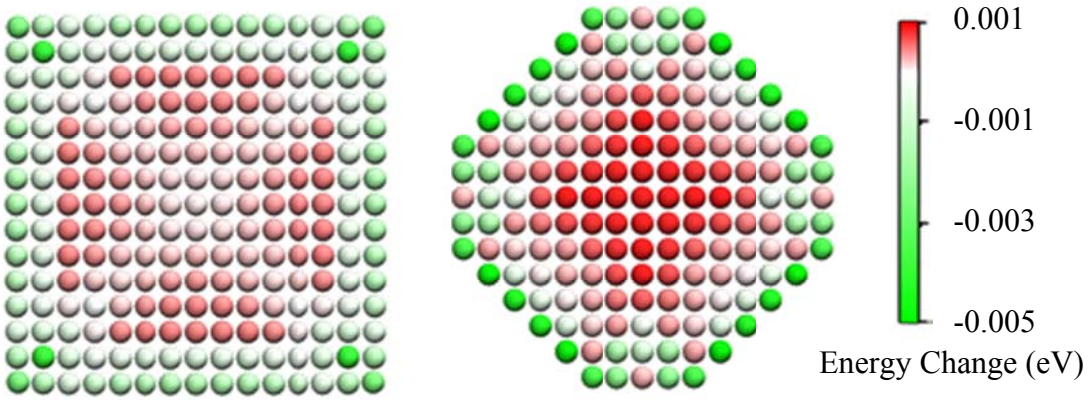

Figure 5.10 Per atom energy change from zero strain structure to equilibrium strain structure for nickel nanowires

The atoms forming the X pattern in the square nanowire did not increase as much in energy as the atoms colored in red near them. This indicates that at the equilibrium strain, the corner atoms did not constrict as much toward the center, counteracting the increase in strain energy from the $[\bar{1}00]$ contraction. The octagonal nanowire, however, had no initial strain energy which could be relieved. Therefore, all the central atoms increased in energy. The octagonal nickel nanowire behaves as expected, constricting more than the square nanowire.

Figure 5.11 shows the change in energy from zero strain to the equilibrium strain for two gold nanowires. The color scale is set such that the gray atoms did not change energy, red atoms increased in energy, and blue atoms decreased in energy. The square nanowire had a much lower equilibrium strain which caused the atoms to have a much larger magnitude of energy change. The atoms in the square cross section behave as expected, with a significant decrease in energy for the surface atoms and an increase in energy of the core atoms. The "X" pattern which was exhibited in the nickel nanowire is noticeably diminished. The octagonal cross section is very different from the nickel nanowire. To compare nickel and gold directly, Figure 5.12 shows both colored according to the same scale. The {011} surface decreases in energy more than the {010}

or {001} surfaces in the nickel nanowire indicating that the higher energy {011} surfaces were the driving force in nickel's contraction. In contrast, the {010} and {001} surfaces in the gold nanowire decrease in energy more than the {011} surfaces. Therefore, the addition of {011} surfaces for gold nanowires results in less contraction.

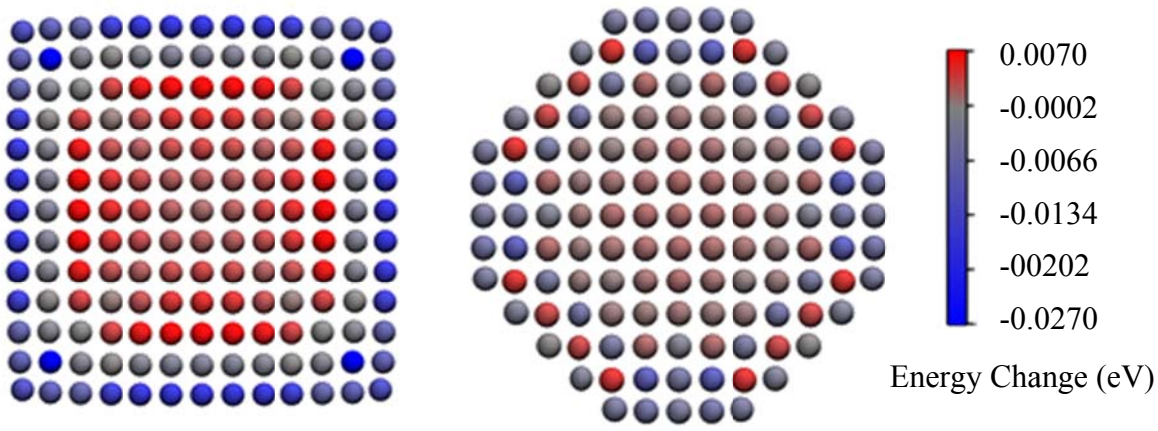

Figure 5.11 Per atom energy change from zero strain structure to equilibrium strain structure for gold nanowires

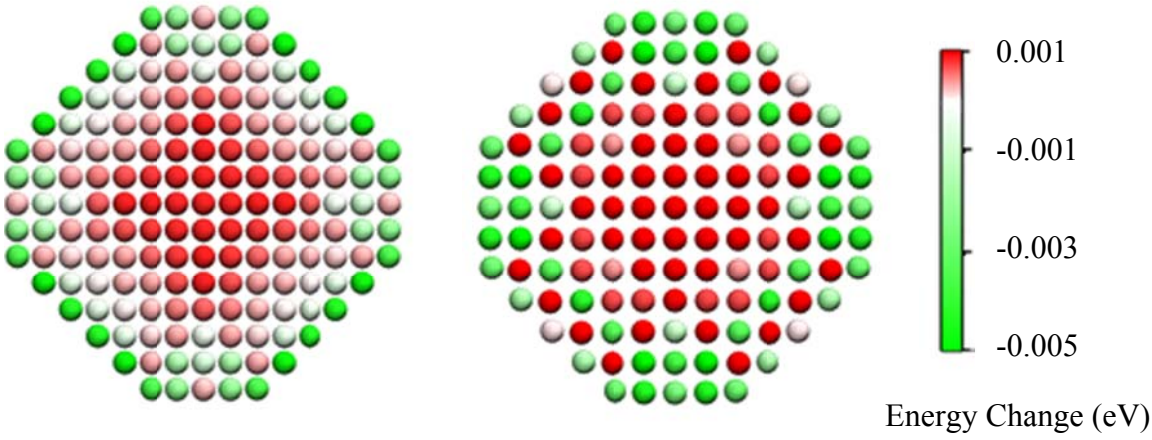

Figure 5.12 Per atom energy change from zero strain structure to equilibrium strain structure for nickel (left) and gold (right) octagonal cross sections

The cause for the decrease in contraction may be that the energy difference of the two crystal surfaces is less in gold than nickel. Figure 5.13 shows that nickel's {011} surfaces are significantly higher in energy than the {010} or {001} surfaces. The surfaces on the gold nanowire are energetically similar.

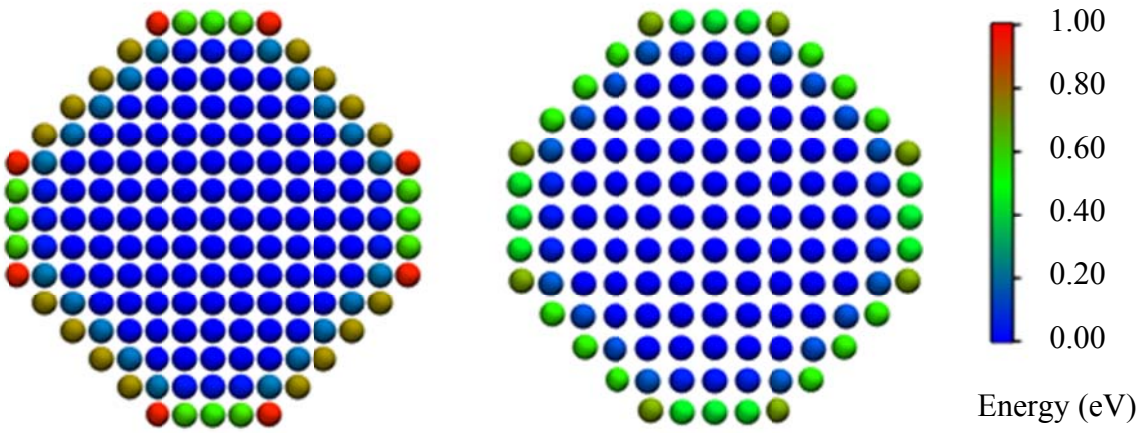

Figure 5.13 Energy of nickel (left) and gold (right) octagonal nanowires at zero strain

Reference [12] also found that in nanowires with a diameter below 1 nm, a shift in structure occurs which causes drastically different mechanical behavior. The entire minimization curve for a 1 nm nanowire can be seen in Figure 5.14.

In the larger nanowires, an energy minimum occurred between a strain of -0.10 and 0. In the case of the 1 nm nanowire, the energy curve flattens, but no local minimum is exhibited in this area. Such large compressive strains cause the nanowire to assume a different structure. This nanowire at zero strain and equilibrium strain is shown in Figure 5.15, where the structure change can be seen. With such large compressive strain, the atoms begin to move into a different configuration showing significant vertical expansion. In Figure 5.16, cross sections of the nanowires from Figure 5.15 are shown.

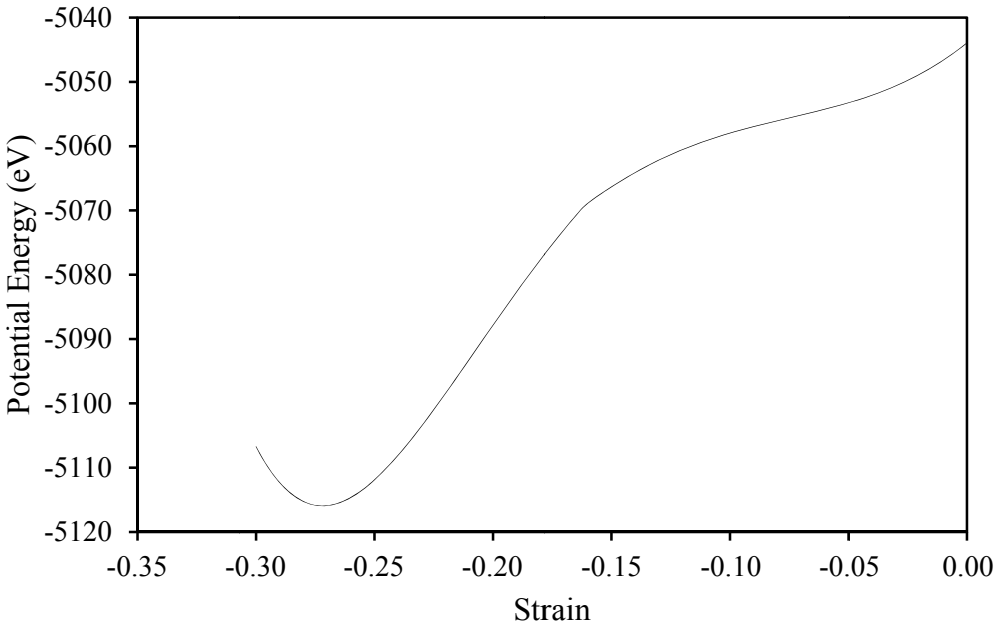

Figure 5.14 Minimization curve of a 1 nm diameter circular copper nanowire

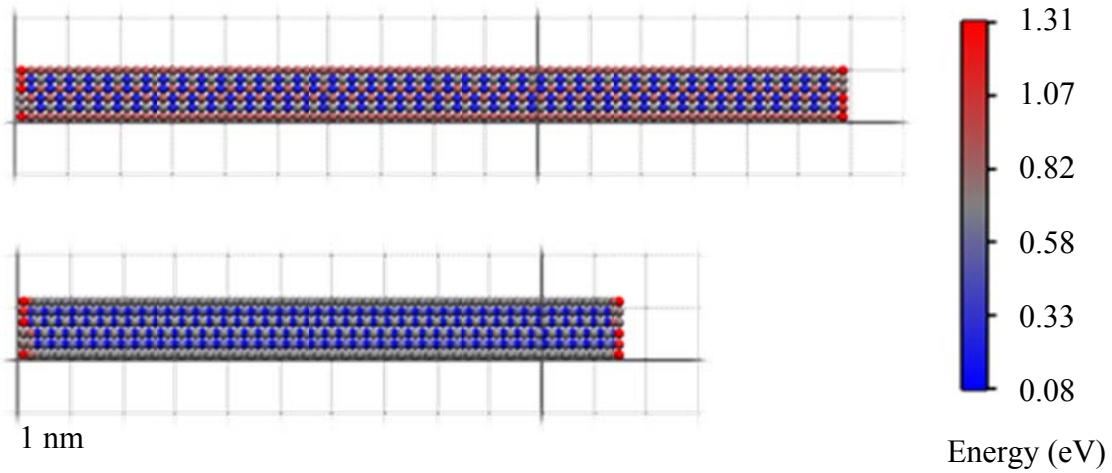

Figure 5.15 1 nm diameter circular copper nanowire before minimization at ε = 0 (top) and after minimization at ε = -0.276 (bottom)

At zero strain, the surface atoms are at a very high energy state due to having fewer adjacent atoms than the core atoms. This causes the nanowire to contract along the

length of the nanowire to minimize energy. Since the contraction is so great, the atoms spread out in the y and z directions to minimize the energy of the core atoms.

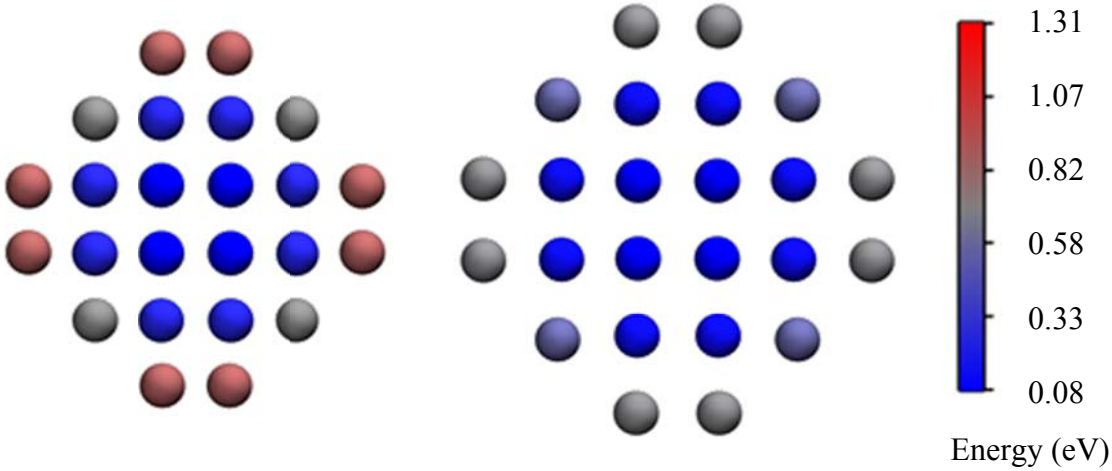

Figure 5.16 1 nm diameter copper nanowire cross section before minimization at ε = 0 (left) and after minimization at ε = -0.276 (right)

However, the structures created with such large compressive strains became unstable. During the minimization process, some structures would begin to exhibit severe plastic deformations. The problems during minimization make the physicality of the structures questionable.

Larger diameter nanowires also exhibit a structure change if minimization is carried out all the way to a strain of -0.3. This structure change may have been missed in previous studies because a local minimum is exhibited before the second minimum. A full minimization curve of a larger diameter nanowire can be seen in Figure 5.17.

When approaching the lower minimum, the majority of these structures were not well behaved further indicating that these structures may not be physical. At times, the minimization was achieved by sliding entire sheets of atoms in the structure. Figure 5.18 exemplifies this shift. Both snapshots show the cross section of a 5 nm diameter circular

copper nanowire. The strain level for this nanowire is the second minimum of Figure 5.17, ε = -0.288. The structure before minimization is shown in Figure 5.18 (a) while Figure 5.18 (b) shows the structure after minimization. One section of atoms is colored in red to show how the program changes the structure during energy minimization. To minimize energy, entire rows and columns of atoms are shifted throughout the structure. This type of change is a plastic deformation, and results in an unreasonable structure for the nanowires. Another indication of the non-physical nature of the structure change is immediate yielding when these structures are used in a molecular dynamics simulation.

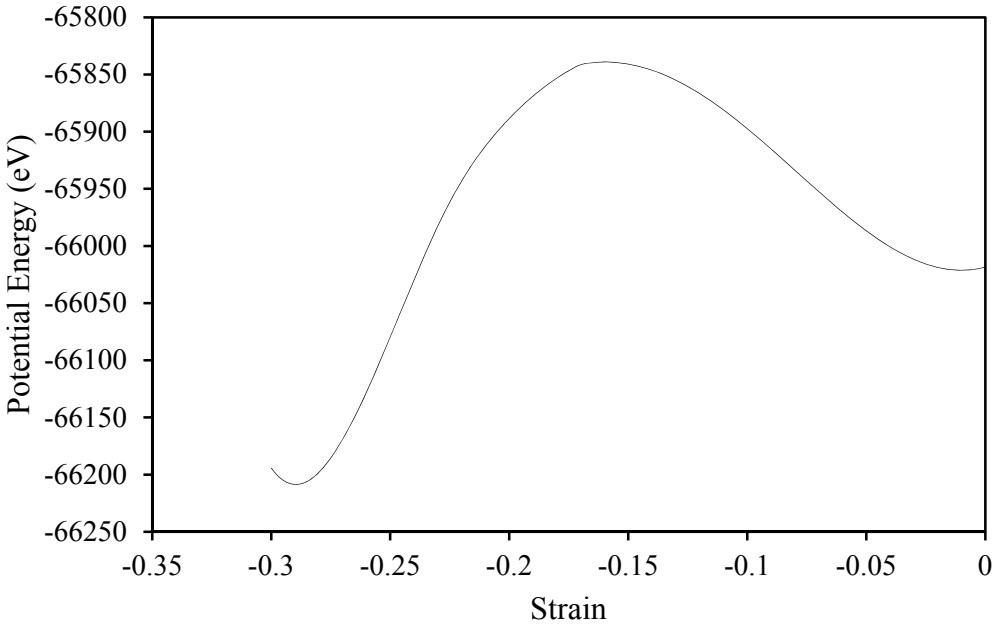

Figure 5.17 Full minimization curve of a 5 nm diameter circular gold nanowire showing two minimums

5.1.1 Remarks about Platinum

The minimum diameter of platinum nanowire that could be created was 4 nm. Structures below 4 nm posed minimization problems. The minimization problems were similar to the problems which can be seen in Figure 5.14. There was no minimum near a strain of ε = -0.100, only a minimum near ε = -0.300 was present. However, during the minimization process, the energy of these structures was minimized by sliding sheets of

atoms on top of each other. The structure change during the minimization resembled that which can be seen in Figure 5.18.

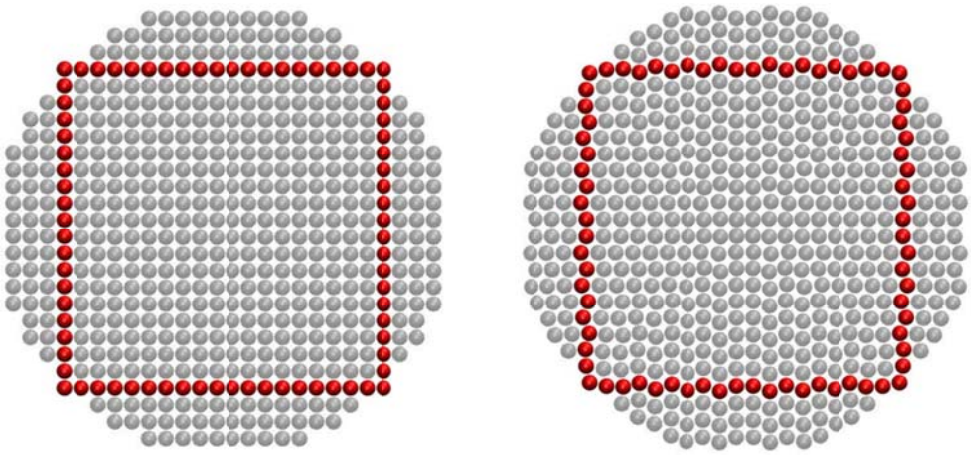

(a) (b)

Figure 5.18 Cross section of a 5 nm diameter silver circular nanowire at $\varepsilon = -0.288$ (a) before minimization (b) after minimization

5.2 Stress-Strain Diagrams

The majority of the numerical data collected was read directly from stress-strain curves. The curves were created from data outputted from LAMMPS every 1000 timesteps which corresponds to one data point every 1 ps. Since in each case the strain rate was set to 10^8 s^{-1}, every picosecond the strain increased by 10^{-4}. LAMMPS does not output a stress quantity, so stress was obtained by outputting the instantaneous pressure and multiplying by the equilibrium volume of the system. Only P_{xx} was used to find the normal stress along the length of the nanowire.

In Figure 5.19, one example of a stress-strain diagram can be seen. The stress-strain diagrams resulting from nanomaterials differ from those of bulk materials. Bulk scale materials generally have a continuous smooth line until failure. Nanomaterials differ by exhibiting almost instantaneous changes in stress levels resulting from localized yield events. These abrupt changes correspond to a dissipation of internal strain through defect nucleation and movement which results in slip.

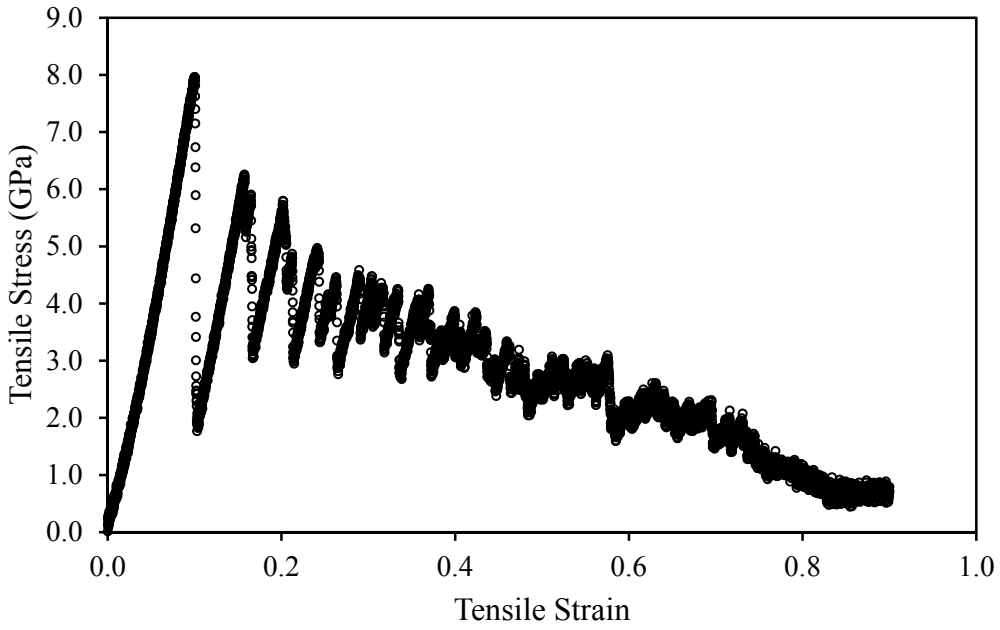

Figure 5.19 Stress-strain diagram for a 5 nm diameter circular copper nanowire

5.2.1 Yield Strain

The yield strain is easily identified from stress-strain diagrams such as the one depicted in Figure 5.19. The yield strain exists at the first point when the tensile stress instantaneously drops. In all cases, this point corresponded to the ultimate stress, or the largest stress exhibited on the stress-strain diagram. In Figure 5.20, Figure 5.21, and Figure 5.22, the yield strain as a function of diameter is graphed for all three cross-sectional shapes.

For all structures except octagonal and circular silver, it was found that the yield strain increased with decreasing cross-sectional area. Since the smaller diameter nanowires contract more than their larger counterparts, they contain more internal strain energy. The increase in yield strain may correspond to the dissipation of the excess strain energy in the smaller diameter nanowires.

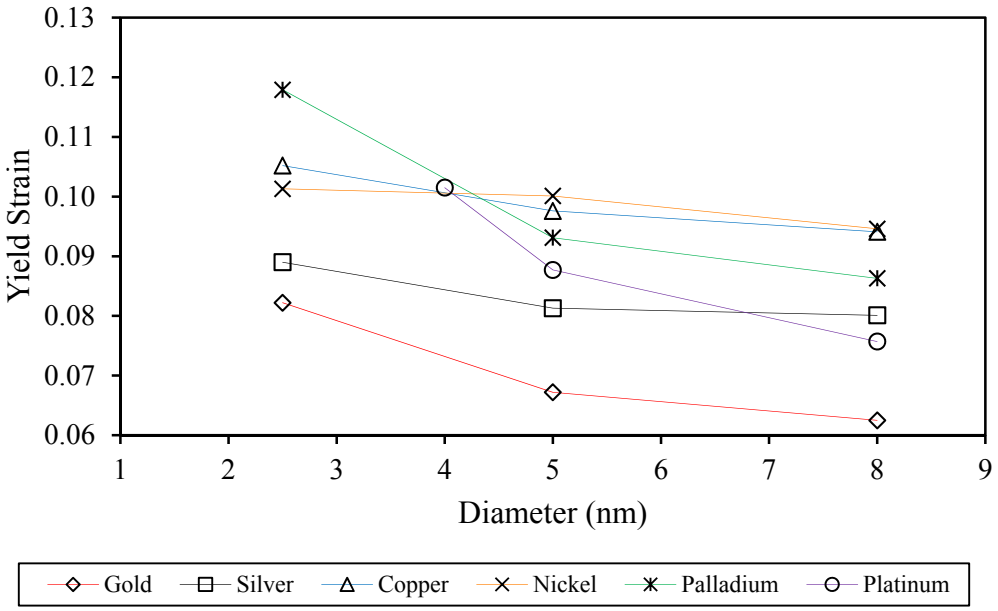

Figure 5.20 Yield strain for square cross section nanowires

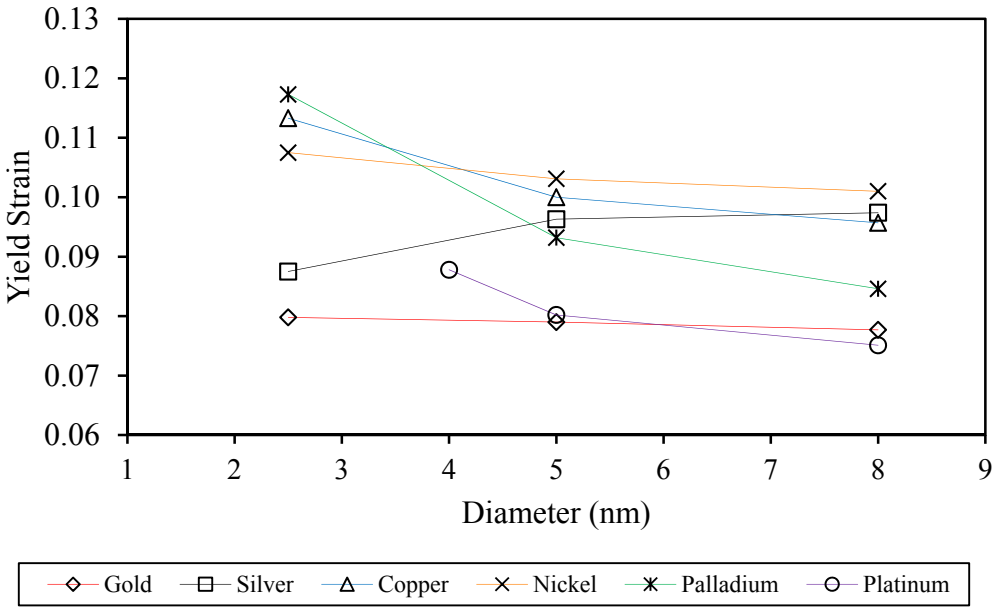

Figure 5.21 Yield strain for circular cross section nanowires

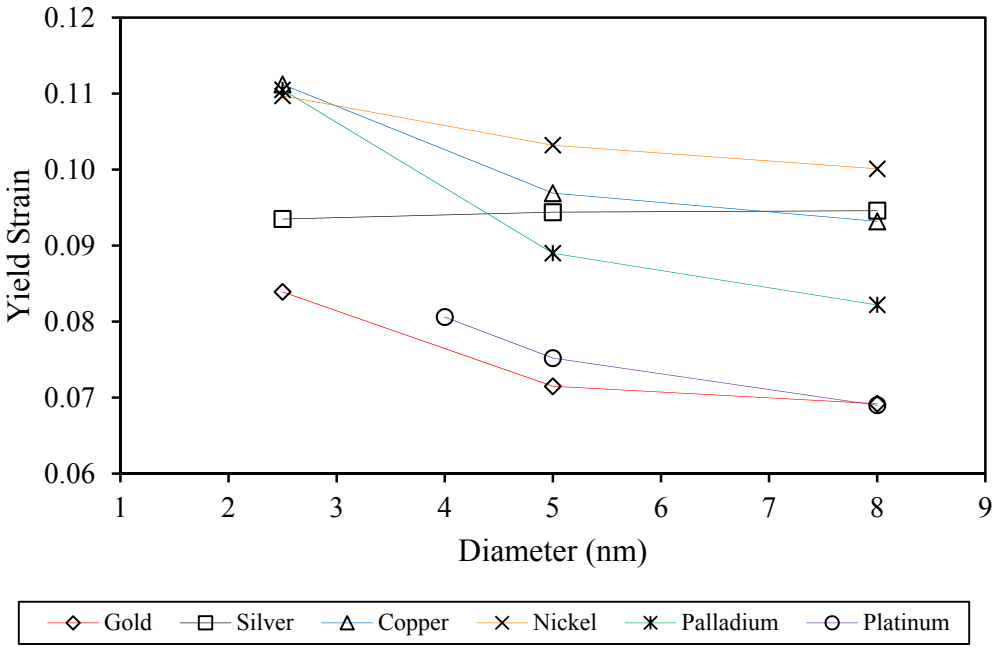

Figure 5.22 Yield strain for octagonal cross section nanowires

5.2.2 Yield Stress

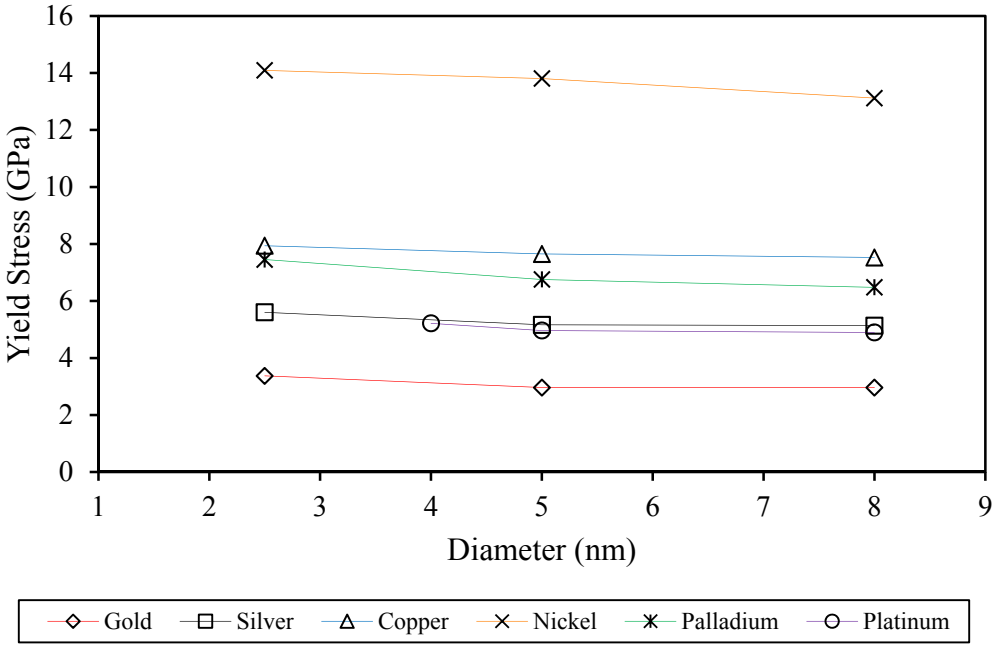

Figure 5.23 Yield stress for square cross section nanowires

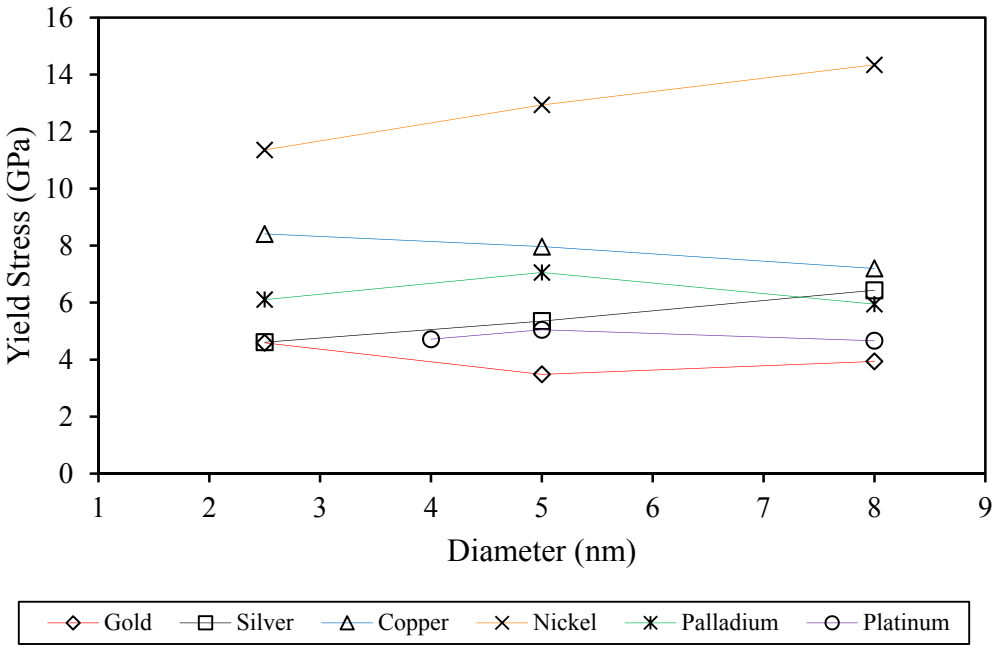

Figure 5.24 Yield stress for circular cross section nanowires

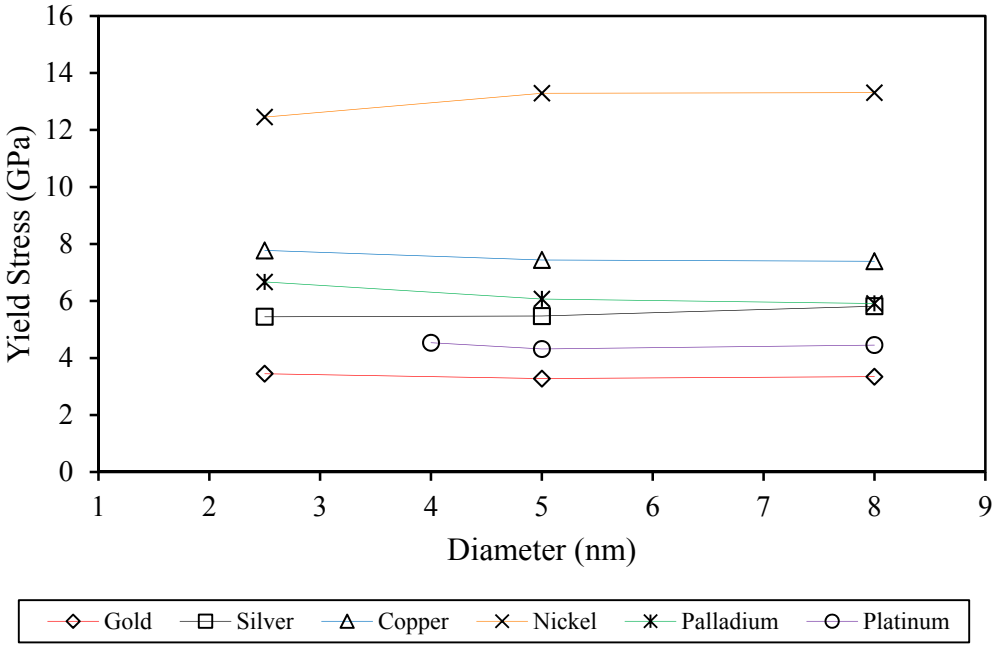

Figure 5.25 Yield stress for octagonal cross section nanowires

Figure 5.23, Figure 5.24, and Figure 5.25 show the yield stress for each nanowire configuration. The yield stress remained relatively constant over the range of diameters. The circular nanowires showed the largest variations in yield stress. This can be attributed to the lack of consistent surfaces on circular nanowires. Both square and octagonal nanowires have surfaces along a defined crystallographic direction. Circular nanowires, however, do not have well-defined surfaces.

5.2.3 Ultimate Strain

Figure 5.26, Figure 5.27, and Figure 5.28 show the ultimate strain for each nanowire. For most nanowires, the ultimate strain increased as the diameter increased. This is due to the fact that most fracture occurred by slip leading to necking which eventually caused failure. The larger diameter nanowires took longer to neck to a diameter where fracture would occur.

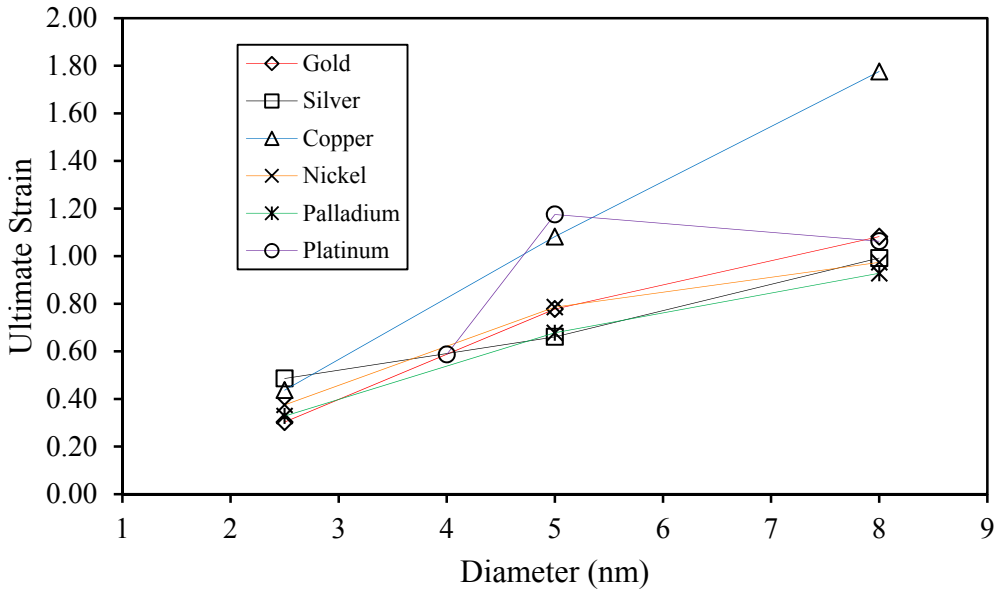

Figure 5.26 Ultimate strain for square cross section nanowires

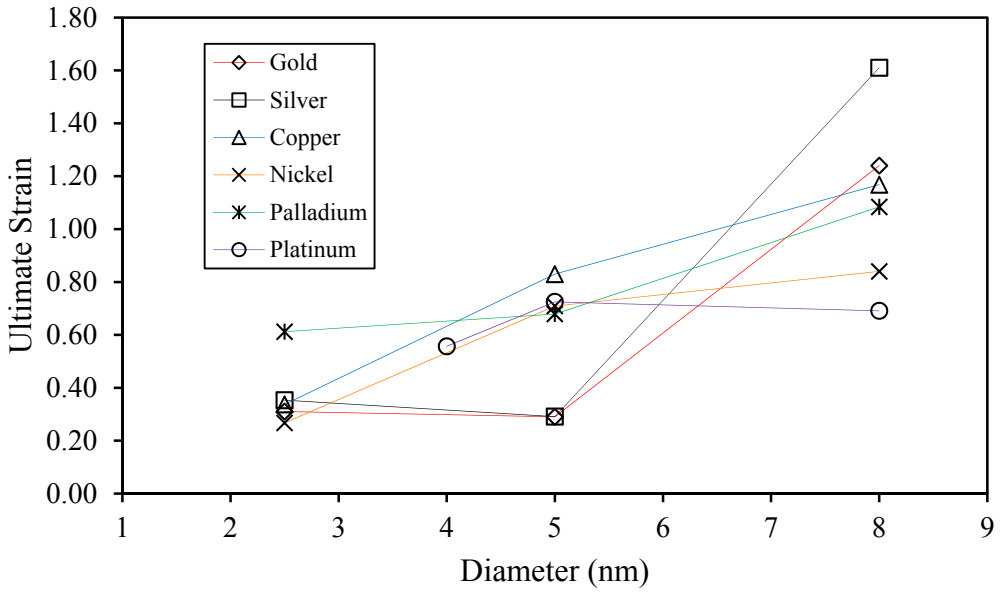

Figure 5.27 Ultimate strain for circular cross section nanowires

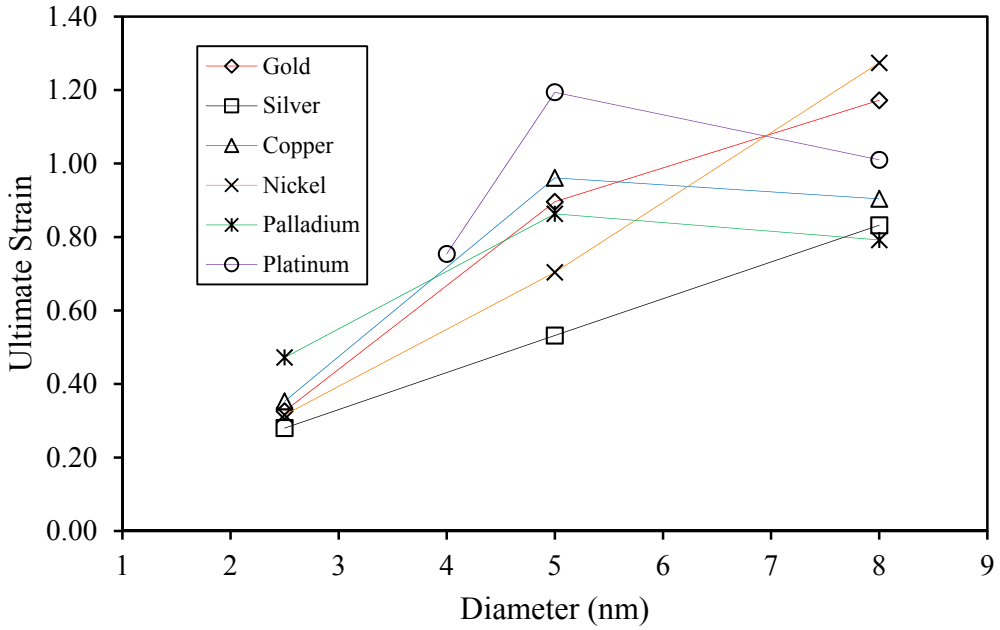

Figure 5.28 Ultimate strain for octagonal cross section nanowires

An important thing to note from these figures is the jump in ultimate strain for the 5 nm platinum nanowire. These nanowire exhibited different deformation mechanisms which allowed for greater tensile elongation. The octagonal nanowire deformed almost exclusively through surface reconstruction rather than slip. This deformation mechanism is discussed further in Section 5.5.3. The square and circular platinum nanowires with a diameter of 5 nm exhibited a mix of surface reconstruction and slip. At a diameter of 5 nm, the surface energy of platinum nanowires may make it likely that surface reconstruction occurs. The surface reconstruction causes the nanowires to have a larger ultimate strain.

5.2.4 Graphical Method Young's Modulus

Two methods were used to determine Young's modulus for the nanowires: (1) a graphical method and (2) an energy method. The graphical method obtained Young's modulus by assuming linear elastic behavior prior to yielding similar to bulk metallic systems:

$$\sigma_{xx} = E\varepsilon \qquad \text{Eq. 5.2}$$

Young's modulus was then found by applying a linear fit to the stress-strain response and recording the slope of the fitted line. Only the response prior to 1% elongation was considered to ensure elastic behavior. The data points used were the same as those in Figure 5.19. The points are instantaneous values taken every 1 ps. As such, thermal noise causes deviations from perfectly elastic behavior. Figure 5.29 shows an example of one of these graphs.

This procedure was completed for all 54 configurations of materials, sizes, and shapes. In Figure 5.30, Figure 5.31, and Figure 5.32, these results are shown.

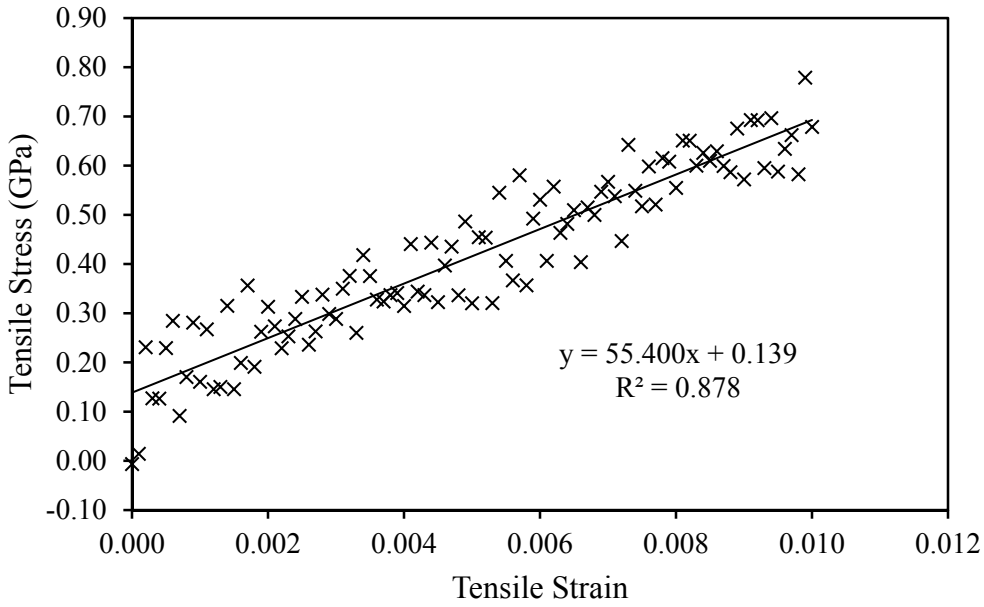

Figure 5.29 Example of graphical determination of Young's modulus using stress-strain diagrams for a 5 nm diameter circular copper nanowire

Young's modulus increased with increasing diameter in all but one case. Young's modulus was calculated assuming linear elastic mechanical behavior before yield:

$$E = \frac{\sigma}{\varepsilon} \qquad \text{Eq. 5.3}$$

Previously, it was found that with increasing diameter the yield strain decreased while the yield stress stayed constant. The finding that Young's modulus increased with increasing diameter is consistent with these findings and Eq. 5.3.

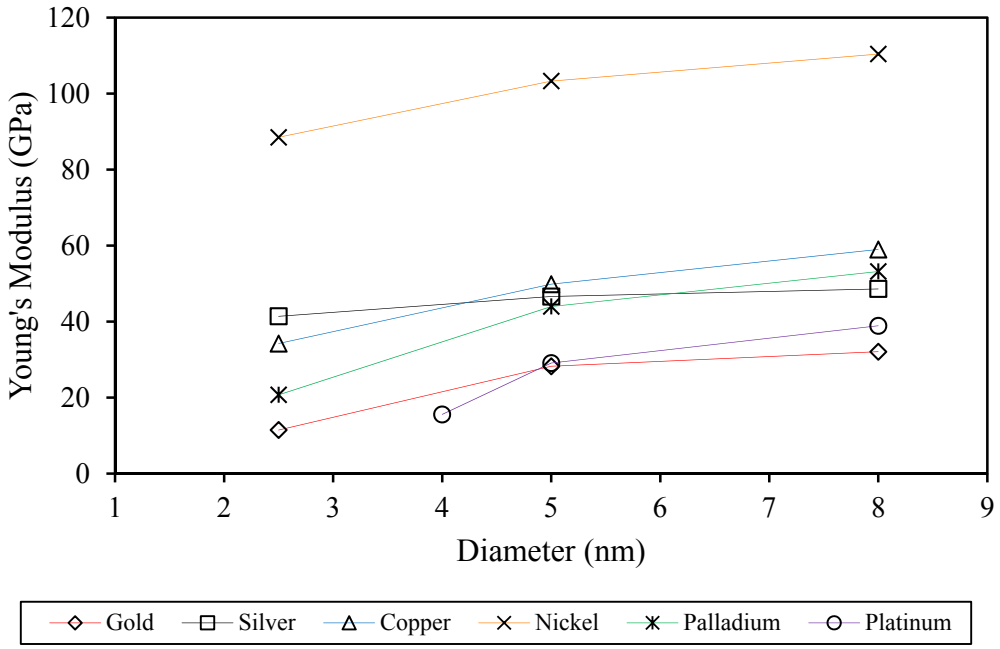

Figure 5.30 Young's modulus as a function of diameter for nanowires with square cross sections as determined by the graphical method

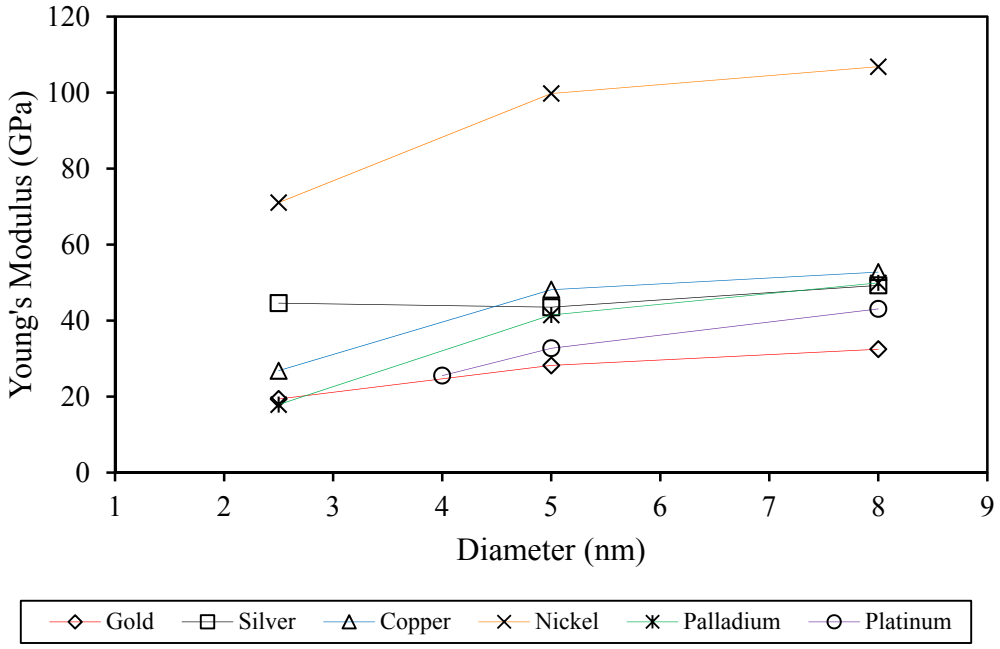

Figure 5.31 Young's modulus as a function of diameter for nanowires with circular cross sections as determined by the graphical method

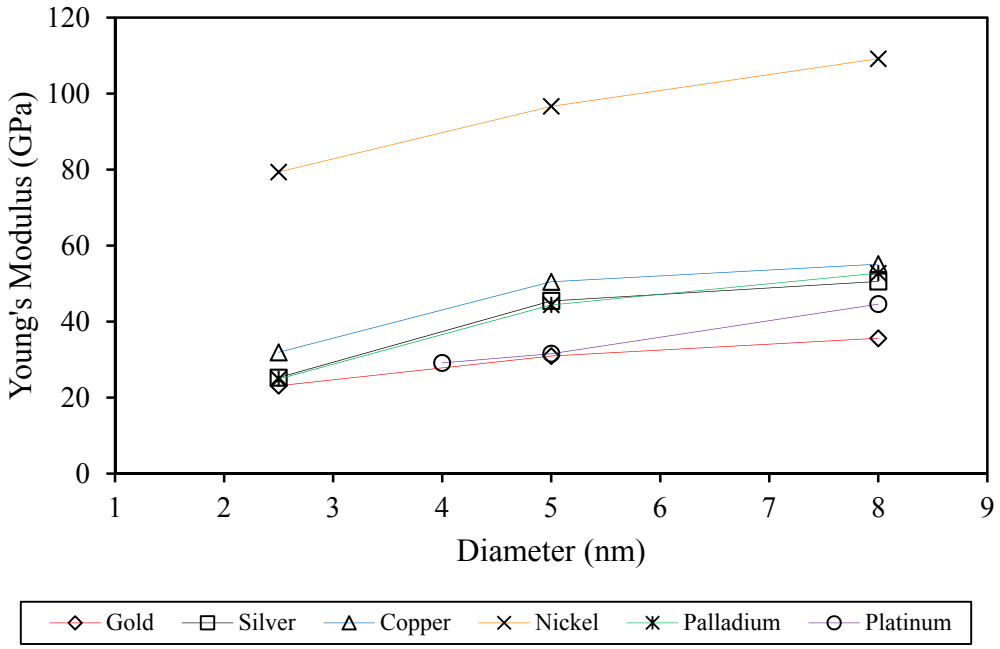

Figure 5.32 Young's modulus as a function of diameter for nanowires with octagonal cross sections as determined by the graphical method

5.3 Energy Method Young's Modulus

The second method used to calculate Young's modulus for the nanowires is the energy method as described in Section 4.5 on page 25. After minimization, the equilibrium structure was stretched to a strain of 0.010 in increments of 0.002. At each strain increment, the structure was minimized, and the total energy was recorded. By Eq. 4.5, a second order fit of $\Delta U / V_o$ as a function of strain can be used to calculate Young's modulus.

In Figure 5.33, one such graph is shown. The coefficient of 2.462 x 10^{10} indicates that the experimental modulus for this wire is 49.24 GPa. The results for all nanowire configurations can be found in Figure 5.34, Figure 5.35, and Figure 5.36.

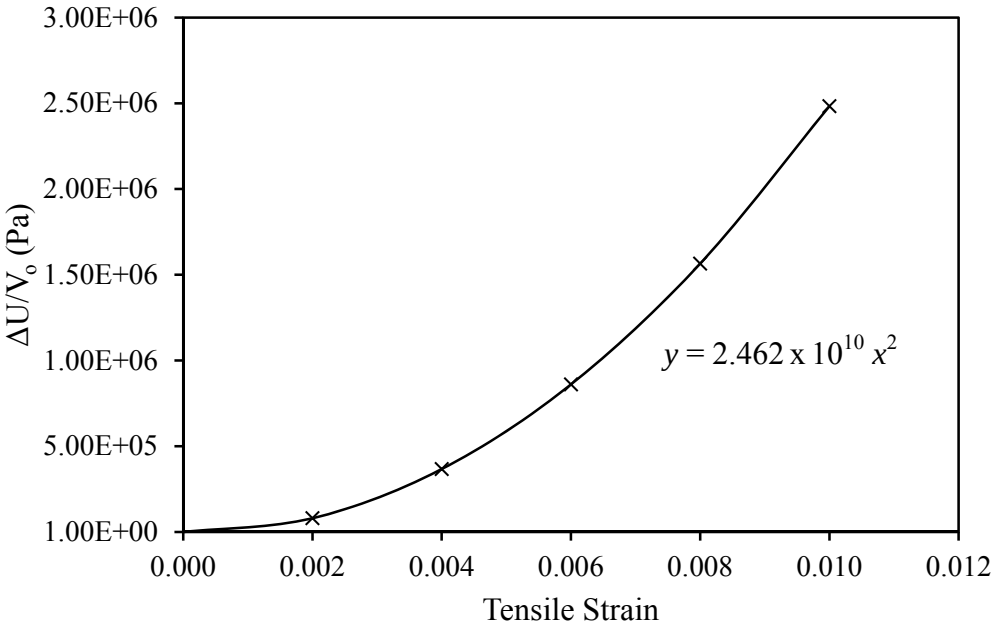

Figure 5.33 Example of determination of Young's modulus using the energy method for a 5 nm diameter circular copper nanowire

Figure 5.34, Figure 5.35, and Figure 5.36 show that, for most nanowires, Young's modulus decreases with decreasing diameter. These results qualitatively compare well with the results from the graphical method. Exact quantity correlation cannot be expected as the energy method applies static loading while the graphical method is dynamic and carried out at a temperature of 300 K. In addition, both measurements depend on choice of atomic volume. This provides validation that the molecular dynamics approach yields expected results.

The energy method allowed for investigation of the modulus of nanowires with diameter of 1 nm. These nanowires show a significantly different trend due to the structural changes that occur. This trend can be seen in Figure 5.37.

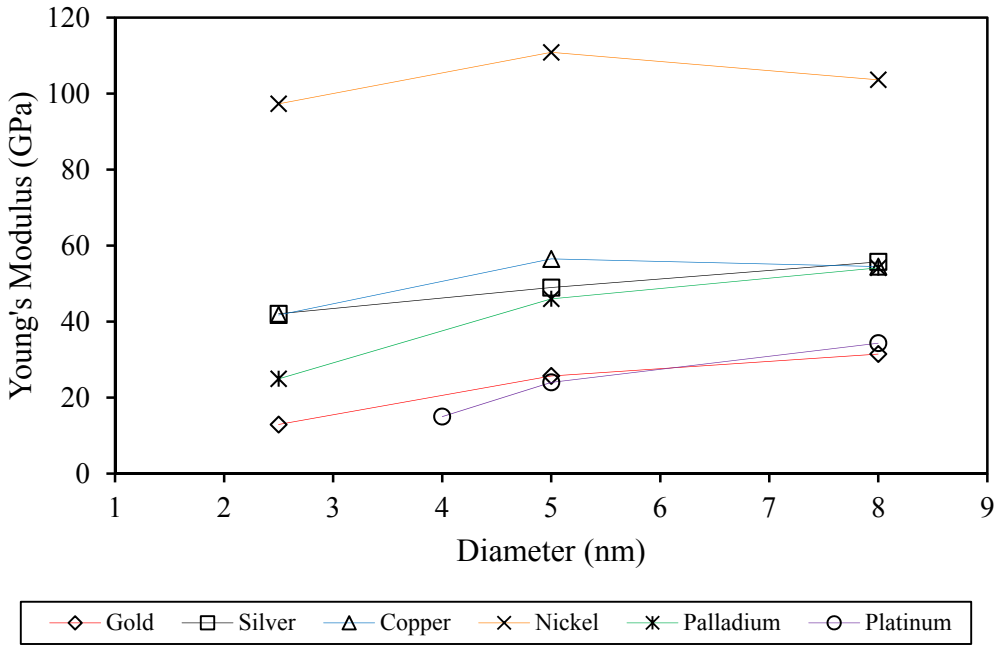

Figure 5.34 Young's modulus as a function of diameter for nanowires with square cross sections as determined by the energy method

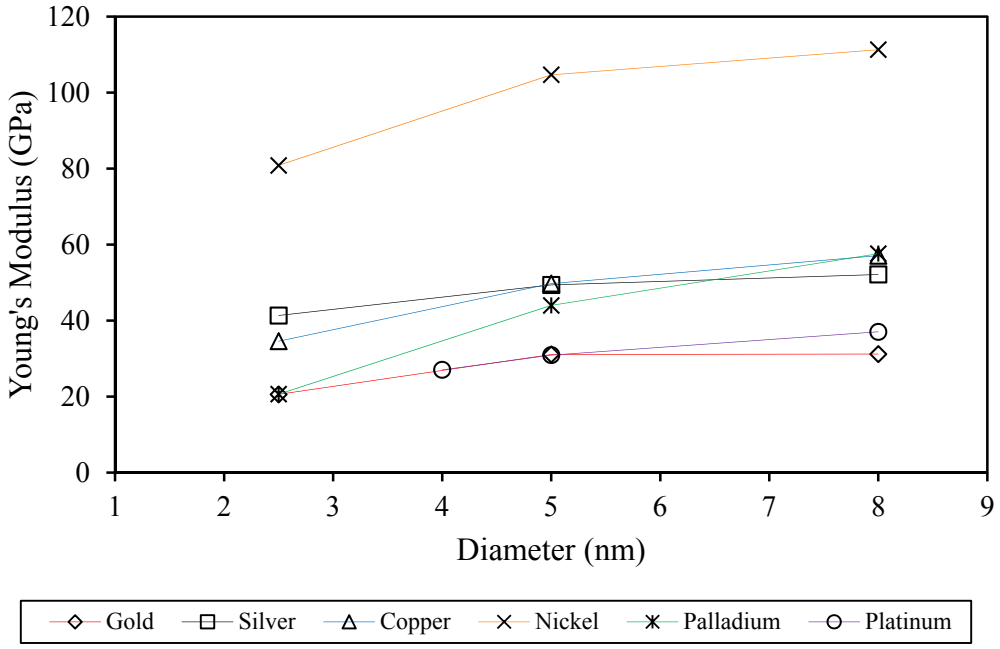

Figure 5.35 Young's modulus as a function of diameter for nanowires with circular cross sections as determined by the energy method

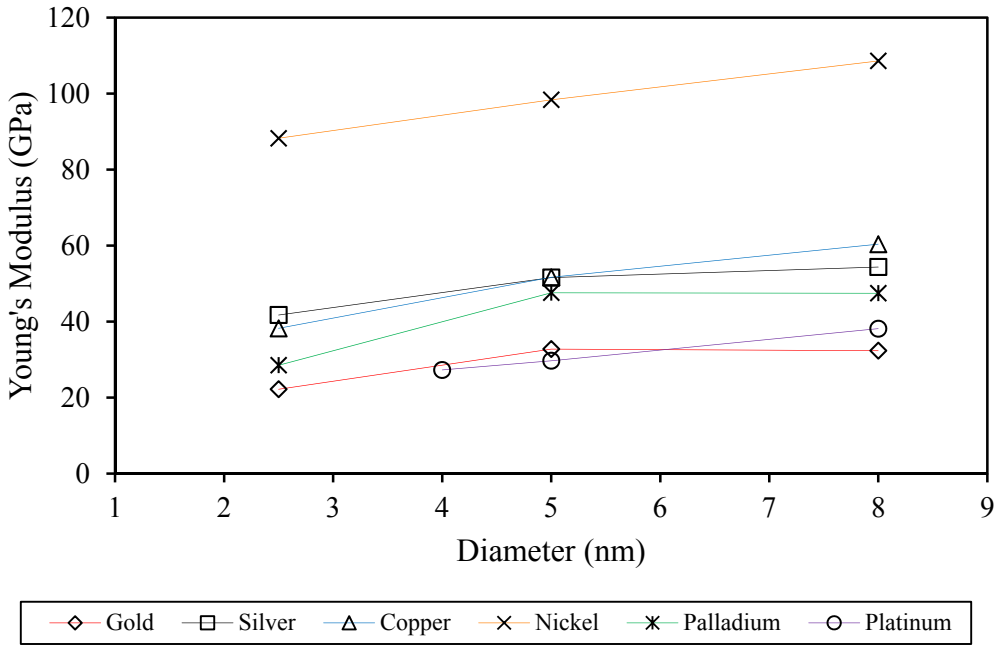

Figure 5.36 Young's modulus as a function of diameter for nanowires with octagonal cross sections as determined by the energy method

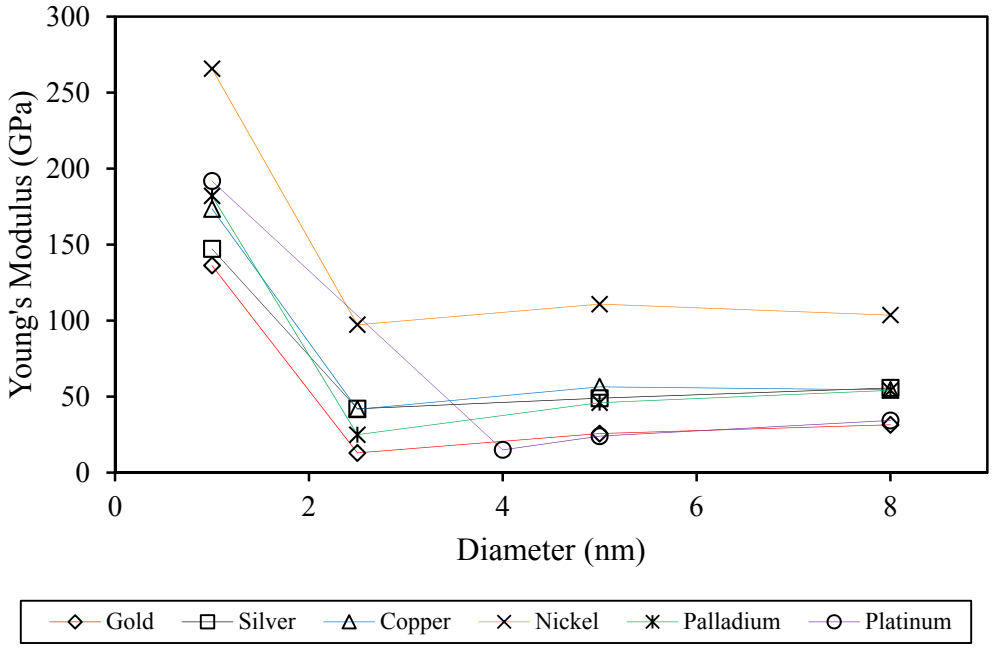

Figure 5.37 Young's modulus as a function of diameter for square nanowires including 1 nm diameter

Figure 5.37 shows an example of Young's modulus as a function of diameter for square cross section nanowires including the 1 nm diameter nanowires. The graphs of the other cross-sectional shapes can be found in the appendix on page 93. The extraordinary increase for the Young's modulus of the smallest nanowire is similar to that found in reference [12]. In addition, the order of magnitude decrease in equilibrium strain of the smaller nanowires also mimics that discussed in [12].

The increase in Young's modulus is also expected considering Figure 5.14. The energy method uses functional fitting to obtain the experimental value for Young's modulus. The slope of the graph in Figure 5.14 is proportional to the calculated Young's modulus. Near the equilibrium strain, the slope increases significantly.

5.4 Finding Young's Modulus through Inversion of the Stiffness Matrix

The last way to verify the molecular dynamics approach is to compare the calculated Young's modulus results to the results obtained by inverting the stiffness matrices for each material. This is the method described in Section 4.6. Table 5.8 lists the values obtained for Young's modulus using this method. Figure 5.38, Figure 5.39, Figure 5.40, Figure 5.41, Figure 5.42, and Figure 5.43 show the Young's modulus dependence for each material. The graphs all include a dashed line which indicates the modulus value calculated by inversion of the stiffness matrix.

Table 5.8 Young's modulus calculated by inverting the stiffness matrix

Material	Young's Modulus (GPa)
Gold	35.158
Silver	53.718
Copper	62.685
Nickel	114.434
Palladium	55.213
Platinum	47.111

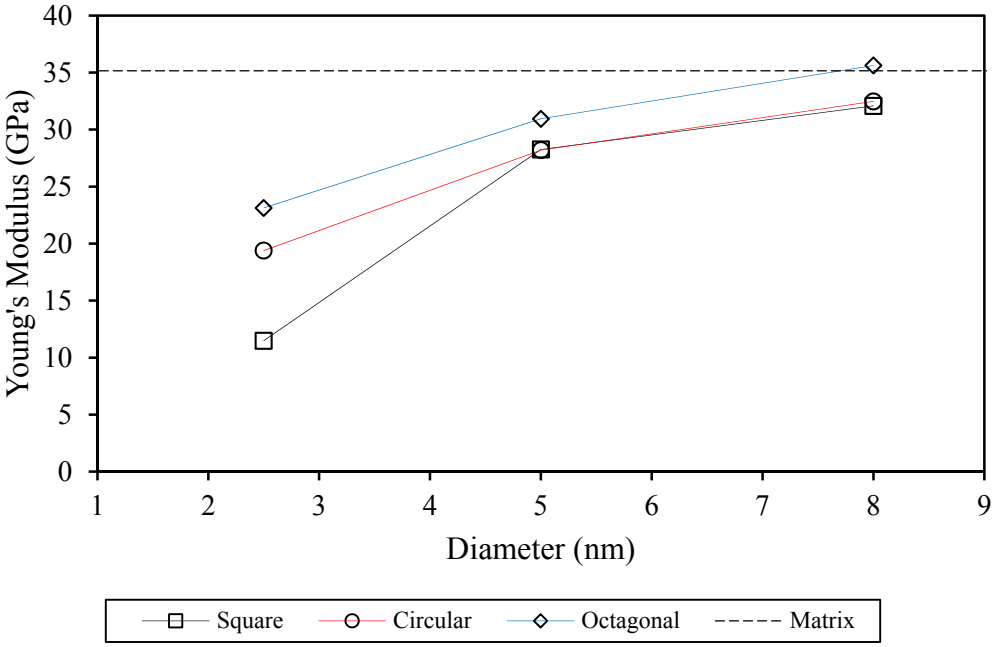

Figure 5.38 Young's modulus as a function of diameter for gold nanowires

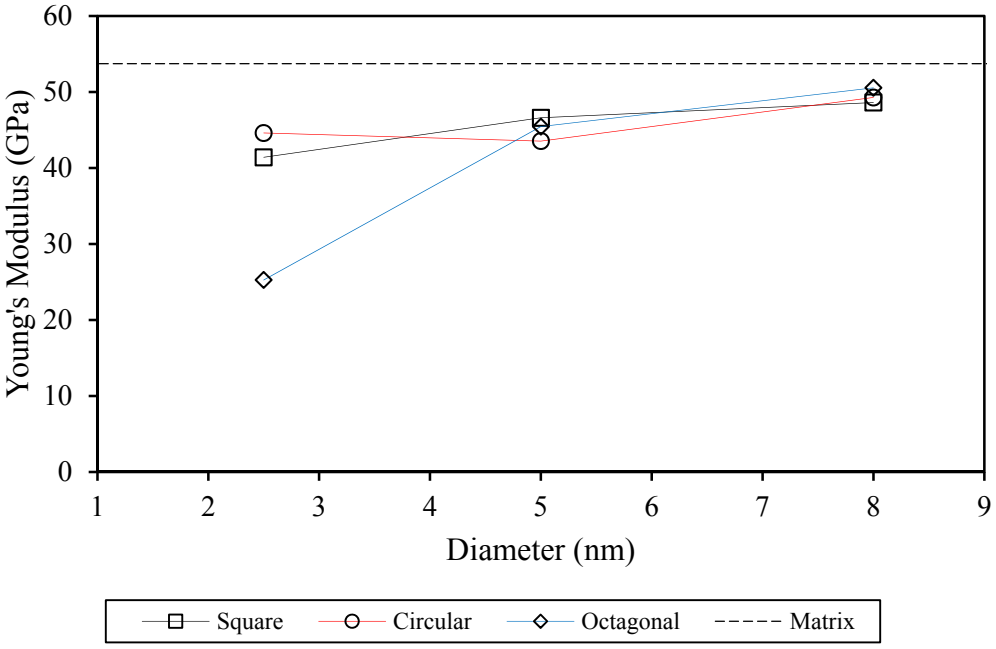

Figure 5.39 Young's modulus as a function of diameter for silver nanowires

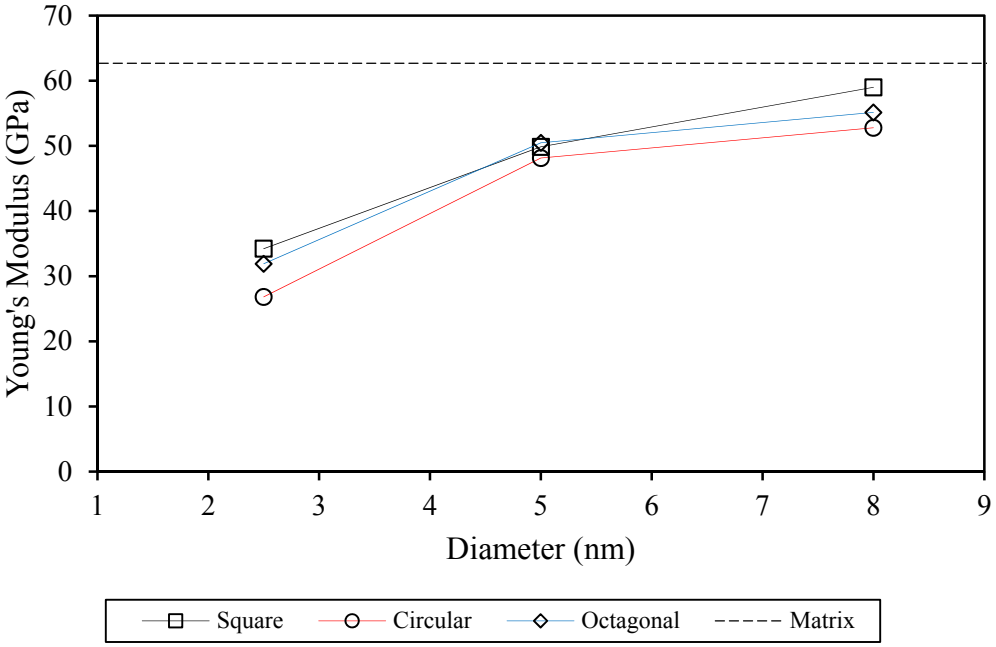

Figure 5.40 Young's modulus as a function of diameter for copper nanowires

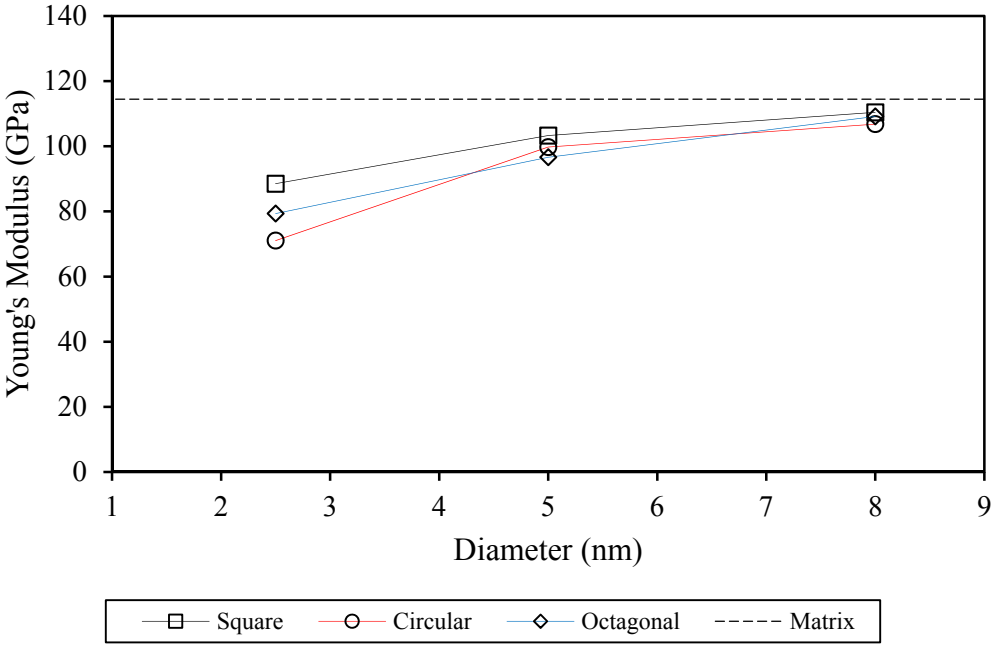

Figure 5.41 Young's modulus as a function of diameter for nickel nanowires

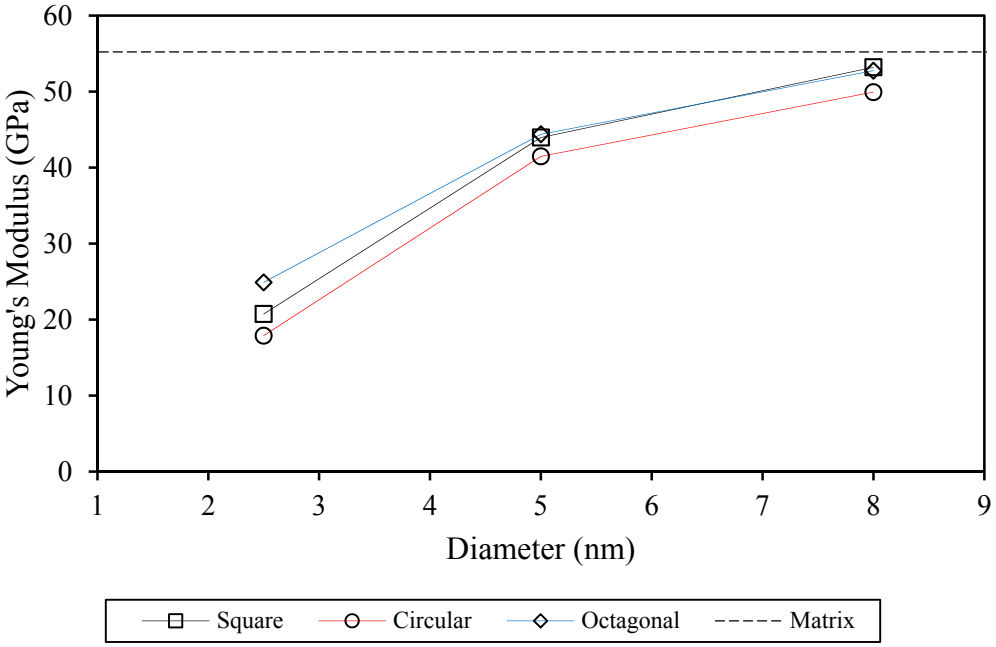

Figure 5.42 Young's modulus as a function of diameter for palladium nanowires

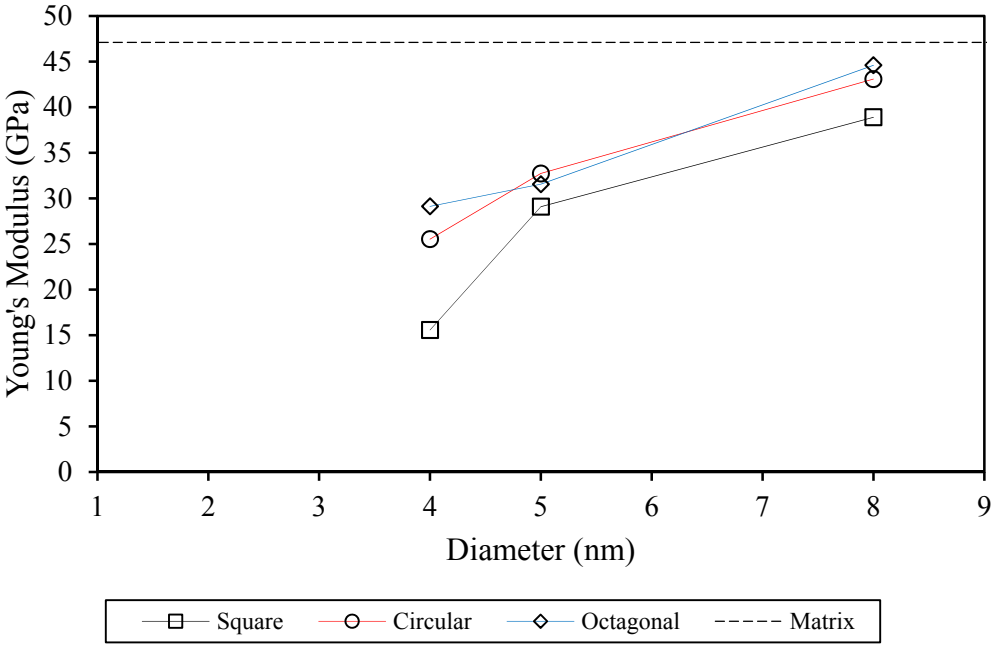

Figure 5.43 Young's modulus as a function of diameter for platinum nanowires

The figures show as the nanowire diameter increases, the values for Young's modulus seem to be approaching the value predicted by inversion of the stiffness matrices. This is because the larger nanowires have less surface area to volume ratio causing them to act more like the bulk material. These findings confirm that the molecular dynamics approach used in this thesis provides reasonable results.

5.5 Deformation Behavior

The deformation behavior of the nanowires depends on the cross-sectional shape. Each cross-sectional shape has different surface types. The square cross section nanowire has {010} and {001} surfaces only. The octagonal nanowire has higher energy {011} surfaces in addition to the {010} and {001} surfaces.

Yielding generally occurs when high energy atoms appear near one of the surfaces causing a partial dislocation. The partial dislocation usually occurs at the edge of two intersecting surfaces as these are the atoms in the highest energy state. The partial dislocation then propagates by the movement of atoms over the surface of the nanowire. The nanowires then fail through {111} slip.

5.5.1 Yield Initiation and Propagation

Figure 5.44 shows the initiation and propagation of a defect on the surface of a 5 nm diameter octagonal palladium nanowire. Only atoms with energy between 0.41 eV and 1.21 eV are shown to highlight the defect. The yielding begins with a large concentration of high energy atoms developing beneath a {011} surface. These high energy atoms push two columns of atoms downward. Once enough space is created, a high energy atom from an adjacent layer moves toward the surface creating an interstitial defect. This atom then displaces the original atoms initiating deformation twinning across the defect.

Figure 5.44 (d) shows the initiation of a twinned structure on the surfaces adjacent to the initial fault. Figure 5.45 shows the propagation across the (011) surface 90° around the x axis from the initial interstitial defect. The propagation speed is very similar on each side of the initial defect. After propagation {111} slip planes are initiated throughout the structure. Figure 5.46 shows another example of the propagation and the beginning of slip in an octagonal nickel nanowire.

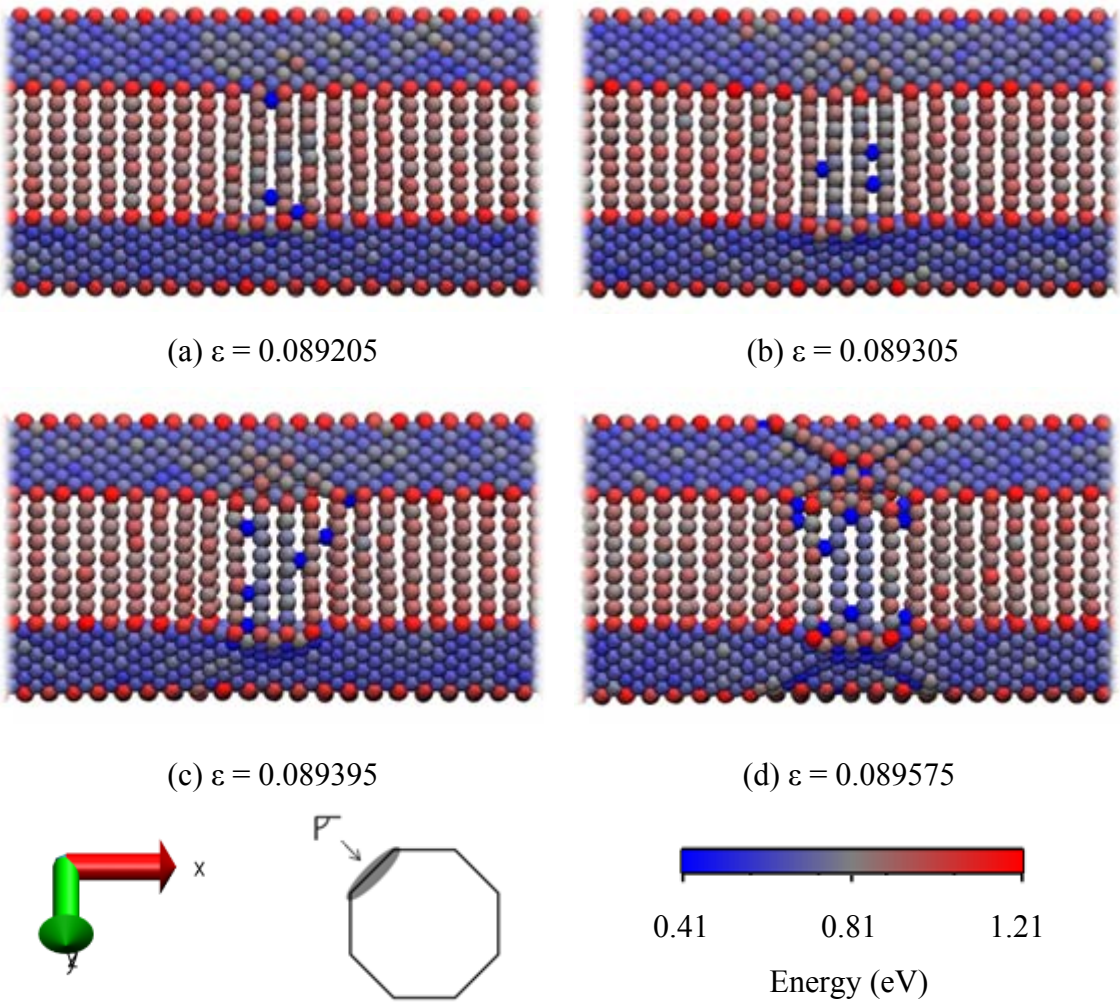

Figure 5.44 Surface defect creation and propagation on a 5 nm diameter octagonal palladium nanowire

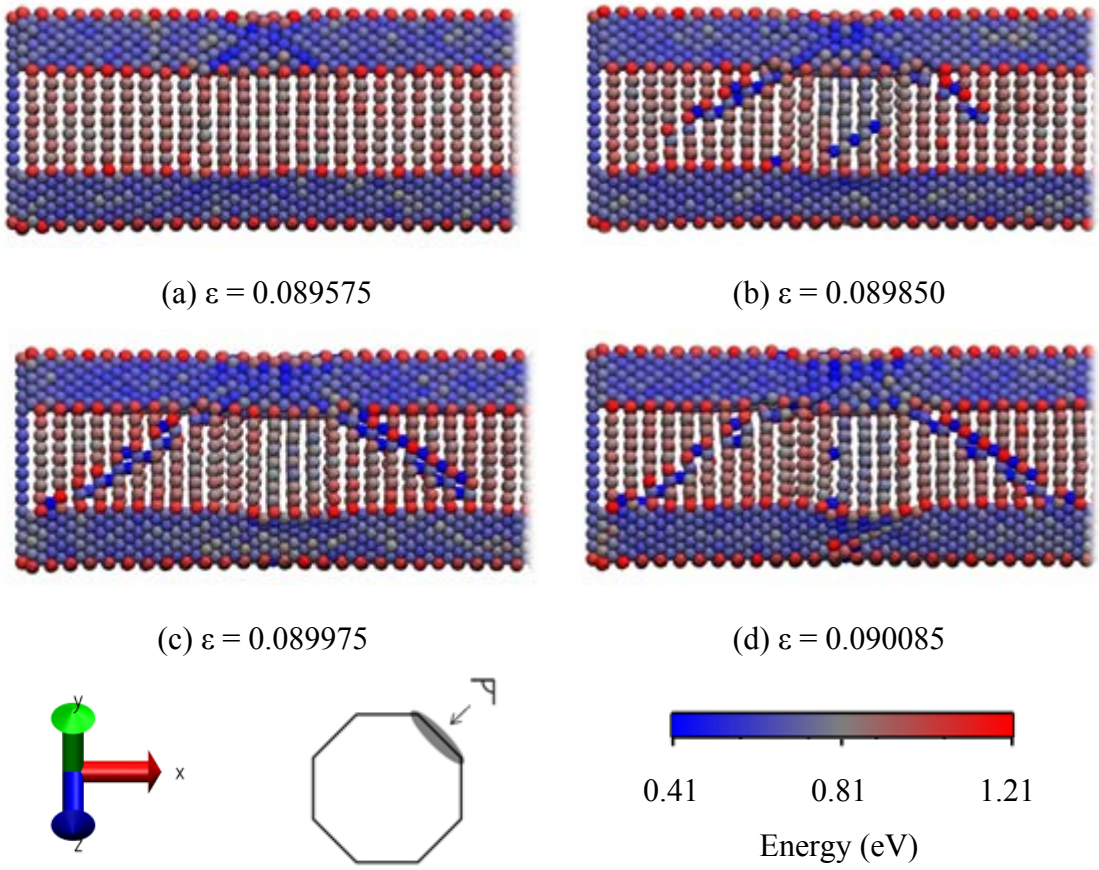

Figure 5.45 Defect propagation on a 5 nm diameter octagonal palladium nanowire

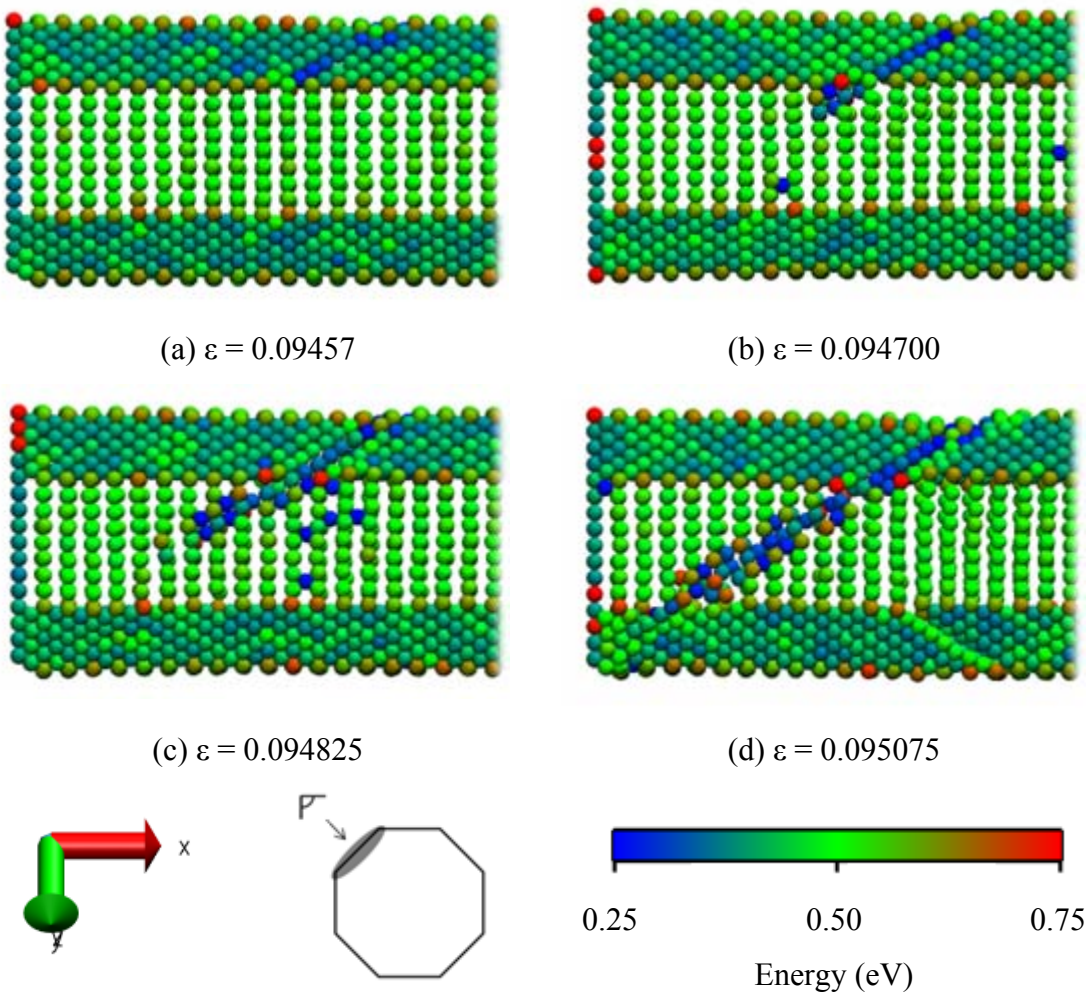

Figure 5.46 Surface defect propagation on a 5 nm diameter octagonal silver nanowire

Here, no twinning is observed. Square nanowires also exhibit similar yielding characteristics. A high energy corner atom is displaced by an interior atom creating an interstitial defect on the surface. The energy is then dissipated by displacing atoms across the structure. These displaced atoms then initiate a slip. Figure 5.47 shows this occurring on a 5 nm square palladium nanowire.

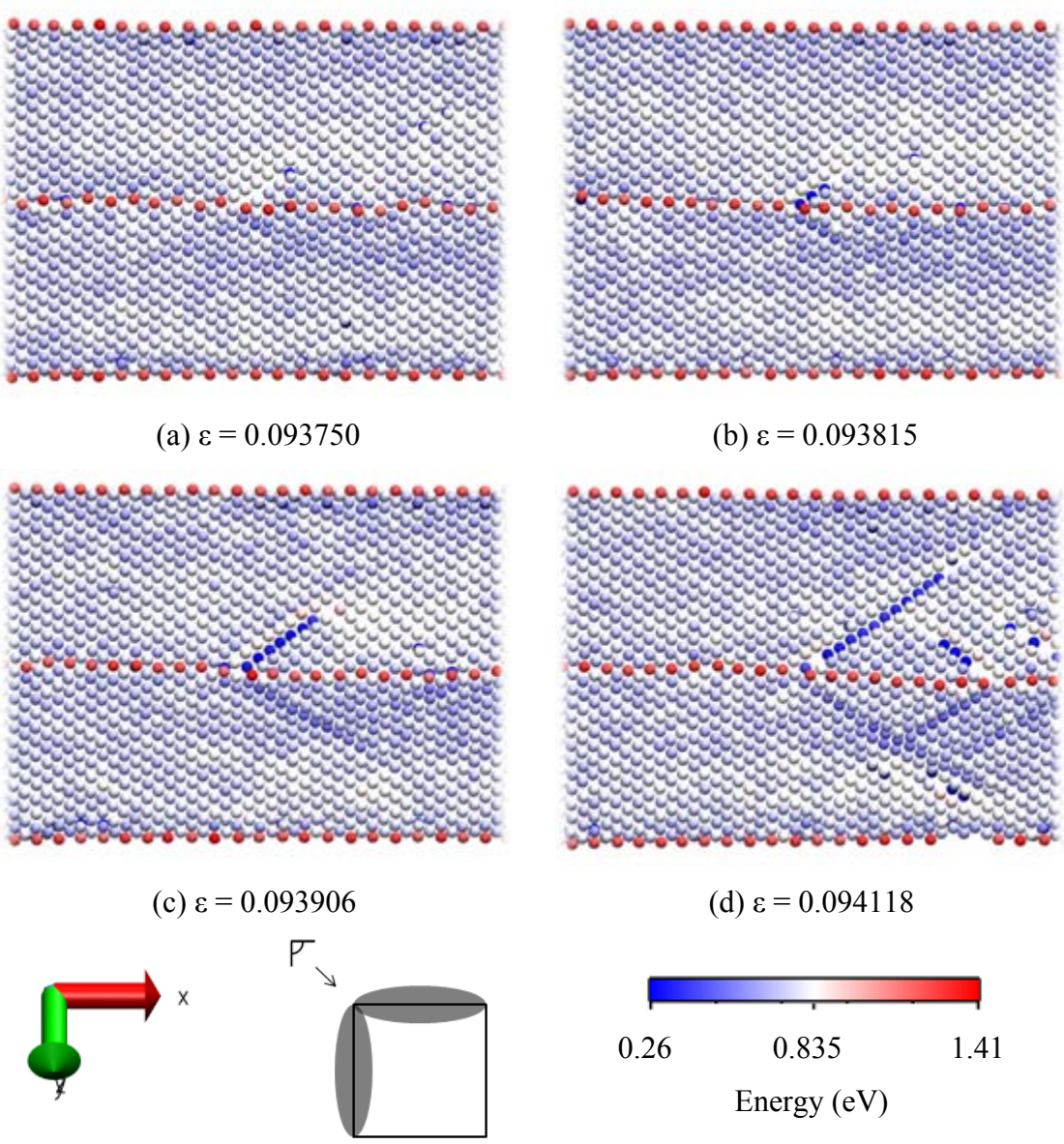

Figure 5.47 Defect propagation on the surface of a 5 nm diameter square palladium nanowire

The displaced atoms always emanate from a high energy corner. The corner atoms move leading to {111} slip which is the main method by which the nanowires deform.

5.5.2 Slip

To show the direction of the slip, a 5 nm square copper nanowire was colored such that three layers of atoms along the slip plane are highlighted as in Figure 5.53.

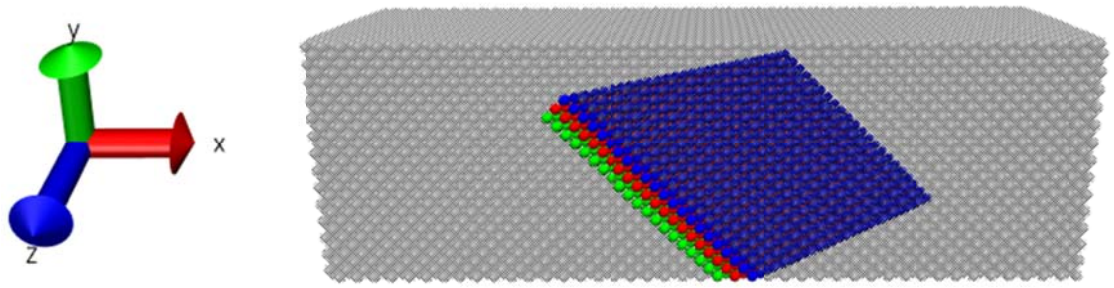

Figure 5.48 5 nm diameter copper nanowire with three adjacent (111) planes highlighted

For clarity, the atoms past the planes in the positive x direction were truncated in the following figures. In addition, the view was rotated so that the [111] direction is coming out of the page.

Figure 5.50 and Figure 5.51 show time lapse snapshots of the nanowire shown in Figure 5.49. Only the three colored surfaces are shown for clarity.

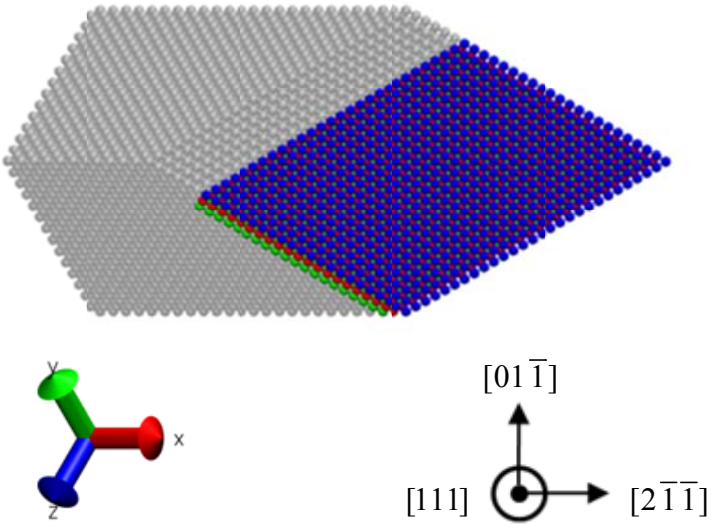

Figure 5.49 5 nm diameter copper nanowire at equilibrium rotated and truncated

In Figure 5.50 (a) the lattice is close to undisturbed from its equilibrium state, and the lattice stacking is still consistent with a face-centered cubic (fcc) lattice. In Figure 5.50 (b) a partial dislocation which nucleated at the edge of the structure has propagated $[1\bar{2}0]$ slip in the $[2\bar{1}\bar{1}]$ direction through nearly half of the cross section. Figure 5.51 shows the subsequent slipping that occurs.

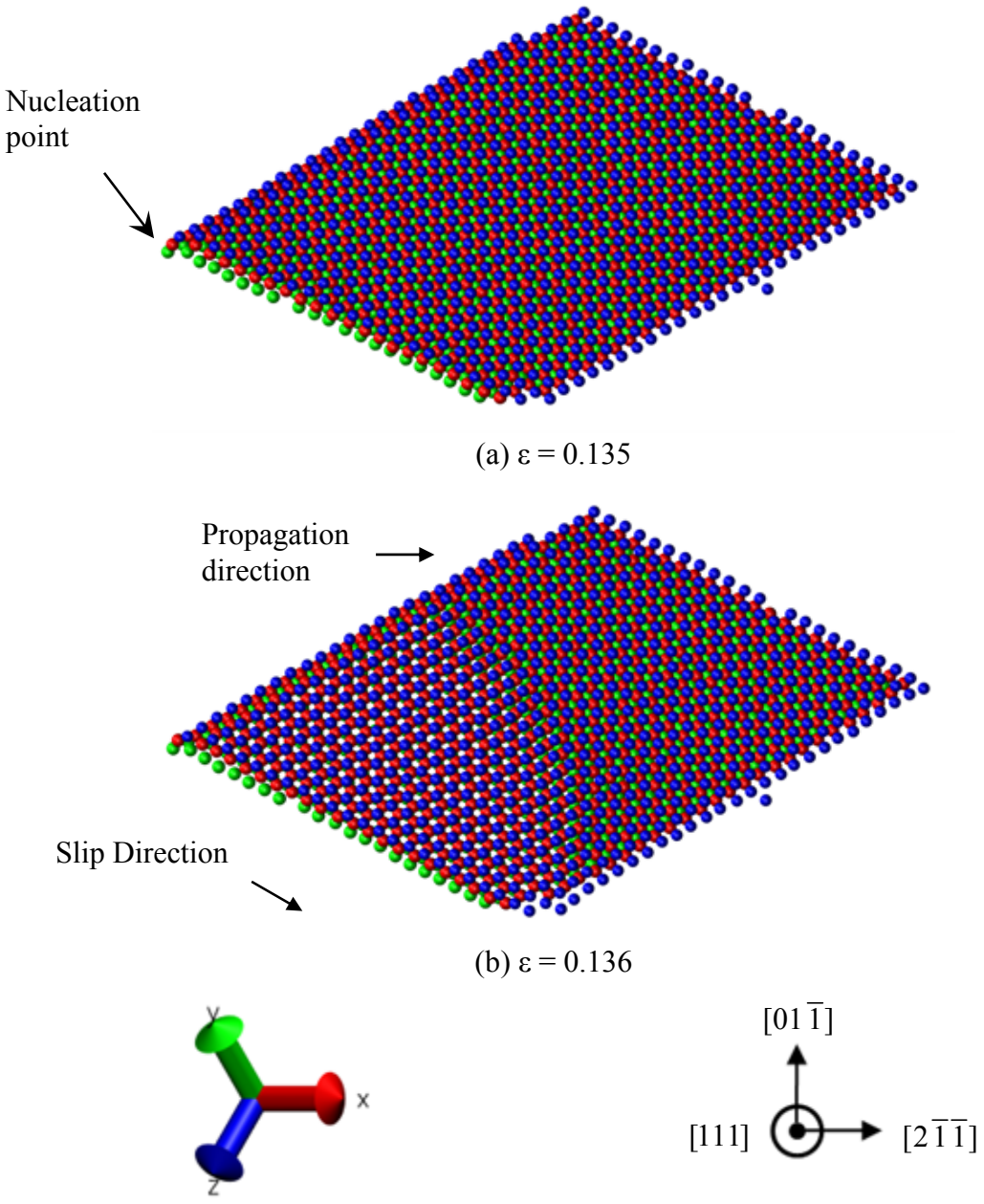

Figure 5.50 Nucleation and propagation of a partial dislocation on a (111) slip plane in a 5 nm diameter square copper nanowire

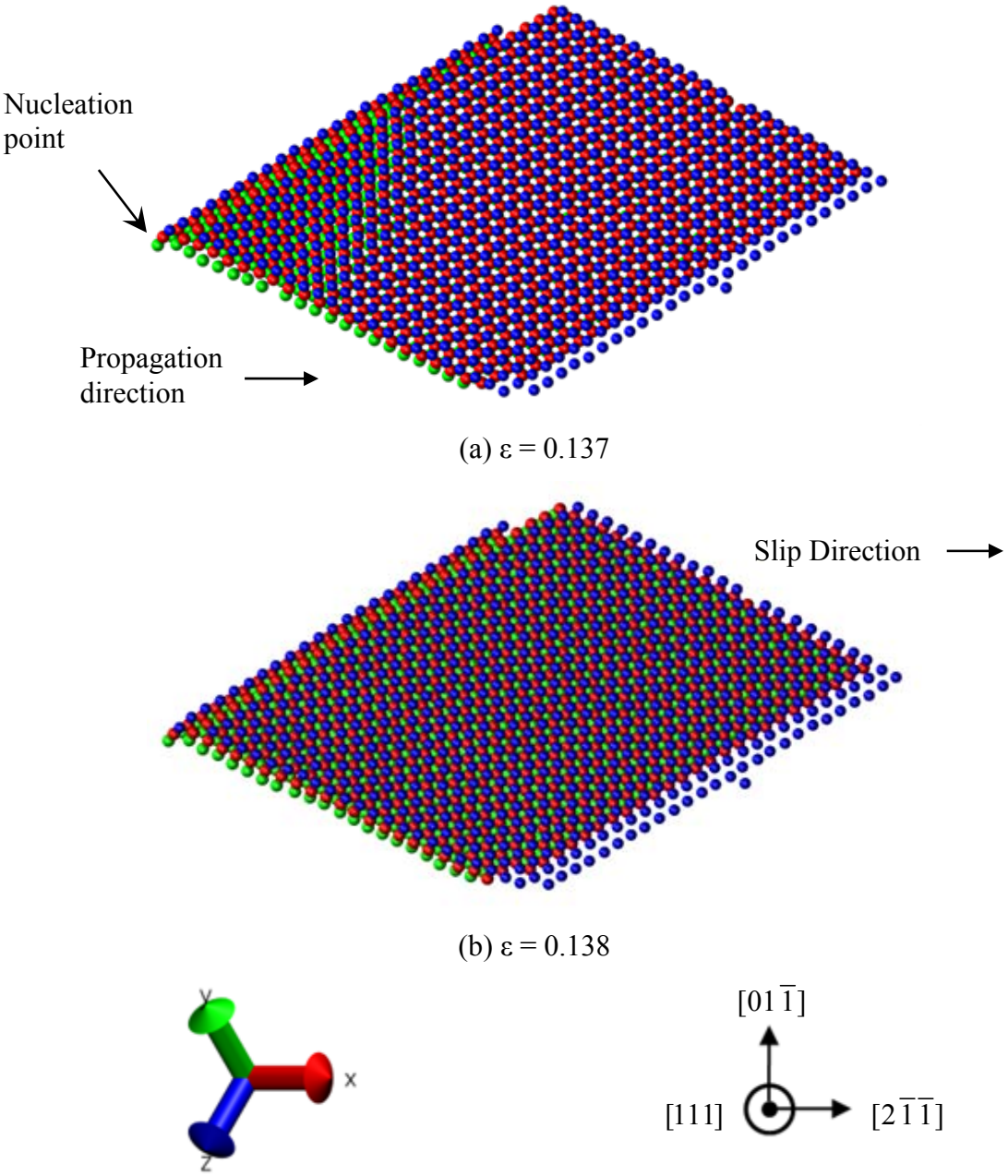

Figure 5.51 Subsequent nucleation and propagation of a dislocation on a (111) slip plane in a 5 nm diameter square copper nanowire

In Figure 5.51 (a), the partial dislocation has propagated across the entire cross section of the nanowire leaving a stacking fault behind. A second partial dislocation is also forming which brings the structure back to an fcc orientation. The second partial

dislocation nucleates in the same area as the first. However, in this case the slip both happens and propagates along the $[2\bar{1}\bar{1}]$ direction.

Similar deformation through slip was the prevalent form of deformation in almost all of the nanowires studied. In the subsequent figures, this slip is highlighted.

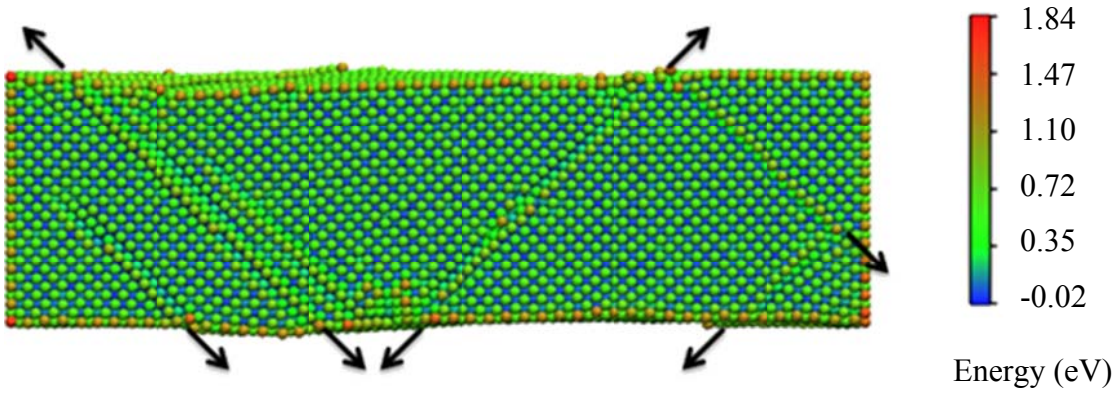

Figure 5.52 Slip planes visible at the point of yielding in a 5 nm diameter nickel nanowire

The slip is not limited to only the (111) plane. It occurs in all {111} class planes. Figure 5.52 shows the multiple slip planes present in a 5 nm diameter nickel nanowire. Figure 5.53 shows the same nanowire rotated 45^{o} around the x axis to show the slip planes continuing at the edges of the nanowire.

Octagonal nanowires also exhibit similar indications of slip on the {001} and {010} surfaces. Figure 5.54 highlights the slip on the (001) surface of an octagonal nickel nanowire. The slip looks very similar to the slip which can be seen on the surfaces of the square nanowire (Figure 5.52). When looking at a {011} surface, the planes appear to be at a 30^{o} angle rather than a 45^{o} angle. However, this is the same plane as the one seen on a {010} or {001} surface. The angle change indicates only a rotation of the global coordinate system and surface cut.

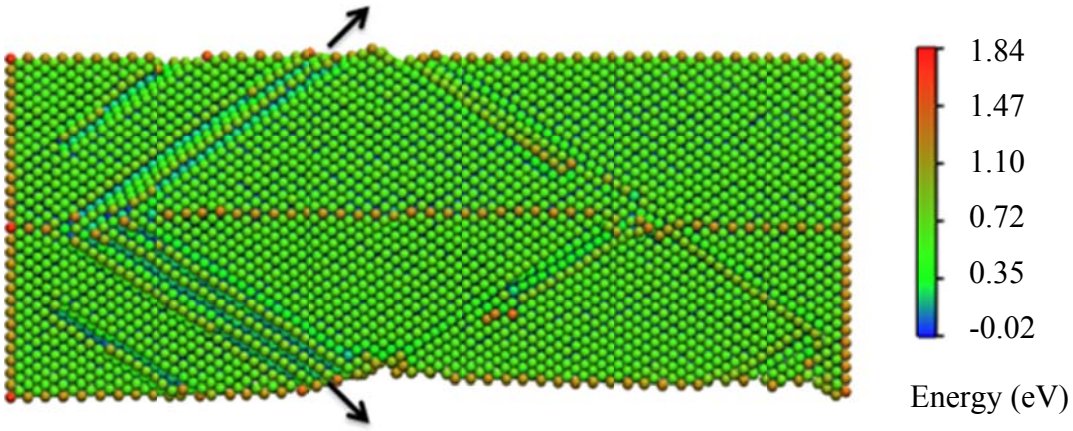

Figure 5.53 Different view of the nickel nanowire showing the slip planes continuing at the edges

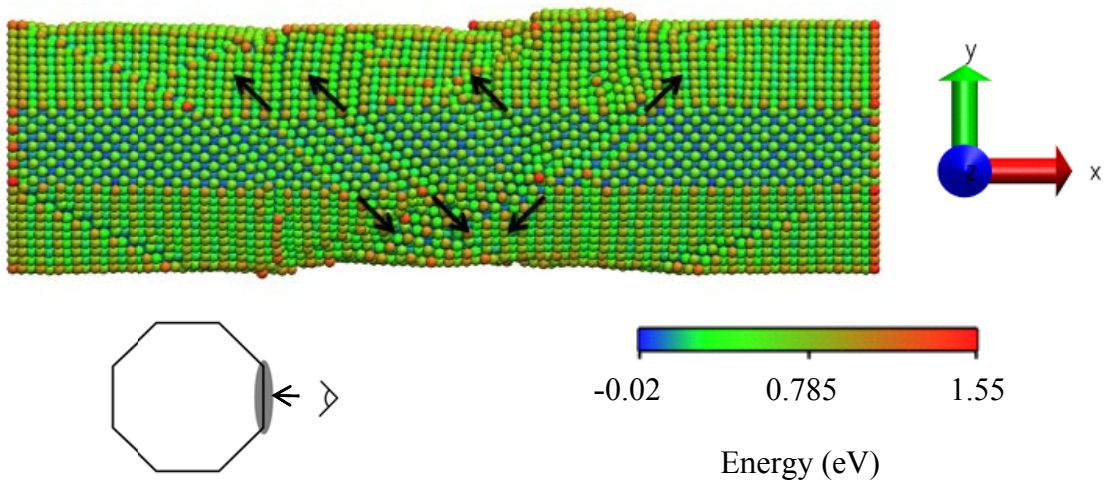

Figure 5.54 Side view of 5 nm diameter nickel octagonal nanowire

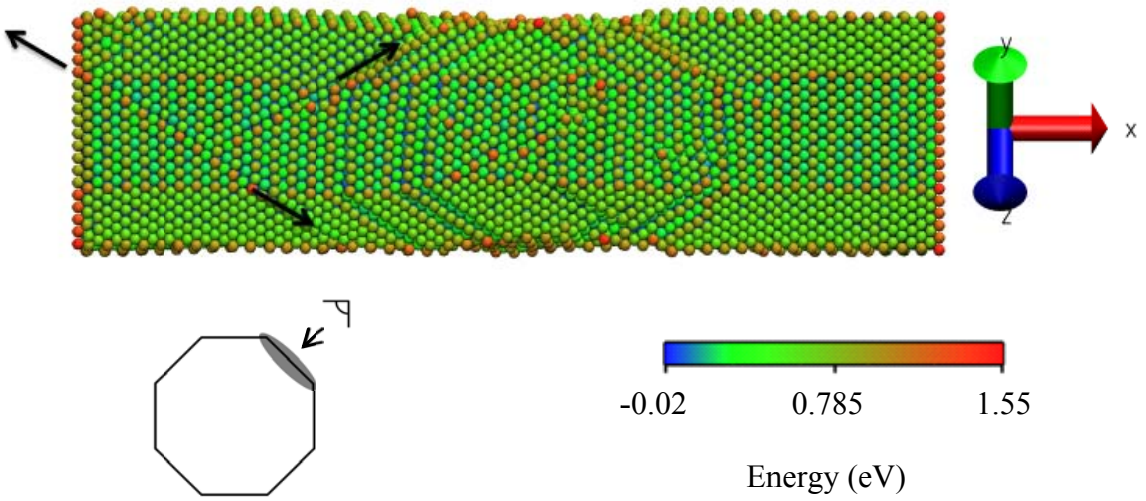

Figure 5.55 5 nm diameter nickel octagonal nanowire rotated 45^{o} around the x-axis highlighting the slip on a {011} surface

5.5.3 Reconstruction

The prevalent mechanism of yield in the nanowires studied is partial dislocation leading to {111} slip. However, octagonal platinum nanowires were found to exhibit a surface reconstruction phenomenon due to the higher energy {011} surfaces. To highlight the difference in these two yield mechanisms, Figure 5.56 shows 5 nm diameter square and octagonal platinum nanowires at equilibrium with the central five layers highlighted. . In the subsequent figures, these atoms are tracked throughout the deformation process. Figure 5.57 shows both the square and octagonal nanowire immediately after yielding.

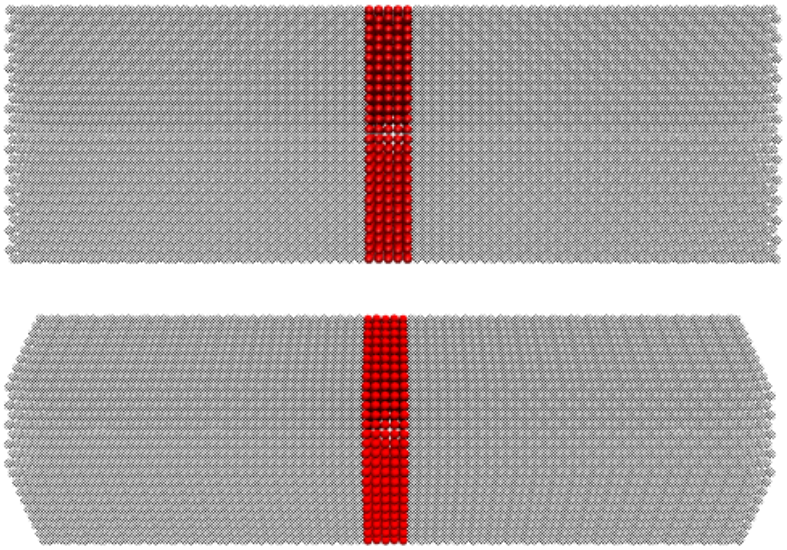

(a) ε = 0

(b) ε = 0

Figure 5.56 5 nm diameter square and octagonal platinum nanowires with central atoms highlighted at equilibrium

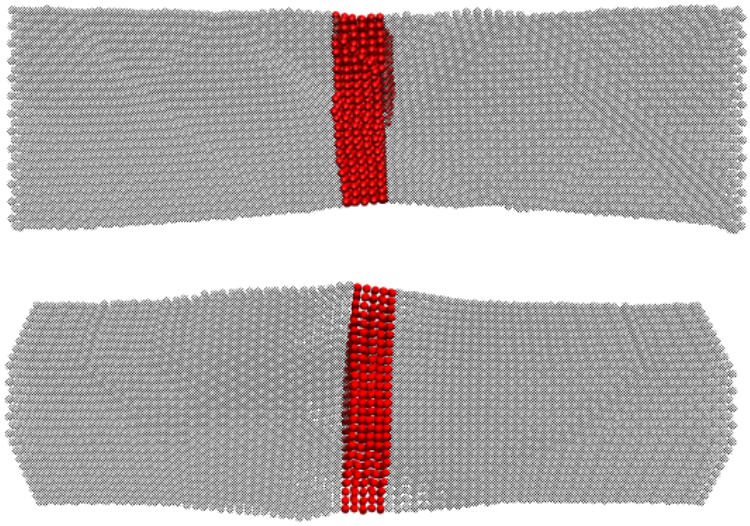

(a) ε = 0.091

(b) ε = 0.081

Figure 5.57 5 nm diameter square and octagonal platinum nanowires with central atoms highlighted immediately after yielding

The slip planes are visible through the central atoms of the square nanowire in Figure 5.58 (a). The widening of the nanowire in the vertical direction visible in Figure

5.58 (b) is an indication of the restructuring. The structure reconfiguration is more evident in Figure 5.58.

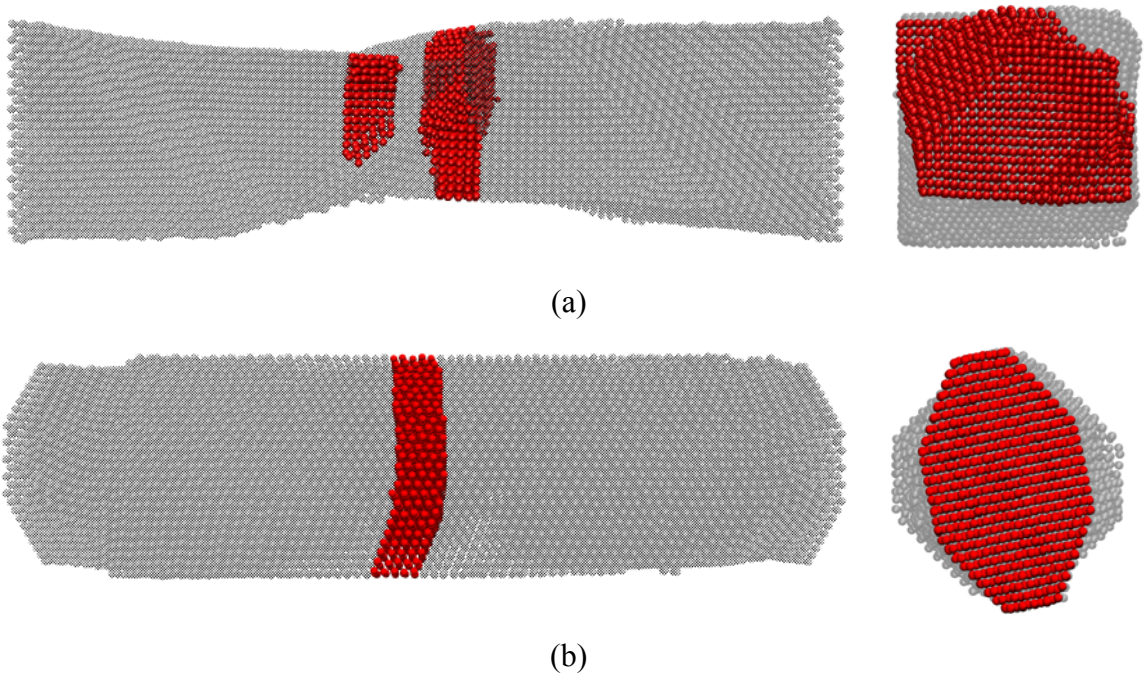

(a)

(b)

Figure 5.58 5 nm diameter square and octagonal platinum nanowires and cross sections with central atoms highlighted at ε = 0.250

Figure 5.58 shows both nanowires at an elongation of 25%. The cross-sectional view shows the nanowires orthographically with the atoms which would hinder the view truncated. In Figure 5.58 (a) the central atoms have shifted into different planes due to {111} slip. However, the cross section shown in Figure 5.58 (b) still exhibits an ordered configuration for the central atoms. The side view of both nanowires at ε = 0.500 can be seen in Figure 5.59. Even at 50% elongation, the central atoms in the octagonal nanowire are clustered. The central atoms in the square nanowire have moved to varied locations due to the {111} slip.

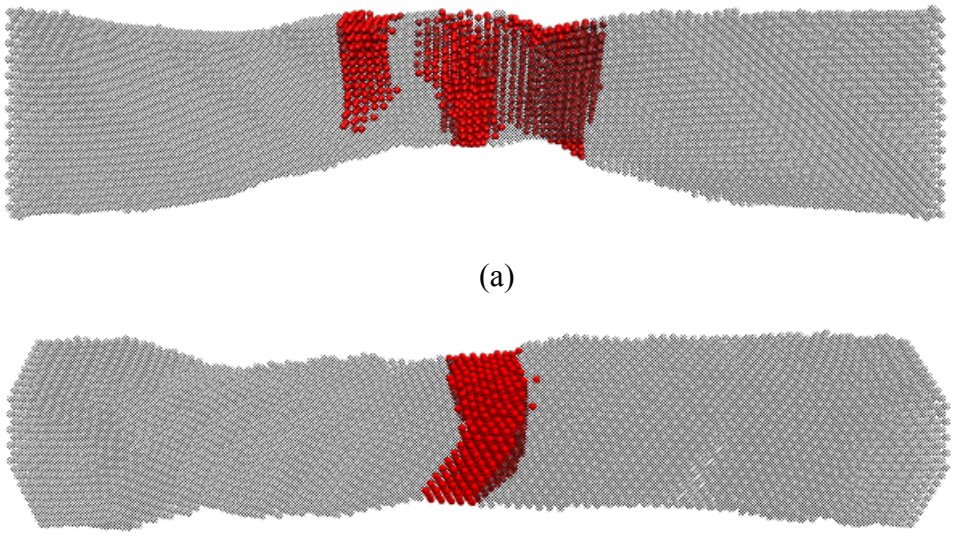

(a)

(b)

Figure 5.59 5 nm diameter square and octagonal platinum nanowires and cross sections with central atoms highlighted at ε = 0.500

To investigate the reconstruction phenomenon more carefully, the octagonal cross section atoms' energies before and after yielding are illustrated in Figure 5.59.

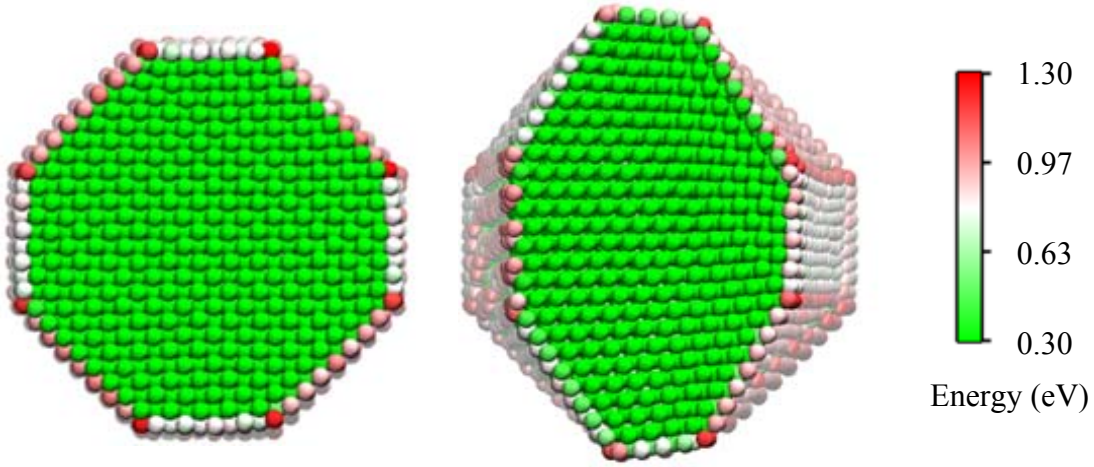

(a) ε = 0.076 (b) ε = 0.081

Figure 5.60 5 nm diameter octagonal nanowire with atoms colored by energy before (a) and after (b) yielding

Before yielding, the {011} surfaces are at a higher energy than the {010} or {001} surfaces. After yielding, all {011} surfaces are reconstructed to lower energy {021} surfaces. Since the square cross-sectional nanowires do not have any high energy {011} surfaces, they do not exhibit this reconstruction.

Figure 5.61 shows the yielding through reconstruction with higher time resolution. Only the surface atoms on the closer half of the structure are shown to highlight the reconstruction.

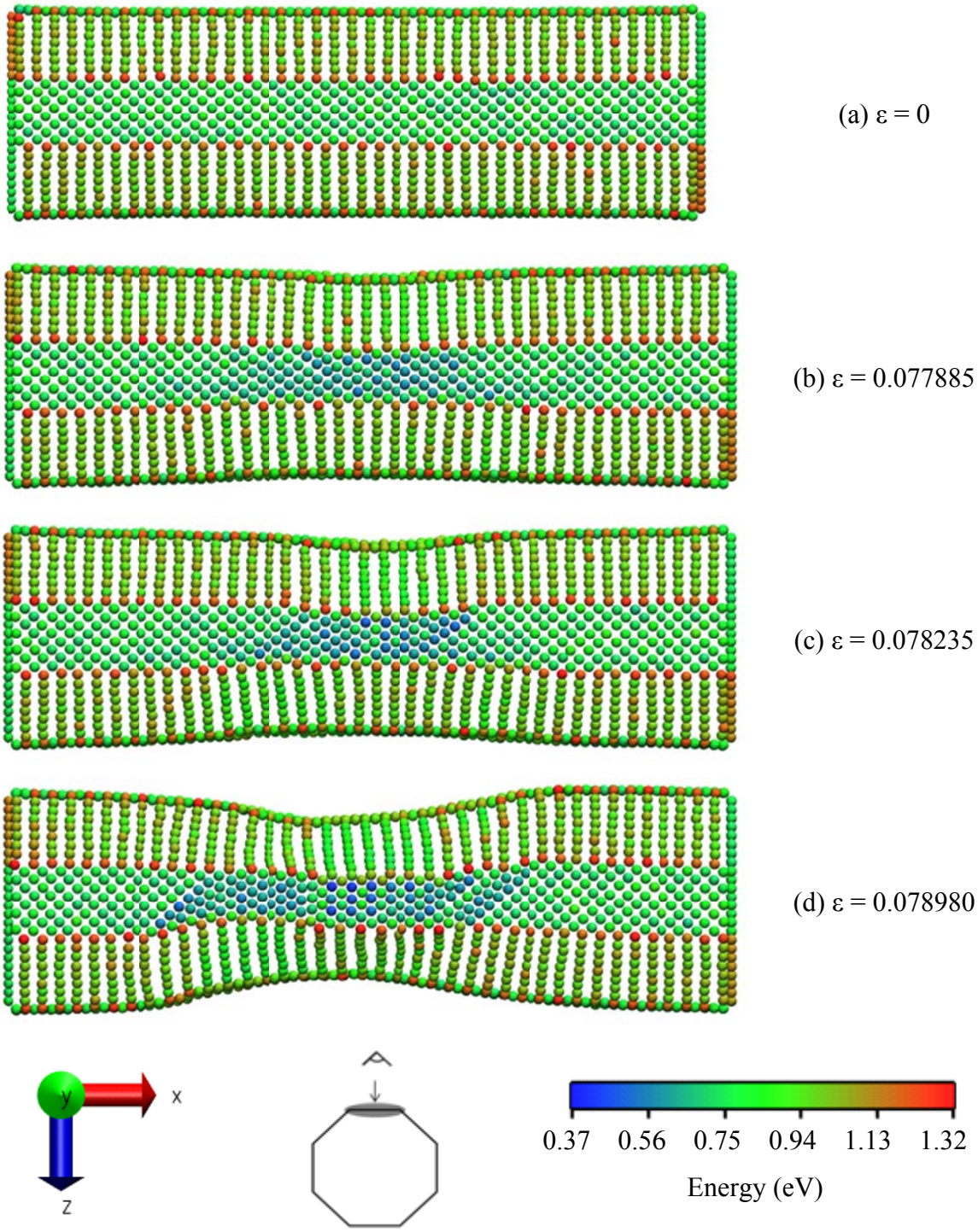

Figure 5.61 (010) surface of a 5 nm diameter octagonal platinum nanowire showing the process of surface reconstruction

Figure 5.61 (a) shows the octagonal structure at zero strain. In Figure 5.61 (b), the structure shows a small amount of necking. On the (010) surface, the central atoms are at a lower energy than they were before the necking. Figure 5.61 (c) and (d) show further necking to the point of reconstruction. The atoms on the (010) surface have become more densely packed, thus decreasing their energy. Figure 5.62 shows a magnified view of the surface before and after reconstruction.

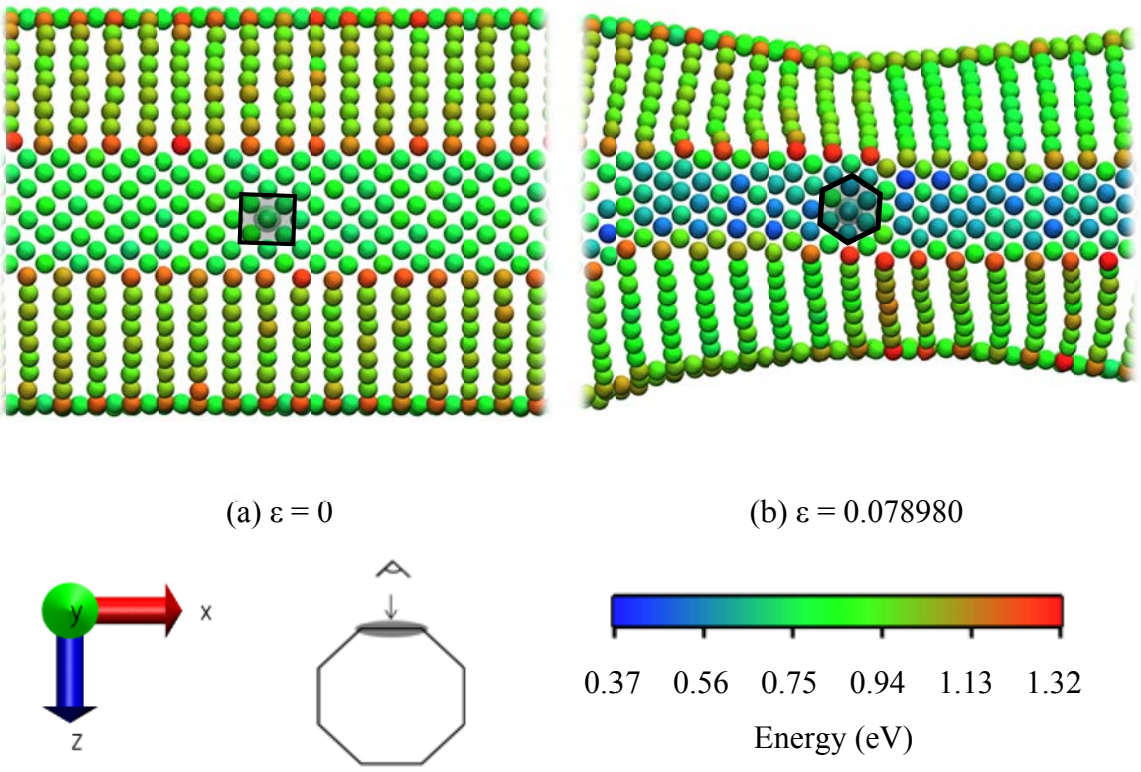

Figure 5.62 Magnified view of the (010) surface of a 5 nm diameter octagonal platinum nanowire showing surface atoms reconstruction

Figure 5.62 (a) shows the surface of the nanowire at zero strain while (b) shows the nanowire after surface reconstruction. During the reconstruction, the surface atoms became more closely packed as indicated by the square and hexagon emphasizing the number of neighboring atoms. The reconstruction resulted in a shift from four to six surface neighbors.

6. CONCLUSIONS

6.1 Conclusions

Molecular dynamics simulations which simulated tensile stretching were performed on nanowires composed of six different fcc metals across three different shapes and three different sizes. Prior to loading, the nanowires' equilibrium strain was found. The equilibrium strain was found to vary due to shapes, sizes, anisotropy of the material, and energetic differences between surfaces.

Stress-strain diagrams were created from [100] tensile loading of <100> nanowires. These stress-strain diagrams were used to calculate many properties including yield stress, yield strain, ultimate strain, and Young's modulus. Young's modulus was found to decrease with decreasing diameter until a critical cross-sectional size. The yield strain was found to increase with decreasing diameter, while the yield stress remained relatively constant. Finally, the ultimate strain was found to increase with increasing diameter.

In addition to calculating Young's modulus from functional fitting of the stress-strain response, an energy method was employed to calculate Young's modulus. The two methods gave qualitatively similar results. The energy method also allowed for investigation of the smaller diameter nanowires. These nanowires exhibited a substantial increase in Young's modulus. However, the physicality of the structures was called into question.

Young's modulus was again calculated by inverting the stiffness matrix for each material. As the diameter increased, the molecular dynamics approach showed the

Young's modulus values tending toward the value calculated by inversion of the stiffness matrix. The molecular dynamics values should approach the matrix values with increasing diameter because the larger diameter nanowires are closer in structure to the bulk material state. These findings further validated the molecular dynamics approach.

Lastly, through visualization of the stretching process, the yield characteristics of the nanowires were investigated. Most nanowires failed through partial dislocation leading to {111} slip. The only exception was the 5 nm diameter platinum nanowires. The square and circular platinum nanowires showed a mix of slip and surface reconstruction at a diameter of 5 nm. The 5 nm diameter octagonal nanowire failed almost exclusively through a reconstruction of the {011} surfaces to {021} surfaces to minimize energy. The surface reconstruction which occurred in these nanowires caused the ultimate strain to be much greater.

6.2 Recommendations for Future Research

Further work could be done to expand upon the research covered in this thesis as described below.

- The surface reconstruction in the octagonal platinum nanowire should be investigated further. Of the 54 configurations studied, only this one exhibited this type of yielding behavior. It would be helpful to compare the atomic energies at the minimized strain and during the deformation to other shapes and sizes.

- Due to time and space constraints, the results from the largest nanowires (8 nm diameter) were not investigated as deeply as the other sizes. A comparison of yield mechanisms and behaviors between two differently sized nanowires could be useful.

- Since the circular nanowires did not have well-defined crystal surfaces, most of the discussion was restricted to the square and octagonal cross-sectional

nanowires. Further investigation of the yield mechanism of the circular nanowires could be completed.

- All nanowires consisted of a single material. Similar studies could be completed on both ordered and disordered alloyed nanowires.

- Only <100> nanowires were researched. More work could be done comparing and contrasting the yield and mechanical behavior in differently oriented nanowires.

- The nanowires created for this research were free of defects and voids. Introduction of voids or defects could produce drastically different results and lead to a deeper understanding of the deformation mechanics.

LIST OF REFERENCES

LIST OF REFERENCES

[1] J. B. Adams, S. M. Foiles, and W. G. Wolfer, "Self-diffusion and impurity diffusion of FCC metals using the five-frequency model and the Embedded Atom Method," *Journal of Materials Research*, pp. 102-112, 1989.

[2] B. J. Alder and T. E. Wainwright, "Studies in Molecular Dynamics. I. General Method," *The Journal of Chemical Physics*, pp. 459-466, 1959.

[3] S. J. Plimpton, "Fast Parallel Algorithms for Short-Range Molecular Dynamics," *J Comp Phys*, pp. 1-19, 1995.

[4] M. S. Daw and M. I. Baskes, "Embedded-atom method: Derivation and application to impurities, surfaces, and other defects in metals," *Physical Review*, pp. 6443-6453, 1984.

[5] Molecular Dynamics. (Last accessed: Feburary 2010) Wikipedia. http://en.wikipedia.org/wiki/molecular_dynamics

[6] H. S. Park and J. A. Zimmerman, "Modeling inelasticity and failure in gold nanowires," *Physics Review*, pp. 054106-1-054106-9, 2005.

[7] Y. Kondo and K. Takayanagi, "Gold Nanobridge Stabilized by Surface Structure," *Physical Review Letters*, vol. 79, no. 18, pp. 3455-3458, 1997.

[8] S. J. A. Koh, H. P. Lee, C. Lu, and Q. H. Cheng, "Molecular dynamics simulation of a solid platinum nanowire under uniaxial tensile strain: Temperature and strain-rate effects," *Physical Review*, pp. 085414-1 - 085414-11, 2005.

[9] S. J. A. Koh and H. P. Lee, "Molecular dynamics simulation of size and strain rate dependent mechanical response of FCC metallic nanowires," *Nanotechnology*, vol. 17, no. 14, pp. 3451-3467, June 2006.

[10] A. M. Leach, M. McDowell, and K. Gall, "Deformation of Top-Down and Bottom-Up Silver Nanowires," *Advanced Functional Materials*, vol. 17, no. 1, p. 2006, November 2007.

[11] G. Wang and X. Li, "Predicting Young's modulus of nanowire from first-principles calculations on their surface and bulk materials," *Journal of Applied Physics*, vol. 104, no. 11, p. 113517, December 2008.

[12] J. Diao, K. Gall, and M. L. Dunn, "Atomistic simulation of the structure and elastic properties of gold nanowires," *Journal of the Mechanics and Physics of Solids*, vol. 52, no. 9, pp. 1935-1962, March 2004.

[13] B. Wu, A. Heidelberg, and J. J. Boland, "Mechanical properties of ultrahigh-strength gold nanowires," *Nature Materials*, vol. 4, pp. 525-529, July 2005.

[14] W.D. Callister, *Materials Science and Engineering*, 3rd ed. New York: Wiley, 1994.

[15] G. Y. Jing et al., "Surface effects on elastic properties of silver nanowires: Contact atomic-force microscopy," *Physical Review*, vol. 73, no. 23, pp. 235409-1 - 235409-6, June 2006.

[16] W. Humphey, A. Dalke, and K. Schulten, "VMD - Visual Molecular Dynamics," *Journal of Molecular Graphics*, vol. 14, pp. 33-38, 1996.

APPENDIX

APPENDIX

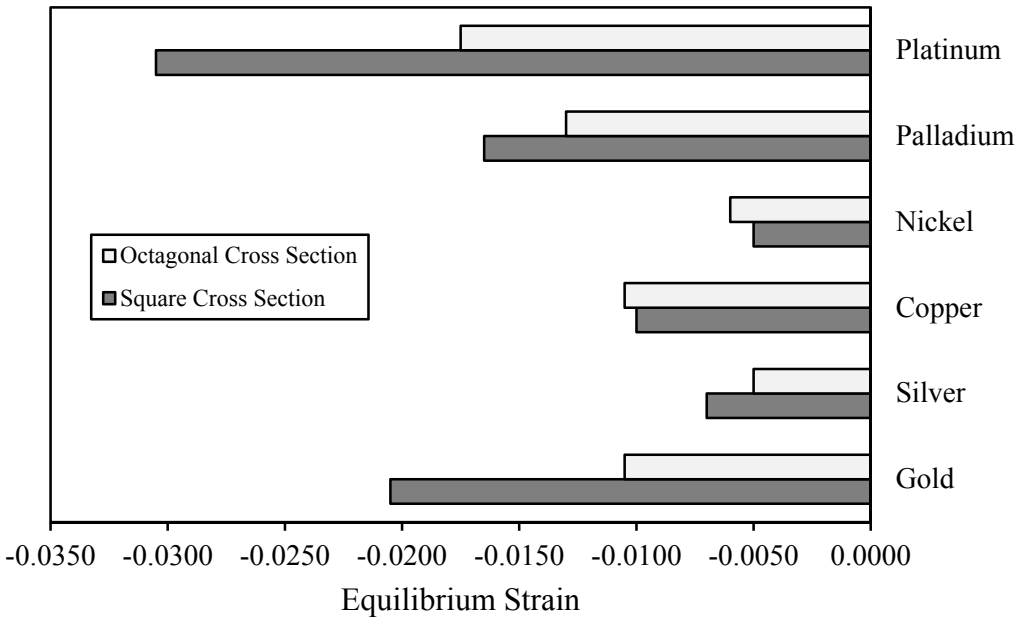

Figure A.1 Comparison of the equilibrium strain of 5 nm square and octagonal cross section nanowires

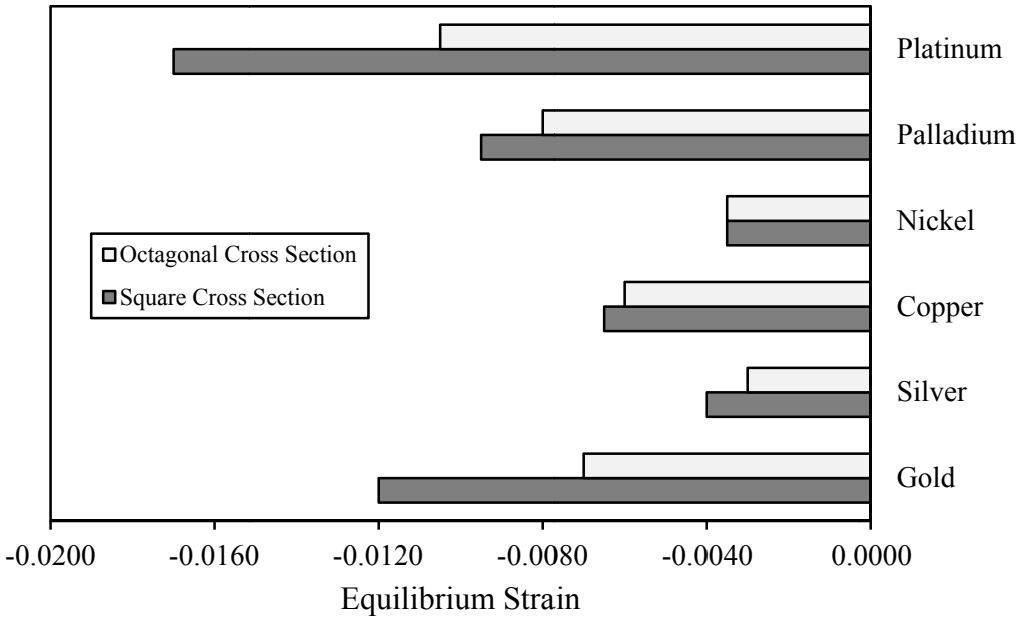

Figure A.2 Comparison of the equilibrium strain of 8 nm square and octagonal cross section nanowires

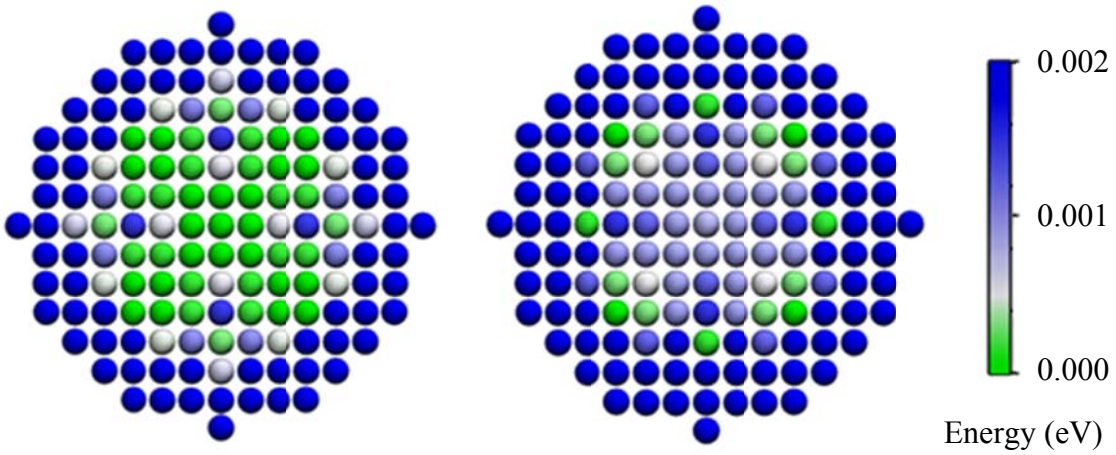

Figure A.3 2.5 nm nickel nanowire cross sections before minimization at $\varepsilon = 0$ (left) and after minimization at $\varepsilon = -0.0105$ (right)

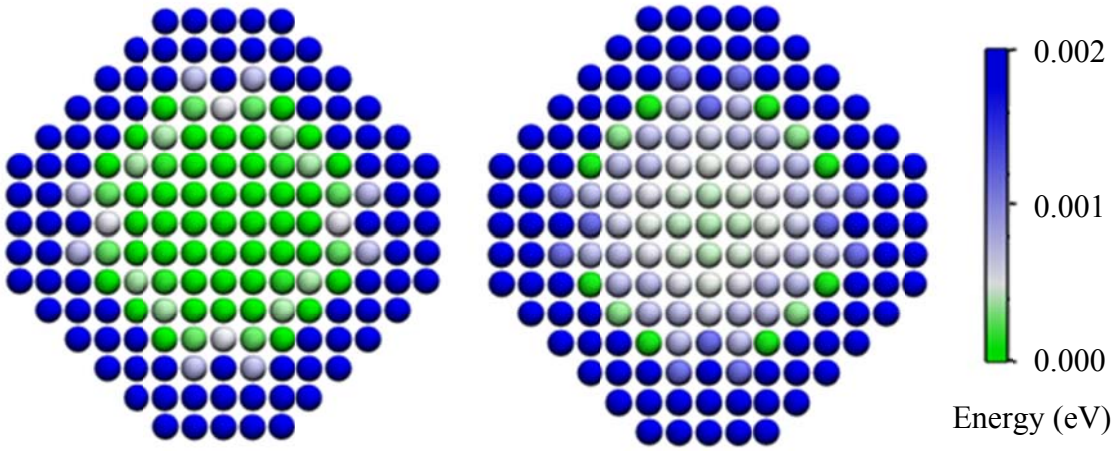

Figure A.4 2.5 nm nickel nanowire cross sections before minimization at ε = 0 (left) and after minimization at ε = -0.0105 (right)

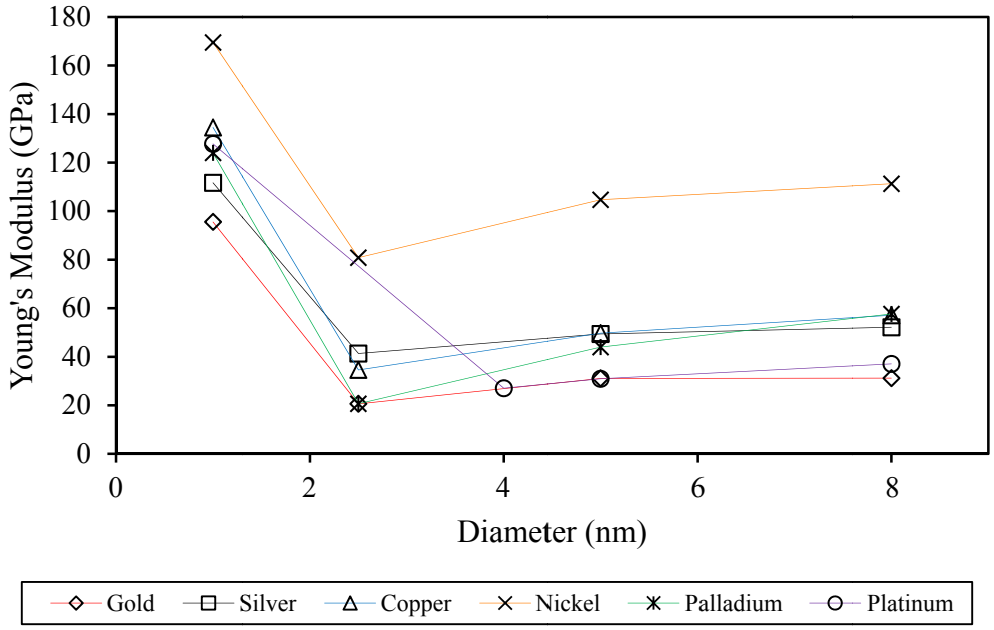

Figure A.5 Young's modulus as a function of diameter for circular nanowires including 1 nm diameter

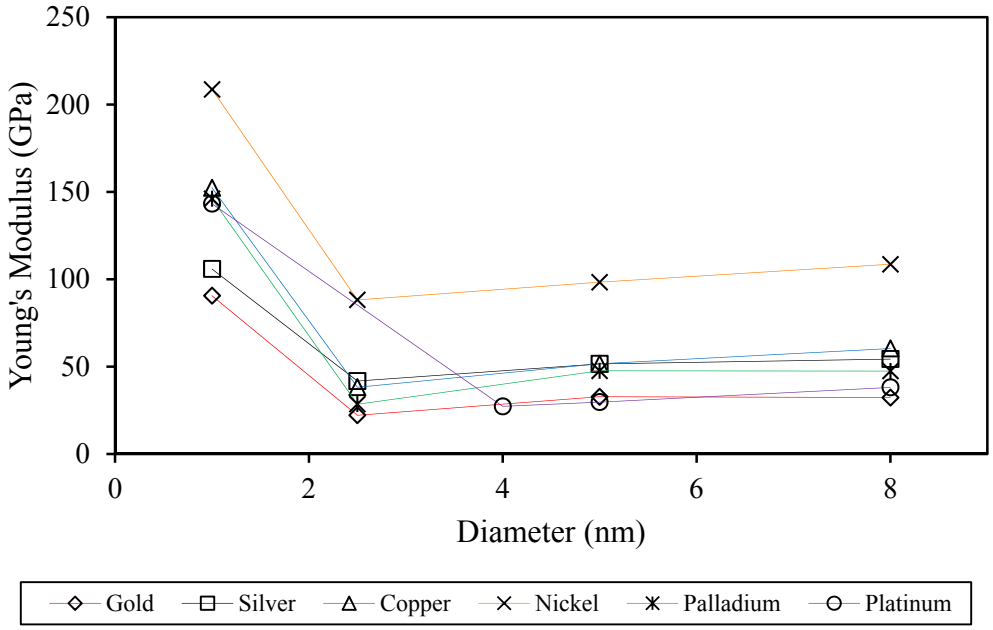

Figure A.6 Young's modulus as a function of diameter for octagonal nanowires including 1 nm diameter